MONOGRAFIE, STUDIA, ROZPRAWY

M45

Wojciech Żórawski

TRIBOLOGICAL PROPERTIES OF COMPOSITE COATINGS SPRAYED WITH A HIGH VELOCITY STREAM

Kielce 2013

MONOGRAFIE, STUDIA, ROZPRAWY NR M45

Redaktor Naukowy serii
NAUKI TECHNICZNE – BUDOWA I EKSPLOATACJA MASZYN
prof. dr hab. inż. Stanisław ADAMCZAK, dr h.c.

Recenzenci:
Prof. dr hab. inż. Tomasz OTMIANOWSKI
Prof. dr hab. inż. Stanisław PYTKO

Redakcja techniczna
Irena PRZEORSKA-IMIOŁEK

Projekt okładki
Tadeusz UBERMAN

Wyd. I
Nakład: 60 egz.
Objętość: 9,5 ark. wyd.

PL ISSN 1897-2691
PL ISBN 978-83-63792-48-0

Wydawnictwo Politechniki Świętokrzyskiej
25-314 Kielce, al. Tysiąclecia Państwa Polskiego 7
tel./fax 41 34 24 581
e-mail: wydawca@tu.kielce.pl
www.tu.kielce.pl/organizacja/wydawnictwo

Contents

Symbols

γ	Nondimensional roughness parameter
χ	Nondimensional parameter describing mass loss by particle
ν	Particie velocity
σ	Stefan-Boltzman constant
λ	Oxygen to propane ratio
ν	Poisson modulus
ξ	Flattening parameter
μ	Coefficient of friction
η	Content of Fe_3O_4 in the powder mixture
η_g	Gas dynamic viscosity
χ_m	Percentage share of the metal-tungsten carbide contact
μ_m	Friction coefficient of the metal-tungsten carbide contact
η_p	Particle viscosity
ε_p	Radiative emission coefficient
σ_s	Stresses shearing of the solid lubricant
χ_s	Percentage share of the solid lubricant film coverage
μ_s	Dry friction coefficient of the solid lubricant in the friction joint
σ_t	Unit stresses necessary to shear the welded areas
λ_w	Wavelength distribution between two adjacent jet tops
ρ_g	Gas density
ρ_p	Particle density
ρ	Share of the effect of the spray parameter on the coating property
C_D	Coefficient of aerodynamic drag
d	Spraying distance
d_p	Particle diameter
D_s	Lamella diameter
$E^{'}$	Equivalent modulus of elasticity for the lubricating film and the steel ball
F	Surface area of the elements in contact
F_{ad}	Adhesive bonding force
F_{chem}	Chemical bonding forces
F_{dyf}	Diffusive bonding forces
F_{epit}	Epitaxial bonding force
F_{koh}	Cohesive bonding forces
F_m	Mechanical bonding force
F_r	Actual surface area of the elements in contact
H	Composite hardness
h	Heat transfer coefficient
M	Mach number

N	Normal force
Nu	Nuselt number
p_0	Stagnation pressure (the sum of Static Pressure and Dynamic Pressure)
p_q	Unit loads at the interface
Pr	Prandtl number
Q	Air flow rate
q	Heat rate
r	Ball radius
Re	Reynolds number
s	Sum of standard deviations
S	Sum of squares
SN	Taguchi's loss function (signal to noise ratio)
T	Temperature
T_p	Temperature of particle before impact
T_0	Stagnation temperature
u	Gas velocity
V	Variance
y_i	Output parameter
φ	Angle between the coordinate systems of principal stresses and sample
ψ	Angle between the normal to the surface and the normal to the deflecting plane {*hkl*}

Miscellaneous

APS	Air Plasma Spraying
HVOF	High Velocity Oxy-Fuel
HP/HVOF	High Pressure/HVOF
HVOLF	High Velocity Oxyliquidfuel
HVSFS	High Velocity Suspension Flame Spraying
HVAF	High Velocity Airfuel Flamespraying
VPS	Vacuum Plasma Spraying
PVD	Physical Vapour Deposition
HAADF	High-Angle Annular Dark-Field Imaging
EDX	Energy Dispersive X-Ray Spectrometer
EDS	Energy Dispersive Spectrometer

Chapter 1

Introduction

Friction, wear and lubrication are some of the top issues to be addressed by all industries. They are responsible for the durability of friction pairs, then, in consequence, the capacity of machines and devices, and, finally, the efficiency of a whole industry. Machine parts in contact may be affected by such factors as an increase in the load, a decrease in the sliding velocity, an insufficient amount of lubricant or a deterioration of its properties. In many friction pairs, especially those involving a reciprocating motion, friction is assumed to be of mixed type. The occurrence of boundary and dry friction implies considerable losses of energy, an increase in the temperature of mating elements and their accelerated wear. Under extreme conditions, these may lead to seizure and failure of a whole system. To separate contact surfaces, we use a liquid or solid lubricant. Whether it is part of a seal or heat exchanger system or of a separate lubrication system, its quality and quantity need to be controlled. Solid lubricants are common in friction pairs operating under mixed friction conditions with predominant boundary and dry frictions. Because of their lamellar structure, they ensure lower friction of elements in a sliding contact. The most common solid lubricants are: graphite, molybdenum disulfide and tungsten disulfide [53, 93, 117, 120].

Today, with the use of nanocrystalline materials, the performance of friction pairs can be further improved. The new polycrystalline solids have particles several nanometers in size, generally not exceeding 100 nm. The value is different for different materials and depends on the functional properties of the elements to be produced.

The concept of nanotechnology was first mentioned in 1959 by a Noble laureate Richard Feynman in his visionary talk *There's plenty of room at the bottom* given at the American Physical Society annual meeting [65, 67]. The common availability of nanomaterials today is a result of rapid advances in this field. Intensive research, starting in the 1980s, has brought about significant changes in the properties of materials, making nanosize materials superior to micromaterials. Nanomaterials, which include metals, ceramics, glasses, polymers and composites, can be divided into 3 groups: one-dimensional lamellar structures, where the length and width are much greater than the thickness of a layer, with this being of the order of several nanometers, two-dimensional fibrous structures, for instance, in the form of wires, with a length considerably greater than the width and thickness or diameter, three-dimensional crystalline structures, where all the three dimensions are of the order of several nanometers. Nanomaterials can be produced using different methods. The most common are: mechanical synthesis, rapid cooling, physical vapor deposition (PVD), chemical vapor deposition (CVD), sol-gel transition, and electrolytic deposition. To be considered nano, a technology needs to satisfy all of the following conditions: the structures produced should have at least one dimension not greater than 100 nm, their physical and chemical properties can be controlled, and such structures can be combined to create larger nanostructures [4, 64, 65]. The development of nanomaterials means learning about new phenomena on atomic and molecular scales. The basic difference between a micro- and a nanometric structure is the volume fraction of atoms occupying the grain boundary area, with this fraction being considerably higher in nanomaterials. Compared with conventional composites, composites with nanometric particle fillers demonstrate higher abrasion resistance at a smaller friction coefficient.

Nanocrystalline coatings can be produced using thermal spraying techniques, which involve deposition of a material in a molten, semi-molten or solid state. The material to be deposited can be in the form of a powder or a wire. The two major factors in all the thermal spraying processes are: the source of energy, responsible for heating the material to a molten or semi-molten state, and the medium, which helps the material particles to accelerate before they are deposited on the substrate. The most important thermal spraying methods are: flame spraying, wire arc spraying, plasma spraying, detonation spraying, laser spraying, high velocity oxygen fuel (HVOF) spraying and cold spraying. The spraying can be performed in ambient air, vacuum, inert or active gas or water. The properties achieved include wear resistance, electrical and thermal insulation, corrosion resistance, biocompatibility, bioactivity, catalytic activity, optical transparency, magnetism, etc. [41, 52, 112, 166, 192, 198]. The research concerning nanomaterials for industrial applications focuses on Al_2O_3, WC-Co, TiO_2, ZrO_2, Y_2O_3, and hydroxyapatites. Thermal spray nanostructured coatings are produced from powders or suspensions containing nanocrystalline particles typically 15-53 μm in size [44, 88]. It is thus possible to create composite coatings with properties different from those of their constituents.

Today, much attention is being paid to tungsten carbide as a coating material, as it is well capable of improving the wear resistance and, accordingly, the durability of machine parts. The WC-Co coatings, comprising hard WC particles embedded in the cobalt matrix, are now commonly deposited using high velocity oxygen fuel (HVOF) spraying. The plasma spray process is no longer optimal to produce WC-Co coatings, as the high-temperature plasma jet and the presence of oxygen considerably contribute to the decomposition, decarbonization and oxidation of WC. The resulting changes in the phase compositions have a significantly negative effect on the performance of WC-Co coatings. The HVOF spray process, with a relatively low temperature flame and a short dwell time, prevents these phenomena effectively. Another solution to improve the quality of WC-Co coatings is the use of nanostructured powders with tungsten carbide nanocrystals. The addition of nanocrystalline Fe_3O_4 particles to act as a solid lubricant should further contribute to better tribological properties of these composite coatings.

Chapter 2

Processes and Phenomena Involved in the Formation of Thermal Spray Coatings

Thermal spraying is a group of processes in which ground metallic and non-metallic material is deposited in a molten, highly-plastic or solid state on a specially prepared substrate. When hitting the sprayed coating, the particles deform, adhere to it and, by dropping one onto another, form a layer with a characteristic lamellar microstructure.

From the scientific standpoint, in the processes of thermal spraying, the velocity of the coating material particle and its temperature at the moment of hitting the sprayed surface have a vital impact on shaping the deposited coating microstructure. These parameters, together with the surface temperature are decisive in terms of constituting the coating, its properties and the efficiency of the spraying process. Particle velocity and its temperature are the result of many factors being the outcome of the applied thermal spraying process, the coating material properties and the technological parameters applied. Thermal spraying processes provide a plethora of possibilities of generating a gas stream with a very diverse range of velocity and temperature, from relatively low velocities and very high temperatures during thermal spraying to very high velocities during cold gas spraying (Fig. 2.1). It directly affects the particles present in the stream, their behaviour at the moment of hitting the surface and, in consequence, the properties of coatings.

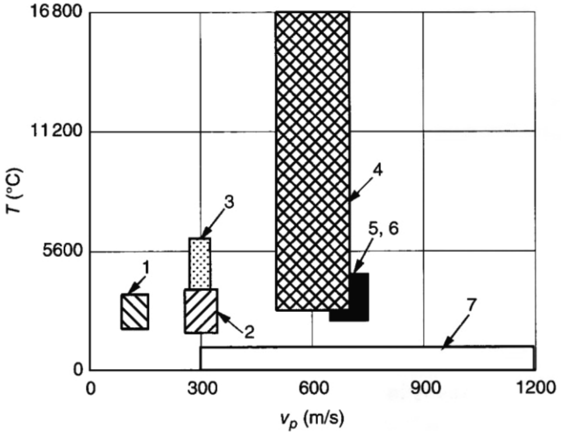

FIG. 2.1. Diagram of jet temperatures (T) and particie velocities (v_p) used in different spraying methods: 1 – low-velocity gas, 2 – high-velocity gas, 3 – electric-arc, 4 – plasma, 5 and 6 – detonation and high-velocity oxygen fuel, 7 – cold spray.

Velocity of coating material particle as well as its temperature while hitting the surface is the result of physical and chemical processes which begin when the particle enters the gas stream. Then, as a consequence of the impact of the stream, the particle starts to heat and accelerate simultaneously. Mutual interaction of the particle and the hot stream of gases results from the impact of such forces as:

- aerodynamic drag,
- aerodymanic lift,
- pressure gradient (Archimedes force),
- added mass force related to the particle acceleration,
- Basset history term,
- shear lift,
- forces caused by particle rotation (Magnus force),
- jet force in the case of evaporating particle.

In the case of thermal spray processes, only the coefficient of aerodynamic resistance is taken into consideration and then particle acceleration in the gas stream is illustrated by the equation (2.1) [54, 109, 112, 134]:

$$\frac{1}{6}\rho_p\, \pi d_p^3 \frac{dv}{dt} = \frac{1}{8}\, C_D \pi d_p^2 \rho_g (u - v)^2 \tag{2.1}$$

where: u – gas velocity, v – particle velocity, d_p – particle diameter, ρ_p – particle density, ρ_g – gas density, C_D – coefficient of aerodynamic resistance.

Value of the C_D coefficient depends on the trajectory of the particle motion in relation to the stream of gases in the following manner:

$$C_D = \frac{24}{Re}, \quad Re < 0.2 \tag{2.2}$$

$$C_D = \frac{24}{Re}\left(1 + \frac{3}{16} Re\right), \quad 0.2 \le Re < 2 \tag{2.3}$$

$$C_D = \frac{24}{Re}(1 + 0.11 Re^{0.81}), \quad 2 \le Re < 21 \tag{2.4}$$

$$C_D = (1 + 0.189 Re^{0.632}), \quad 21 \le Re < 200 \tag{2.5}$$

where:

$$Re = \frac{\rho_g d_p (v_g - v_p)}{\eta_g} \tag{2.6}$$

η_g – gas dynamic viscosity.

In the equation (2.1), a spherical shape of the particle was assumed. This shape concerns a wide range of powders applied in the processes of thermal spraying, obtained especially by the gas atomisation method. Spherical shape of the powder grain can also be assumed for non-spherical grains which possess a high coefficient of thermal conductivity, and after entering, especially the plasma stream, they take on a desired shape. While determining the Reynolds number, one should take into account the fact that grain diameter can be subject to change as the result of evaporation from its surface. Also, gas dynamic viscosity as well as its density depends on the differences between the gas and the grain temperature. With miniscule temperature differences, the values corresponding to the gas temperature are assumed. Whereas with major temperature differences, the values corresponding to the average temperature of the boundary layer are taken into account. It is also vital to consider momentum alterations of the gas stream connected with inserting powder into it. In the case of inserting a huge amount of powder, the intensity of its heating together with its velocity decrease.

The process of heating powder grains in the gas stream takes place in the form of convection, conducting and radiation. The convection process plays an important role directly after inserting the grain into the gas stream, where the hot gas has a much higher velocity. Heat is transferred inside the grain by conductivity. Coefficient of thermal conductivity plays an important role in this process. When it value is low or when the grain is huge, then the process of its thermal diffusivity in the grain can be substantially longer than achieving the melting point on the surface of the grain. Usually, two cases of grain heating are taken into consideration: non-gradient heating, when the grain lacks temperature gradient and gradient heating, when the temperature inside the grain differs from the one outside. Radiation process from the stream to the grain and vice versa is analysed for the grains with a huge diameter [54, 112].

For the particles whose material possesses a high coefficient of thermal conductivity or tiny grains conducting heat inefficiently and being present in the hot stream of gases for a considerable time, the thermal balance equation is in the following form (2.7):

$$\pi d_p^2 h\left(T_g - T_p\right) + h_r\left(T_g\right) = \frac{1}{6}\pi \rho_p c_p d_p^3 \frac{dT_p}{dt} + \pi d_p^2 \varepsilon_p \sigma T_p^4 \tag{2.7}$$

where the left side of the equation (2.7) describes the heat flow as the result of convection, conductivity and radiation, whereas the right side describes the heat absorbed by the grain: h – coefficient of heat conductivity, ρ_p – particle material density, ε_p – coefficient of particle material emissivity, σ – Stefan-Boltzmann constant.

In the case of gradient heating in the grains from the material with a low coefficient of thermal conductivity or grains conducting heat efficiently but being present in the stream of gases for a short time, the thermal conductivity equation needs to be solved (2.8),

$$c_p(T)\rho(T)\frac{\partial T}{\partial t} = grad(\lambda(T)gradT) + q \tag{2.8}$$

where: q – heat stream intensity.

Varied condition of the grain during its heating is taken into consideration while solving the equation; the grain is in uniform state of matter, there is a movable boundary of state of matter in the grain and the grain surface evaporates, whereas the middle part of the grain is close to the melting point.

In the processes where low stream temperature and its high velocity occurs, the particle is not molten at the moment of impact, it is deformed due to a conversion of kinetic energy of the grain into its plastic deformation with heat emission. Particles are not subject to melting; this allows to obtain a coating with a tiny number of oxides and a low level of internal stresses. Particle temperature can be determined from the following relation (2.9) [109]:

$$\rho_p v_p c_p \frac{dT_p}{dz} = Nu\frac{6\lambda_w}{d_p^2}(T_0 - T_p) \tag{2.9}$$

$$Nu = 2a + 0.459\, b\, Re_{p0}^{0.55} Pr^{0.33} \tag{2.10}$$

$$a = \exp(-M_{po})\left(1 + \frac{17M_{po}}{Re_{po}}\right)^{-1} \tag{2.11}$$

$$b = 0.666 + 0.333\exp\left(-\frac{17M_{po}}{Re_{po}}\right) \tag{2.12}$$

where: Nu – Nusselt number, Pr – Prandtl number, M – Mach number, λ_w – wave length between two neighbouring tops of jet distribution, p_0 – stagnation pressure, T_0 – stagnation temperature.

The particle that hits the substrate should have a set velocity and temperature, regardless of the applied spraying process. Within the range of lower velocities (Fig. 2.1), it ought to be completely molten. This allows its deformation which facilitates filling the surface irregularities. Such a coating has a tiny number of pores and density approximate to a solid material. In the case when the particle temperature is higher than the melting point, then evaporation from its surface can occur, which lower the efficiency of the spraying process. If the particle possesses Temperature lower than the melting point, then it adheres to the substrate to a lesser degree, which causes the increase in coating porosity and lowers its properties. Within the range of high velocities (Fig. 2.1), kinetic energy of the particle is the factor which determines its deforming and constituting the coating. The melting process of the grain can be very complex considering differential grain morphology of the currently-applied composite powders on the example of WC-Co (Fig. 2.2).

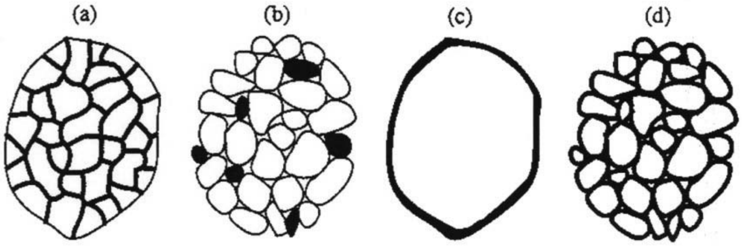

FIG. 2.2. Different morphology of WC/Co composite particle: a) sintered and crushed, b) pelletized and sintered, c) coated, d) coated and pelletized, o – WC, ● – Co [52].

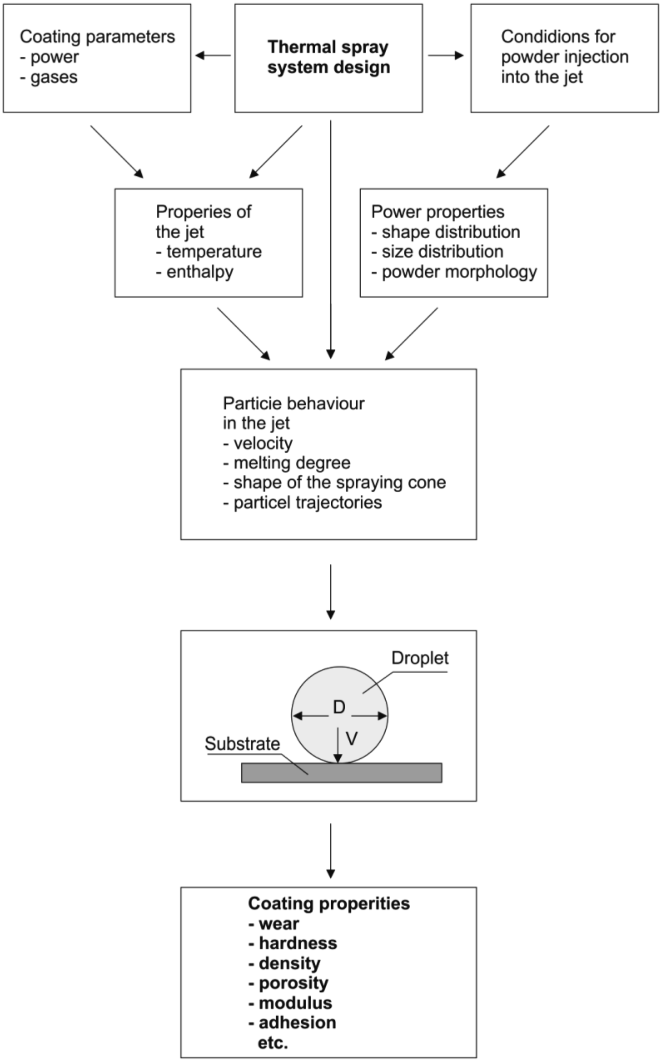

FIG. 2.3. Interdependencies of the main thermal spray parameters.

The influence of basic factors affecting the velocity and temperature of the coating material particles and, in consequence, the properties of the sprayed coating are shown in Figure 2.3.

The basic element of the coating obtained as a result of thermal spraying is the deformed powder grain, which, as a consequence of hitting the surface, fills surface irregularities and solidifies by taking on the shape of a lamella. Such a course of the spraying and coating formation processes leads to the occurrence of pores being the result of an irregular distribution filling in the substrate by the solidifying particle. Moreover, oxides and new phases can appear in the coating as a consequence of the impact of the spray stream atmosphere onto the particle. Lamella can retain chemical and phase composition of the coating material depending on the spraying conditions. A very rapid course of the solidifying process leads to the occurrence of internal tensions, which, in turn, can lead to microcracks in the lamellae, and, in extreme cases, to cracks on the sprayed coating. In the case of a composite coating spraying, the coating comprises purposefully inserted new phases resulting from the properties of an additional material and its interaction with the gas stream.

In the coating formation process, it needs to be considered that a fully-shaped coating is composed of a few other layers resulting from a distribution of particles in the spray stream cross-section and its velocity in relation to the sprayed surface of the element. Spray stream usually has a circular section where the particle velocities and temperature are the lowest at the edges, and their number and distribution depend on powder feed rate. At the moment of commencing the spraying process, when the spray stream starts moving against the element, the particles with the lowest temperature and velocity reach its cold surface first.

The coating which formed by them, and already has increased temperature, is reached by the particles from the stream centre with the highest velocity and temperature, thus causing further temperature increase. The grains (with the same velocity and temperature like the ones that reached the surface as the first) from the remaining part of the stream are deposited on a coating heated in such a way. On the basis of the conducted analysis, it can be assumed that a single layer is composed of three sublayers of different microstructure with a gradual transition among them. The properties of the first of the sublayers are much poorer than those of the one deposited directly on it. The last sublayer possesses intermediate properties between them. Too high stream transfer temperature reduces the beneficial effect of the increased temperature of the coating. In addition, powder too feed rate causes an increase in thickness of the first sublayer, which has an undesired influence on the properties of the whole coating.

Coating porosity, which occurs during spraying, is the feature that substantially influences its properties. In a vast majority of applications minimizing this phenomenon is of utmost importance due to lower coating cohesion, it also reduces its corrosion resistance and accelerates wear. Porosity is increased with the presence of minimally deformed grains or the ones which were merely subject to seizure. This, in turn, leads to cracks in the coating, its delamination and shelling. Such shelled hard grains, especially in anti-wear applications, cause an accelerated wear of the coating. Open porosity in the coating enables direct corrosion of the substrate. Nevertheless, in some applications it is desirable. In the coatings constituting heat barriers 15% porosity significantly increases its insulation properties, and the porosity of the sprayed coatings can reach up to 50% in order to increase its surface [134]. Additionally, a high level of coating porosity is desired in slide bearings which are saturated with oil or a solid lubricant.

On the basis of such illustration of the thermally-sprayed coating formation process, its demonstrative model can be created (Fig. 2.4). This model includes the impact of the factors present during its formation.

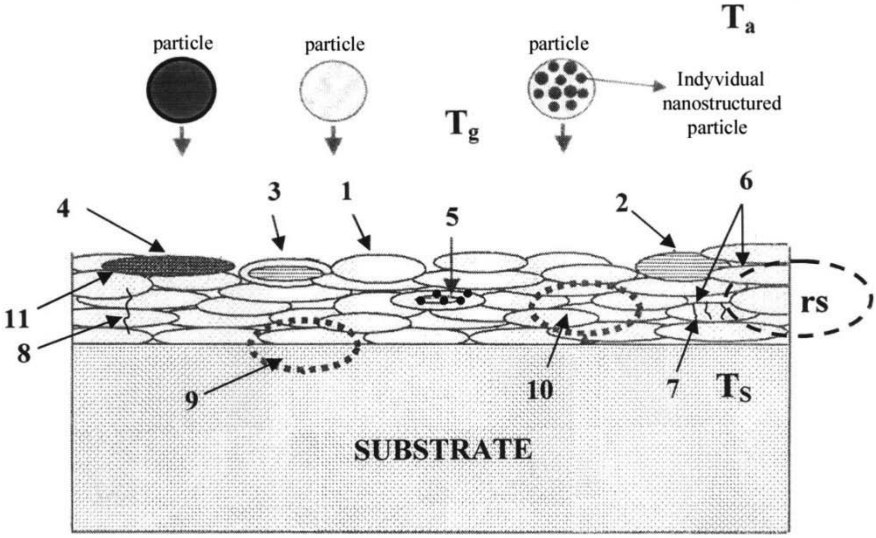

Fig. 2.4. Model illustrating the elements of microstructure of the thermally-sprayed coating and the factors influencing its properties: 1 – lamella with an original phase composition and grain size, 2 – lamella with an original phase composition and varied grain size, 3 – lamella with a core possessing an original phase composition, 4 – lamella composed of the new phase, 5 – lamella with a nanostructured construction, 6 – pores, 7 – cracks in the lamella, 8 – cracks comprising several lamellae, 9 – adhesion between the lamellae and the substrate, 10 – cohesion between the lamellae, 11 – adhesion between the lamellae with a varied phase composition; *rs* – internal stresses in the coating, T_g – gas stream temperature, T_s – temperature of the substrate, T_a – temperature of the atmosphere.

When hitting the substrate, powder grain is in the melted, high-plastic or solid state and possesses certain velocity depending on the place and the its residence time in the spray stream.

It determines the shape and the internal structure of the lamella. Its solidifying process is very rapid and exceeds 10^6 °C/s. Both the temperature of the substrate and its physicochemical properties also influence the process of deformation and solidification of the lamella. A very short period of time from particle adhesion to the substrate to its deformation and complete solidification inhibits the analysis of the phenomena which significantly decide about the properties of the sprayed coating.

Moreover, taking granulometric distribution of the applied coating material into consideration (which comprises significant differences of particle sizes together with their different thermal and kinetic energy), a coating is composed of lamellae with a substantially diverse level of deformation and internal structure. Typical structures of lamellae are shown in Figure 2.5. Non-deformed grains, which are subject to seizure in the substrate irregularities, can also be present in the coating. They are poorly adhered to it and lower the properties of the coating.

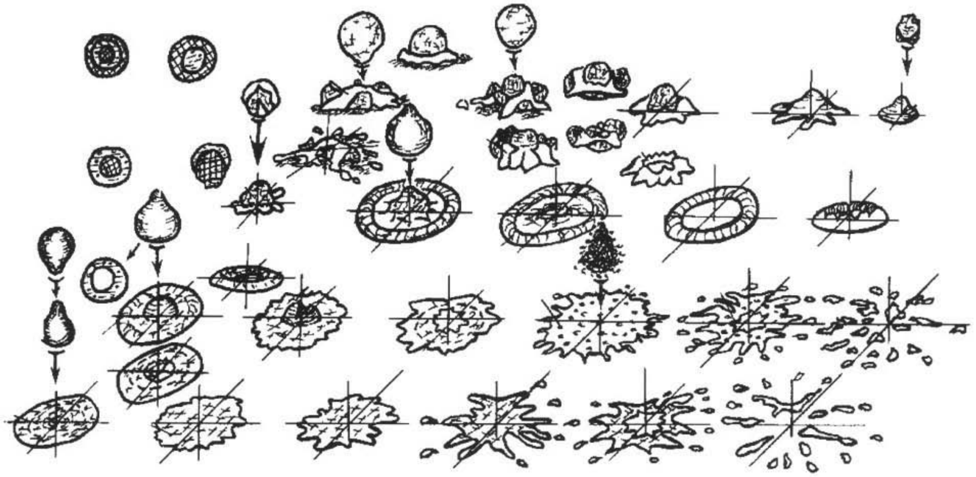

FIG. 2.5. Typical shapes of thermally-sprayed lamellae and powder grain morphologies [134].

Adhesion between the lamella and the substrate as well as cohesion between the lamellae themselves are a decisive factor in the quality of the thermally-sprayed coatings. Mechanical seizure in the irregularities of the substrate is considered to be the basic process determining the adhesion of the lamella to the substrate. For this reason, the substrate is purposefully prepared in order to obtain proper porosity. Either rough turning or abrasive blasting is applied. After processing, the substrate not only possesses appropriate porosity but it is also clean and active. Lamella can also be obtained on a smooth substrate, which proves the point that other factors affect coating adhesion as well. Diffusion of the coating material to the substrate (and the other way round) can additionally occur between the sprayed lamella and the substrate. Taking a wide range of temperatures and hitting grains velocities into consideration, the possibilities of the occurrence of chemical reactions, surface energy alterations or electrostatic forces also need to be taken into account. Bonding forces of the lamella to the substrate or to a neighbouring lamella F_w can be noted as a constituent of the following elementary forces (2.13):

$$F_w = F_m + F_{ad} + F_{koh} + F_{dyf} + F_{chem} + F_{epit} \tag{2.13}$$

where: F_m – mechanical bonding force, F_{ad} – adhesive bonding force, F_{koh} – cohesive bonding force, F_{dyf} – diffusive bonding force, F_{chem} – chemical bonding force, F_{epit} – epitaxial bonding force.

Ultimate bonding force F_w is a superposition of particular components and their weight depends primarily on the temperature and particle velocity or substrate properties, i.e. the material, porosity, temperature, wettability etc.

Molten metal grain covered with a layer of oxides can be considered as the basic case (Fig. 2.6a). The tiny layer of oxides may be subject to breaking while hitting the substrate. Consequently, the substrate, which can be covered with a fine layer of oxides, can directly contact the sprayed metal (Fig. 2.6b). In this situation, adhesive bonding between the layer of oxides and metal grain takes place. When the layer of oxides remains on the deformed lamella (Fig. 2.6c), adhesion bonding takes place between the layer of oxides of the substrate and grain oxides. Partial perforation of oxide layers is also possible and then the cohesion force results from the ratio of direct contact of the oxides and metal (Fig. 2.6d). Analogical deliberations also concern the bonding present in the layer between the lamellae. Physical interaction between substrate atoms and the lamellae is the result of the van der Waals forces (physisorption). The interaction is possible when both surfaces of lamellas are clean, close to each other at the distance of atom reaction and are activated by, e.g. as a result of plastic deformation. If the exchange of valence electrons occurs between atoms, then the phenomenon of chemisorption can appear. The creation of chemical compounds between the lamella and the substrate often causes tight metallurgic bonding.

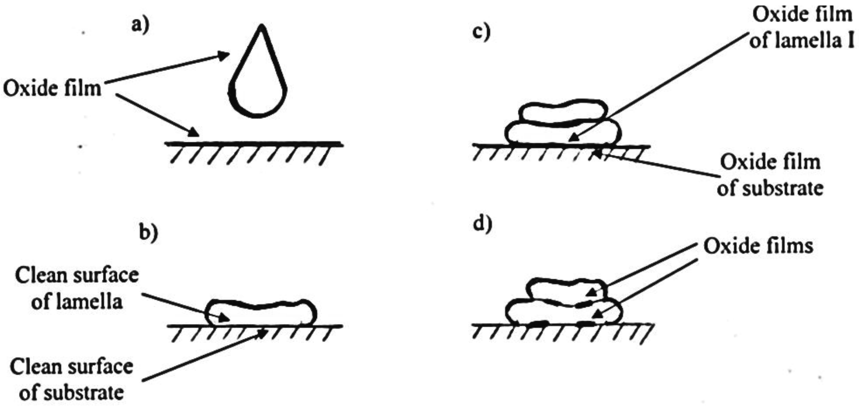

FIG. 2.6. Typical situations appearing at the impact of composite particle into the substrate: a) a particle before impacting the substrate, b) direct contact of the sprayed metal grain with the substrate, c) contact of the fine layer of oxides with the lamellae oxides, d) a mixed situation (b + c).

In the case of spraying composite grain consisting of two phases, one of which constitutes a solid lubricant (Fig. 2.7a), bonding forces are the result of bonding these phases to the substrate (Fig. 2.7b). In the case of the contact between the lamellae the situation is analogical. Cohesion is likely to occur if the same phases from the neighbouring lamellae are adhesive (Fig. 2.7c) whereas adhesion appears if there is contact of various phases (Fig. 2.7d).

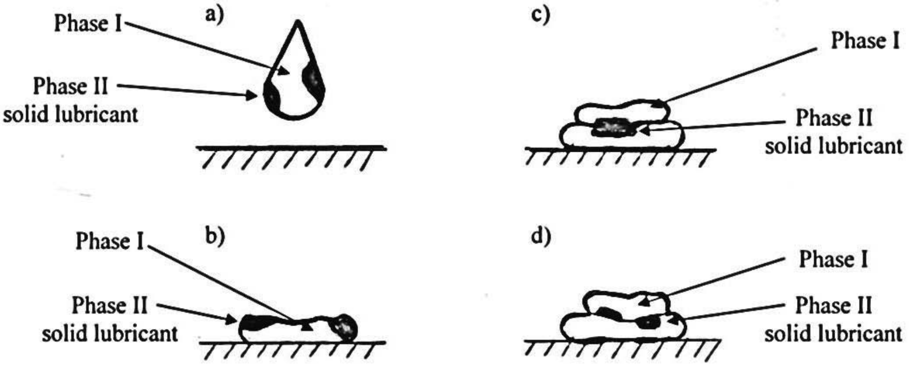

FIG. 2.7. Typical situations occurring at the impact of the composite particle into the substrate: a) a particle before impacting the substrate, b) direct contact of the sprayed composite grain with the substrate, c) contact of the areas of the same phase, d) contact of the areas from different phases.

Having analysed the above situations, one can draw a conclusion that in the case of composite materials the coating cohesion as well as its adherence to the substrate are lowered. It means that the presence of a solid lubricant in a coating needs optimization every single time.

In the cases when the deformed particle takes on discus shape the coefficient of flatness ξ (set out by Madejski on the basis of dependence) can be determined as follows (2.14) [54, 112]:

$$\xi = \frac{D_s}{d_p} = 1.2941\left(\rho\frac{v}{\eta_p}\right)^{0.2} \tag{2.14}$$

Coefficient ξ takes the following into consideration: surface tension, viscosity and particle solidification; yet, it does not take heat gradient alterations in the particle into consideration thus constitutes the basis for further analysis. The coefficient of flatness taking particle mass losses and surface porosity into account is illustrated by the following formula (2.15) [134]:

$$\xi = 0.845\sqrt{\chi}\,Re^{\frac{1}{4}}\{1 - 0.06\sqrt{\gamma}\sqrt{Re}\} \tag{2.15}$$

where: χ – a non-dimensional parameter determining the loss of mass by the particle, γ – a non-dimensional parameter determining porosity called the ratio of the irregularity level ε to particle radius r_p.

It appears from the relationship (2.15) that the level of particle flatness diminishes with surface porosity increase, i.e. a porous surface leads to an increase in friction between the splashing particle and the surface, thus limiting grain flattening.

Both the particle size and real conditions of conducting the spraying process (mainly surface wettability, thermal conductivity, the angle of grain impact into the substrate, and oxidation of the lamella deposited on the surface) determine the ultimate shape of the lamella. Fine grains, nanometric in size (which are sprayed in the form of a slurry), are far less subject to splashing as the forces of surface tension inhibit this process considerably.

Increased surface temperature causes its higher level of wettability, which also affects the course of the lamella solidification process and its ultimate shape. Together with the increase of surface temperature, the splashed-shaped lamella, typical for lower temperatures, takes on more convenient disc shape. Its microstructure is fine-grained in the directly adherent area to the substrate. It is the outcome of much better contact of the lamella with the substrate, which is the result of removing the absorbed fine layer of gases and condensates. It enables close contact and increased heat flow between the solidifying particle and the substrate. Moreover, in the nanometric scale his roughness increase as result of oxidation induced by high temperature. It cause growth of substrate wettability in contact with the molten particle. All the above-mentioned factors lead to increased viscosity of the particle and limit its splashing during its deforming, which favours the creation of discus-shaped lamellae [178]. The impact of the physico-chemical state on the course of shaping the lamella was confirmed in research, where the surface of the burnished stainless steel sample was covered with three different organic substances (xylene, glycol and glycerol) with various boiling points. If the temperature of the sprayed coating was lower than the boiling point of the deposit, then it created favourable conditions for splashing the particle during its deforming and obtaining lamellae with an irregular shape. Substrate temperature exceeding the temperature of the deposits by 50°C caused evaporation of all the organic substances which were absorbed on the substrate. This resulted in obtaining discus-shaped lamellae without the splashing process. Identical behaviour was observed for Al, Ni particles and for Al_2O_3 [80].

Temperature of the neighbourhood gas stream has also a significant influence on the course of the deforming powder grain process. If it is above the melting point of gases, then it delays the process of lamella solidification, thus facilitating its shrinking. High temperature of gases also leads to increased adhesion of the lamella with the substrate in comparison with the gas of lower temperature [1, 38].

The properties of a thermally-sprayed coating are the result of series of physical, chemical processes as well as technological parameters of depositing.

Two main stages can be distinguished during the course of this process. In the first phase, from the moment of grain insertion to the gas stream until its contact with the substrate, the reciprocal interaction of the coating material with the gas stream is vital. Both kinetic and thermal energy are conveyed to the particles depending on their sizes and morphology, physic-chemical properties of the material from which they were made and the placing in the spray stream. In the next stage, the process of deformation and solidification of the grains takes place. Creating of the coating during the process of thermal spraying needs optimisation which depend on technological conditions and the aim of coating forming.

Chapter 3

Coatings Containing Solid Lubricants

Materials which have been applied as a solid lubricant can be divided into two groups: substances with small internal cohesion and substances with anisotropic cohesion, i.e. those in the form of layers. Soaps, waxes, polymers and soft metals belong to the first group, whereas graphite, molybdenum and tungsten disulphides, a few oxides, hydroxides, halides, nitrides and sulphides belong to the second group [53, 76, 120]. Crystal materials with layer structure have distinct slide and cleavage planes which run along particular layers. In such compounds, atoms placed in flat layers are fixed with covalent bonding, which is much stronger than electrostatic bonding, present among the layers. It is quite common for the same compound to crystallize in a few polymorphic types which do not have the properties of a solid lubricant. Crystal cohesion is vital in this case, which is substantially influenced by a mutual relationship of crystallographic dimensions a_0 and c_0, known as the axial relationship. With an increase in the a_0/c_0 ratio, mutual interaction of layers becomes easier. When the a_0/c_0 ratio equals 2, it enables free interaction of parallel layers (for MoS_2 it is 1.93; whereas for WS_2 – 1.96). Adhesion of a solid lubricant to the substrate is also of high importance. It can be mechanical in its form when the applied solid lubricant is rubbed into the ruggedness of the coating-substrate interfaces. Chemical adhesion occurs when lubricant reacts with the substrate forming a chemical compound. The value of adhesion has to exceed action of tangential forces during slipping, even at high load. Otherwise, material which do not possess enough high adhesion to the substrate cannot be used as solid lubricant. For this reason, different techniques are implemented in order to increase the value of adhesion.

Solid lubricants are in many cases very good solution enabling flawless interaction of rubbing elements. Their mechanical as well as chemical resistance is much greater than the one of plastic and liquid lubricants; that is why their application is more varied. It is of paramount importance when friction pairs operating in adverse conditions must meet specific requirements, i.e. coefficient of friction must not exceed a certain value, the wear of coating-substrate interfaces must not exceed a given value either and the durability of such a pair, with a certain level probability, must be longer than its demanded operating time. Given these facts, research on elaborating new solid lubricants and their applications is conducted. Although solid lubricants are successfully used in diverse operating, temperature and environmental conditions, there are certain limitations in their applications. Most solid lubricants, except for soft metals, have a low coefficient of thermal conductance. This substantially limits the heat transfer directly from the coating-substrate interfaces. Depending on the surrounding and operating conditions, the coefficient of friction can change and reach high values. Oxides being the result of the reaction of oxygen present in the atmosphere with the metallic substrate, frequently are solid lubricants. They prevent the coating-substrate interfaces from seizing. During the interaction of elements in vacuum, the lack of oxides on the substrate increases the friction coefficient, initiates the process of adhesive wear and seizing [53, 120]. During long operating time, there might be problems with oxidation of solid lubricants and their ageing, as is the case with transition-metal dichalcogenides. In the case of operating at a high temperature or in an oxidative environment, irreversible phase changes in solid lubricants may occur. This may result in losing their lubricity properties; furthermore, hard phases may appear, which accelerates wear. What is more, solid lubricants also use up and their exchange is more complicated in comparison with liquid lubricants. For this reason, research is conducted on new solid lubricants and the methods of their application in the friction pair in order to reduce its coefficient of friction and increase its durability (Fig. 3.1) [33].

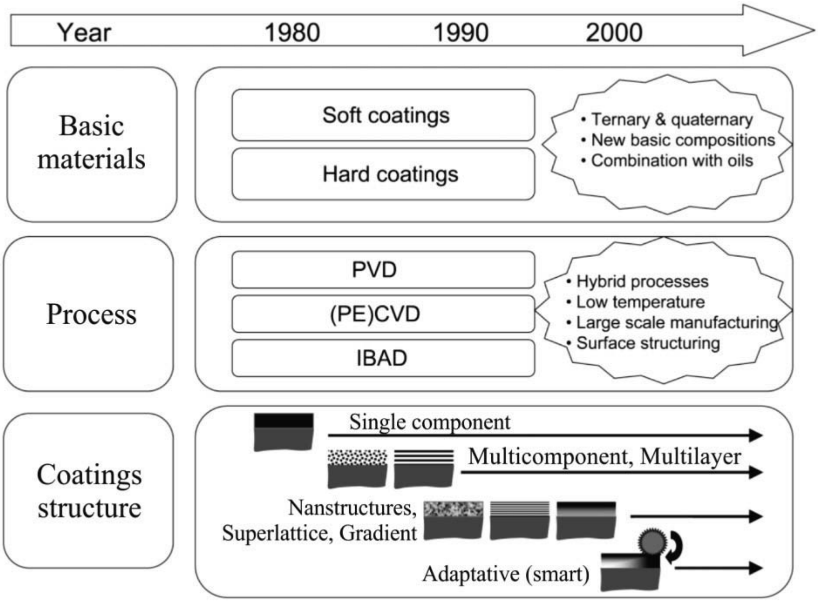

FIG. 3.1. Historical development of tribological coatings and solid lubricant films [33].

The PVD methods create new opportunities where DLC (diamond-like carbon) films are particularly promising, because they have a very low coefficient of friction [12, 39, 94, 156]. Mo-S-C films embedded by the PVD method with a various amount of carbon had a very low coefficient of friction ($\mu = 0.015$) in mating with 100Cr6 steel ball in a nitrogen environment. The XRD examination of its microstructure has revealed the presence of MoS_2 grains (ca. being a dozen or so nanometres large) in the carbon matrix [116]. The GLC (graphite-like carbon) film embedded on very hard substrates from Si_3N_4, SiC, and WC also enabled a significant lowering of the coefficient of friction in water environment [170]. Hybrid techniques which combine the best characteristics of particular methods are being developed. The ECS (Electrostatic Spray Coating) and the CVI (Chemical Vapour Infiltration) methods were applied to accomplish a fusion of boron and cubic titanium nitrides (cBN-TiN). The obtained hard layer had a topography resembling that of lotus leaves. The spaces created among the elements of substrate structure acted as suppliers for MoS_2 embedded as a result of barrelling. It caused reduction in substrate porosity and more than twofold lowering of the friction coefficient. The obtained value, i.e. $\mu = 0.28$, for coating cBN-TiN/MoS_2 mating with stainless stell ball, was comparable to the values obtained for MoS_2 layers embedded by the PVD method [176]. Research of low-friction WC/C and Ni/Cr-Cr_3C_2 coatings produced by this method are conducted by Institute for Sustainable Technologies National Research Institute in Radom [99, 100, 101, 149] in Koszalin University of Technology [28, 96, 108] and Lodz University of Technology, too [111]. The use of graphite is also being tested [120]. Graphite, despite its relatively high decomposition temperature (it is heat resistant in the air atmosphere up to 500^{o}C, whereas in the vacuum up to 3500^{o}C), requires additional protection in the form of nickel layers in the case of application in thermal spray processes. Dies sprayed with a graphite-powder coating, the grains of which had been coated with a 5-µm nickel coating, substantially improved stamping sheets of steel [160]. Graphite layer, embedded by the sol-gel method, had an excellent adhesion to the substrate and led to a significant lowering of the coefficient of friction [168]. Research on leaded tin bronze obtained by the powder metallurgy method with various contents of graphite showed that its 3% addition enabled obtaining the highest resistance to wear and the lowest coefficient of friction [92]. Moreover, the presence of graphite in a hybrid Cu-TiC composite, which was sintered with the use of microwaves, increased its tribological properties. Due to the content of both TiC hard grains and graphite its wear and coefficient of friction were lower than in the case of pure copper. The obtained self-lubricating transitory carbon coating prevented carbon oxidation in a wide range of hybrid composite parameters [123]. The application of titanium and its alloys contribute to limiting their unfavourable tribological properties. Applying graphite onto the coating obtained on the titanium alloy by the method of microarc oxidation allowed fivefold reduction of the coefficient of friction in comparison with a coating without graphite [174]. The powder metallurgy method was applied in order to make a composite consisting of Ni matrix with an addition of silver and hexagonal boron nitride (h-BN). Similarly, the coating containing solid lubricants was obtained during the operating time of the tested composite, which reduced wear five times as opposed to the Ni matrix without the above-mentioned additions. However, no synergic interaction of both solid lubricants was observed, mainly because h-BN formed a strongly adherent layer on a counter sample [162].

Solid lubricant can be applied in the form of specially prepared mass with bonding additions, which is used to fill in grooves bored on the interacting surface. The same solution was used to increase durability of piston rings, where the grooves in pistons were filled in with Fe_3O_4, sodium metasilicate, and water. Next, pistons were soaked to evaporate water from the mixture and underwent finishing [66].

The effect of using solid lubricants within friction pairs can be substantially enhanced due to the texturizing process of the coating-substrate interfaces. Substrate texture is depicted as areas regularly appearing on the substrate, which have a distinct topography (Fig. 3.2). They may also have other physicomechanical or physiochemical properties than the rest of the substrate coating.

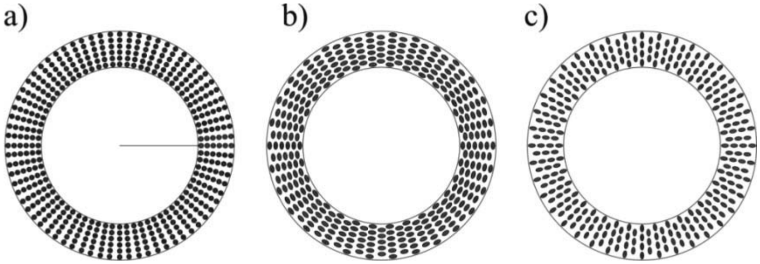

FIG. 3.2. Dimple shapes and arrangements (a) circular, (b) elliptically shaped circumferentially oriented, and (c) elliptically shaped radially oriented [122].

Areas composing the texture are shaped due to the use of other parameters or technologies than those applied in substrate processing. Different techniques of modifying substrate topography, e.g. machine cutting, etching, applying ion and laser beams, and electric arcs are used to obtain micro-dimensional structures on the substrate which compose solid lubricant suppliers [104, 122, 126]. Cloth burnishing is a technique used for injecting solid lubricants. Such an application of molybdenum disulphide onto the texturized substrate by PAAT (Pulsed Air Arc Treatment) allowed keeping the lubricating film longer by 75% of the operating time than on the abraded substrate. Furthermore, adding stearin to solid lubricants caused a threefold increase in the durability of the film parallel with lowering the coefficient of friction to $\mu = 0.1$ [104]. Satisfactory results can be also achieved by applying the ball burnishing technique. A mixture of molybdenum disulphide, nanograins of aluminium and stearin led to a more effective decrease of the coefficient of friction than in the case of using pure MoS_2 [103].

Research is conducted on the use of new materials, i.e. fullerenes, with solid lubricant properties [78, 125, 180].

Tribological properties can also be improved by adding the hard phase to composite coating. Supersonically sprayed coating $Fe_{43}Cr_{16}Mo_{16}C_{15}B_{10}$ metallic glass coating with an addition of 8% WC-12Co exhibited a lower coefficient of friction and wear and increased hardness than a coating without the addition of the hard phase [154].

Thermal spraying techniques provide a wide range of possibilities of applying solid lubricants onto the surfaces of mating machine elements (Table 3.3) [15, 52, 112, 134, 171, 172, 190, 191, 192, 195, 196]. The application of the coating material with a solid lubricant for spraying results in obtaining a thin film. It can be coated onto a given element which can operate in a wide range of conditions. Utilizing molybdenum disulphide in the process of thermal spraying allows improving considerably operating conditions of the interacting elements. Taking high temperatures, present in the spray stream, into consideration, molybdenum disulphide can be subject to decomposition, thus additionally forming MoO_3. Its presence in the friction area is unfavourable due to its hardness. Despite the fact that heat resistance molybdenum disulphide in the air reaches 500^oC, the maximum operating temperature should not exceed 400^oC; however, in the vacuum it retains its properties at 700^oC [53, 120, 138]. A thin nickel coating is used to protect it against harmful effects of temperature. A composite coating obtained by detonation spraying of WC-12Co powder with a 10% addition of MoS_2-Ni exhibited a lower coefficient of friction and wear [36]. The necessity to protect molybdenum disulphide against high temperature of the spraying stream results from its high melting temperature, i.e. 1185^oC. In the case of spraying it in a mixture with WC-Co, its temperature is 307^oC lower than the melting temperature of cobalt, i.e. 1492^oC. Powder grain should reach ca. 2000^oC during detonational spraying, which guarantees the best resistance properties of WC-Co coating. Unfortunately, this temperature causes complete melting of MoS_2 grains, which are subject to decomposition and are not deposited on the substrate. Only lowering the temperature of the spraying stream enables to obtain a coating with molybdenum disulphide [138]. Preparing composite powder is more expensive and technologically complex; nevertheless, it facilitates avoiding solid lubricant degradation and improves coating properties. A mixture of WC-12Co powders, copper, and molybdenum disulphide underwent sintering and then crushing. The plasma sprayed coating contained both Cu and MoS_2, and, in addition, the occurrence of copper contributed to considerable lowering the level of tungsten carbide decomposition. As a consequence, WC-12Co/Cu/MoS_2 coating had not only lower coefficient of friction but also increased wear resistance than WC-12Co [182].

Hexagonal boron nitride (h-BN) is the material commonly used as a solid lubricant in thermal spray processes. It has a layer structure like graphite, where atoms present in the planes are bonded with trifold covalent bonds, whilst among the planes there are only weak dispersion forces (Fig. 3.3). Thermal stability at 1000^oC is its main advantage, even in the oxidizing atmosphere.

Al-12Si/TiB_2 composite powder with a 7.7% addition of h-BN obtained by the mechanical synthesis method was devoted to the plasma spray process. The obtained coating contained hexagonal boron nitride, but its presence did not contribute to lowering the coefficient of friction. Wear resistance tests carried out on the ball on disc tester showed a twofold increase in wear of the coating in the case of Al_2O_3 ball in comparison with 100Cr6 steel ball [106, 153]. Supersonically and plasma spray coatings from NiAl powder with a 10% h-BN addition facilitated lowering the coefficient of friction of the obtained coatings; however, the authors did not provide its value [57].

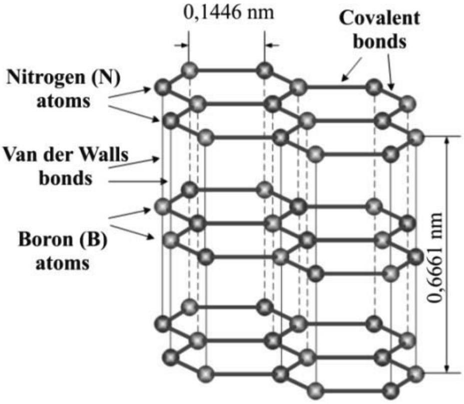

FIG. 3.3. Structure of hexagonal boron nitride.

Using the properties of plastic which have a low coefficient of friction gives new possibilities. Plasma and supersonic spraying conducted with WC-12Co powder with a 6% addition of ETFE (trifluoroethylene) proved that ETFE particles were present in both sprayed coatings. The HVOF-sprayed coating turned out to be better, because the decomposition of WC grains occurred on a smaller scale. It showed a lower coefficient of friction both in the conditions of dry friction as well as in acid environment (5% solution of H_2SO_4) [102]. Another concept is a combination of a hard thermal spray coating with a thin polymer coating on the surface. Such a multi-layer system enables adjusting its properties, i.e. wear resistance, coefficient of friction, adhesion, wettability, and electric properties to working conditions. Supersonically sprayed Cr_2O_3,TiO_2, WC/CoCr, and Mo coatings were then varnished with polyamide-imide. The varnishes contained additions to increase tribological properties of the sprayed coatings; i.e. h-BN, graphite, and PTFE (Fig. 3.4).

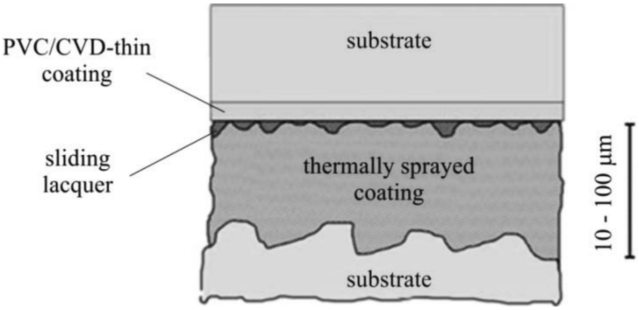

FIG. 3.4. Schematic drawing of investigated system [129].

The countersample was made from carbonized steel coated with DLC. Supersonically sprayed TiO_2 and Mo coatings varnished with a lacquer containing graphite had a much lower coefficient of friction and increased life than the previously-used system, where the DLC coating interacted with the DLC coating [129].

In order to improve sliding properties of the supersonically sprayed coatings, soft metals are also applied. The supersonically sprayed WC-12Co coating was next galvanized with a copper coating which filled the pores present in the sprayed coating. The modified coating had a lower coefficient of friction together with a lower wear in comparison with the sprayed WC-12Co coating [183].

The possibility to use solid lubricants, which are present in numerous machines and devices, at higher temperatures is a particularly interesting issue. At high temperatures (reaching 800°C) a eutectic system of calcium and barium fluorides are applied as solid lubricants. Unlike graphite or molybdenum disulphide used at lower temperatures, they do not have layer structure; nevertheless, their crystal lattices possess planes which enable sliding at high temperatures. Soft metals, e.g. copper or silver are used as solid lubricants to provide proper fiction properties at lower temperatures. Usually, at high-temperature utilizations, the matrix is formed by the material not subject to considerable alterations in its phase composition and which simultaneously provides high resistance to wear at a wide range of temperatures. The plasma spray $WC–(W,Cr)_2C–Ni$ coating with five different contents of silver and $BaF_2–CaF_2$ eutectic system underwent tribological testing at 200, 400, and 600°C. The coating with the largest content of a solid lubricant, i.e. 20% Ag and 20% $BaF_2–CaF_2$ showed the lowest coefficient of friction at every temperature. The wear of coatings was varied at different temperatures, but at 600°C the coating with the largest content of a solid lubricant also had the highest level of wear, whilst the coating without any additions the lowest [22]. High resistance to wear of $WC–(W,Cr)_2C–Ni$ matrix is connected with the creation of $NiWO_4$, $CrWO_4$, and Cr_2WO_6 nanograins. Their presence in the coating is a factor which substantially limits coating wear, especially at high temperatures. The tests conducted at 800°C showed that supersonically sprayed $WC–(W,Cr)_2C–Ni$ coating has a much lower coefficient of friction and wear than WC-17Co coating [56]. $Cr_3C_2–NiCr$ matrix also shows excellent properties at high temperatures (it distinguishes itself by significant hardness and oxidation resistance). Hexagonal boron nitride as well as the eutectic system of calcium and barium fluorides were used to make two composite powders, in which solid lubricants were coated with $Cr_3C_2–NiCr$ matrix as a result of pressure hydrogen reduction. The sprayed coatings had h-BN and $BaF_2–CaF_2$ in its structure, whilst the coating with the eutectic system of calcium and barium fluorides had the lowest coefficient of friction at 800°C.

The Oil-Free Turbomachinery research program has been conducted in the NASA laboratory for twenty years. Its aim is to develop a composite for shaft pivots in bearings placed in air turbines at 650°C. The solution to this problem is based on plasma spray composite coating, in which, depending on operating conditions, the properties of various components are used [55, 148]. The conducted research led to forming PS300 coating, which proved to be useful in many applications; however, in the case of applying it in superalloys, spalling could be noticed, which, in turn, limited its utilization. The modified coating labelled as PS304 consists of 60% NiCr matrix, 20% Cr_2O_3, 10% Ag, and 10% BaF_2-CaF_2. An improvement in the properties of PS304 coatings with composite powders constitutes another stage. Tests carried out on PS304 powder, which is a mixture of NiCr, Cr_2O_3, Ag, and BaF_2-CaF_2 showed that the grains of the components differ considerably both in size and morphology. It influences the diverse behaviour of these grains in plasma stream and it inhibits obtaining a coating with equally distributed components, which lowers its properties. For this reason, composite powder was created, the grains of which contained all the components, and chromium oxide was in a nanorystal form. Plasma spray coating from this sort of powder had a more homogeneous microstructure, increased hardness, and adhesion [179].

Further research led to the development of PS400 coating, which had a new matrix, i.e. 70% NiMoAl as well as 20% Cr_2O_3, 5% Ag, and 5% BaF_2-CaF_2 (Fig. 3.5). Chromium oxide provides high wear resistance in the spray coatings, while silver and BaF_2-CaF_2 eutectic are responsible for the coefficient of friction both at low and high temperatures.

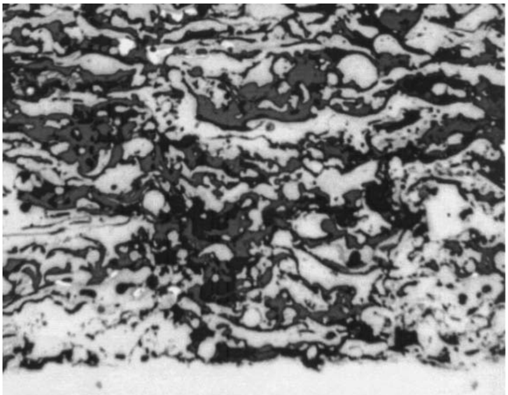

Fig. 3.5. Cross-section of PS400 coating [32].

The newest developed PS400 coating, in comparison with the PS304 one, distinguishes itself with increased size stability at high temperatures in the air, inert atmosphere and vacuum. It is connected with altering the NiCr matrix into NiMoAl composed of 90%Ni, 5%Mo, and 5%Al, which is more resistant to crawling, and the presence of aluminium increases adhesion of the coating (Table 3.1).

The coefficient of friction of PS400 coating collaborating with Inconel X-750 alloy is slightly smaller, while wear, especially at high temperatures, is substantially smaller (Table 3.2). PS400 coating is three to four times smoother than PS304 coating and it not required additional heat treatment to provide dimensional stability, what significantly reducing costs. The issue of insufficient lubrication during turbine start-up at ambient temperature remains to be solved [32, 33]. Plasma spray PS304 coating was also successfully applied to thrust bearings in turbines and piston rods of steam turbine jacks [43, 169].

TABLE 3.1. Comparison of the NASA plasma spray coatings (Oil-Free Turbomachinery Programm) [32].

Coating designation	Binder matrix	Hardener	Solid lubricants	Generall attributes
PS100	NiCr	Glass	Ag + fluorides	Soft-high wear
PS200	Ni-Co	Chrome carbide	Ag + fluorides	Hard-low wear (abrasive to counter face dimensionally stable)
PS300	NiCr	Chrome oxide	Ag + fluorides	Moderate hardness, midly abrasive to counter face, poor dimensional stability unless heat treated
PS400	NiMoAl	Chrome oxide	Ag + fluorides	TBD (Technical Basis Document)

TABLE 3.2. Results of pin-on-disc friction tests (Oil-Free Turbomachinery Programm) [32].

Coating designation	Test temperature, ^{o}C	Friction coefficient	Pin wear, mm^3/Nm	Coating wear, mm^3/Nm
PS304	25	$0{,}31 \pm 0.05$	$96 \pm 30 \cdot 10^{-7}$	$480 \pm 30 \cdot 10^{-6}$
PS304	500	$0{,}25 \pm 0.02$	$32 \pm 5 \cdot 10^{-7}$	$280 \pm 30 \cdot 10^{-6}$
PS304	650	$0{,}23 \pm 0.02$	$38 \pm 4 \cdot 10^{-7}$	$100 \pm 30 \cdot 10^{-6}$
PS400	25	$0{,}31 \pm 0.04$	$141 \pm 28 \cdot 10^{-7}$	$1180 \pm 380 \cdot 10^{-6}$
PS400	500	$0{,}16 \pm 0.02$	$2.1 \pm 0.3 \cdot 10^{-7}$	$6.3 \pm 1.0 \cdot 10^{-6}$
PS400	650	$0{,}21 \pm 0.03$	$8.9 \pm 2 \cdot 10^{-7}$	$7.6 \pm 1.2 \cdot 10^{-6}$

The coefficient of friction can also be decreased with the above-mentioned lubricants operating at an ambient temperature. A 3% addition of gravimetric CaF_2 to Al_2O_3–15% ZrO_2 powder enabled decreasing the coefficient of friction to $\mu = 0.58$ [70]. The conducted testing of WC-12Co composite coating sprayed with an addition of solid lubricants in the form of Cu and BaF_2/CaF_2 proved that with the increase of their content in the coating the coefficient of friction decreases, while the level of wear rises. The coating mating with stainless ball with a 10% addition of copper and 10% addition of BaF_2-CaF_2 had the lowest coefficient of friction ($\mu = 0.02$) and wear [181]. Obtained results of tribological experiments are difficult to compare because of different types of applied tribotesters, countersamples and test conditions (Table 3.3).

TABLE 3.3. Plasma and supersonic sprayed composite coatings with solid lubricant; composition, spraying technique, friction coefficient, applied tribotester.

Ref.	Matrix (% wt.)	Solid lubricant (% wt.)	Method of powder preparation	Spraying technique/substrate	Countersample (shape - material)	Coefficient of dry friction/temperature °C	Coating R_a, μm	Applied tribotester
[102]	WC-12Co	6% ETFE (trifluoroethylene)	Blend	Plasma/Al alloy	Ball ϕ10 - Al_2O_3	0.95	no	SRV[1]
[102]	WC-12Co	6% ETFE (trifluoroethylene)	Blend	HVOF/Al alloy	Ball ϕ10 - Al_2O_3	0.65	no	SRV[1]
[102]	WC-12Co	6% ETFE (trifluoroethylene)	Blend	Plazma/Al alloy	Ball ϕ10 - Al_2O_3	0.17 (5% vol. H_2SO_4)	no	SRV[1]
[102]	WC-12Co	6% ETFE (trifluoroethylene)	Blend	HVOF/Al alloy	Ball ϕ10 - Al_2O_3	0.15 (5% vol. H_2SO_4)	no	SRV[1]
[183]	WC-12Co	Cu	Electrochemical	Plasma/mild steel	Ball ϕ 4 – Stainless steel	0.3	$R_a = 0.5$	BOD[2]
[70]	Al_2O_3-15ZrO_2	3% CaF_2	Blend	plazma/Al alloy	Ball ϕ12.7 - Al_2O_3	0.58	no	BOD[2]
[181]	WC–12Co	10%Cu/10%BaF_2–CaF_2	Sintered	Plasma/mild steel	Ball ϕ 4 – Stainless steel	0.02	$R_a = 0.5$	BOD[2]
[181]	WC–12Co	20%Cu/10%BaF_2–CaF_2	Sintered	Plasma/mild steel	Ball ϕ 4 – Stainless steel	0.14	$R_a = 0.5$	BOD[2]

Ref.	Matrix (% wt.)	Solid lubricant (% wt.)	Method of powder preparation	Spraying technique/substrate	Countersample (shape - material)	Coefficient of dry friction/temperature °C	Coating R_a, μm	Applied tribotester
[181]	WC–12Co	30%Cu/10%BaF_2–CaF_2	Sintered	Plasma/mild steel	Ball ϕ 4 – Stainless steel	0.23	$R_a = 0.5$	BOD[2]
[22]	WC–(W,Cr)2C–Ni	Ag/BaF_2–CaF_2 Different compositions	Blend	Plasma/stainless steel	Ball ϕ 3 – Si_3N_4	0.5/600	no	BOD[2]
[56]	WC–(W,Cr)2C–Ni	–	Sintered	HVOF/stainless steel	Ball ϕ 3 – Si_3N_4	1.1/800	$R_a \leq 0.1$	BOD[2]
[56]	WC–17Co	–	Sintered	HVOF/stainless steel	Ball ϕ 3 – Si_3N_4	0.65/800	$R_a \leq 0.1$	BOD[2]
[59]	NiCr- Cr_3C_2 20-26/64-70	BaF_2–CaF_2 10%	Cladded	Plasma/low carbon steel	Ball ϕ 6 – Si_3N_4	0.4/800	no	BOD[2]
[37]	NiCr- Cr_3C_2 28-7-60	hBN 5%	Cladded	Plasma/superalloy	Ball ϕ 6 – Si_3N_4	0.53/800	no	BOD[2]

Applied tribotester:
1) SRV – ball-disc (oscillating ball movement on disc),
2) BOD – ball on disc,
3) POD – pin on disc.

Another group of coatings, where the presence of solid lubricants is vital, are end seals of compressor blades and turbines in jet engines. Rotating compressor and turbine units require complete sealing in order to eliminate reverse flow of fumes or compressed air through the areas between blade ends and the casing. The occurrence of reverse flows causes losses which lower jet engine efficiency. Standard seals in conventional machine units cannot be applied in this case since they do not meet the requirements set. That is why coatings which must abrade while touching the operating element are applied. In the case of thermally sprayed coatings, they are labelled as abradable coatings. Abradable seals are the coatings sprayed onto the internal surface of the compressor or turbine casing, which has contact with the blade rim of a turbine or compressor. They are treated directly by blade ends, which enables to obtain a very high level of measurement tolerance in the interacting unit. Obviously, the blade end must not be subject to abrasion while contacting the sprayed coating. Diverse materials are applied depending on the area of coating application. In compressors these are different polymers with an addition of such soft metals as aluminium, bronze, or babbitt metal. In the case of turbines, these are composite coatings containing nickel with graphite, NiCr alloy with polyester, or MCrAlY alloy (where M = Cr, Co, Fe) with an addition of polyesters, graphite, hexagonal boron nitride, or bentonite (Fig. 3.6). In the case of applying a coating, the matrix of which is MCrAlY alloy, blade end abrasion may occur as it is not easily-abraded material [10, 52, 62, 91, 93].

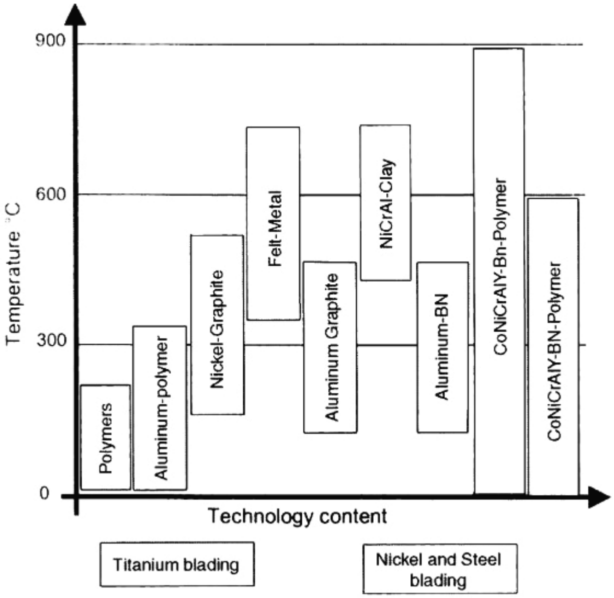

FIG. 3.6. Suggested temperature range for turbine compressor abradables [52].

3.1. Thermal Spray Coatings for Lightweight Engine Blocks

Losses issues due to friction are topical particularly in the automotive business, where only the losses in car engine reach 48% due to this reason (Fig. 3.7) [6, 12, 13, 161].

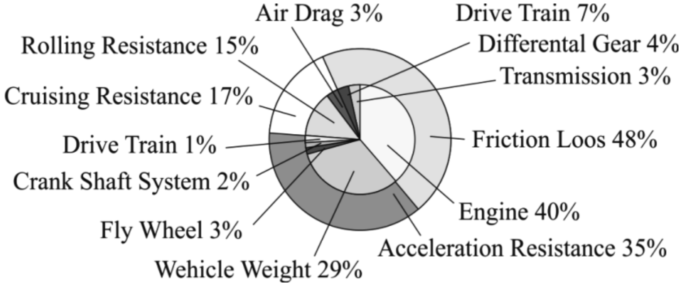

FIG. 3.7. Energy consumption developed in an engine [161].

For this reason, research taking advantage of various thermal spraying techniques is carried out. These techniques enable forming the coatings containing solid lubricants on the substrates of small density. Alloys of aluminium, which are the perfect constructing material, are a huge challenge. However, poor tribological properties limit significantly their wider use. This issue is researched in numerous research and scientific centres which aim to find solutions allowing the application of aluminium alloys in friction pairs. Utilizing the FSP (Friction Stir Processing) method to incorporate a mixture of SiC and MoS_2 into the substrate of the A356 aluminium alloy allowed obtaining a stable and homogenous coating MoS_2-rich and, in consequence, decreasing the coefficient of friction [2]. Such solution cannot be adopted at higher temperatures. 300°C is the maximum ceiling temperature at which molybdenum disulphide can operate; beyond this temperature molybdenum disulphide becomes decomposed and losses its solid lubricant properties. The issue requires a more in-depth analysis since a solid lubricant with a low coefficient of friction at temperatures ranging from ambient to 1000°C does not exist.

The issue of utilizing aluminium alloys particularly concerns the automotive industry, where their use to produce cylinder blocks is closely connected with lower fuel consumption. It is because of a distinct difference in density of cast iron, i.e. 7.8 g/cm^3, used to produce cylinder blocks compared to 2.8 g/cm^3 of silicon-aluminium alloy. Nevertheless, relatively low resistance to wear and common seizures exclude it from utilizing. For this reason, numerous tests are carried out to take advantage of all the merits of aluminium alloys. New possibilities create hard anodizing technology of cylinder lines carried out on aluminium alloys composite materials, which is applied in industry [139, 175]. The application of cast-iron sleeves in aluminium engine blocks was a partial solution to the problem. However, such a construction has several flaws; the distance between the cylinders becomes larger and this increases the weight of the engine. Furthermore, the flow of heat from the sleeve to the cooling system is not even. Oxides which are formed between the cast-iron sleeve and the aluminium block affect it seriously since they are spread unevenly, which, in consequence, leads to uneven deformation of the bush. Such a situation leads to scavenges during the operating time of the engine and its power losses. In addition, there are problems with assembling cast-iron cylinder sleeves and their sealing resulting from the difference in the linear expansion coefficient of cast iron and aluminium. Research has been conducted on galvanized coatings deposited on cylinder walls, e.g. nickel galvanized coatings with an addition of dispersed SiC. The obtained nickel coatings with an addition of silicon carbide have been utilized merely in small-size engines. However, the process of electroplating is both complicated and relatively expensive. Additional problems related to environmental protection generate more costs, which has brought further research to stop. Thermal spraying processes have turned out to be the most perspective; they have also become a standard solution during the production of aluminium engine blocks.

TABLE 3.4. A comparison of applying thermal spray processes to film coating on cylinder bodies aluminium blocks [7].

Criteria	Thermal spray processes		
	Arc (wire)	HVOF (wire or powder)	Rotating plasma (powder)
Materials	Metallic alloys	Metallic alloys, carbides, composites	Metallic alloys, carbides, ceramics, composites
Versatility in choice of material	Restricted choice of materials	Limitation for refractory materials	High versatility
Heat transfer into the engine block	Medium	Very high	Low
Repeatability of the melting process	Formation of the melted particle is difficult to control	High (powder) Medium (wire)	High
Coating thickness as sprayed	500 µm	200 µm	200 µm
Coating properties for cylinder bores	Medium	High	High
Process cost	Low	Very high	Low
Industrial status	Start of Small basis	Prototypes	In industrial production for 5 years

Arc, plasma and HVOF spraying processes, which were applied in the spraying of prototypical engine blocks, have been analysed (Table 3.4) [6, 7, 163, 165]. Plasma-sprayed coatings proved to be the most convenient both technologically and economically. They met strict requirements concerning quality and mass-production feasibility. The RotaPlasma® system developed by Sulzer Metco company with a rotating plasma-arc gun enables to put coatings on a fixed cylinder block. Depending on the purpose of coatings, various powder materials are applied: carbon steel with an addition of iron carbide (wustite FeO and magnetite Fe_3O_4) as a solid lubricant; tool steel composite with Mo; stainless steel with Mo and Cr; and composites with 20% of ceramic. Moreover, wustite and magnetite are obtained during the plasma spray process. The amount of iron carbide can be controlled by selecting plasma spraying parameters, plasma contents, the dwell time of powder grains and its enthalpy.

Plasma spray coating has a typical lamellar microstructure (Fig. 3.8); its thickness is 120-150 μm, after finishing it ranges it varies from 70 to 170 μm. Furthermore, the coating has to meet strict quality requirements regarding proper microstructure and substrate topography. Porosity of the coating should range between 1 and 3%; taking tribology into consideration, the most advantageous one is that of 2%. The microstructure of spray coatings from carbon steel should have wustite which is ca. 70% harder than the steel matrix. It functions as a solid lubricant lowering both the coefficient of friction and wear. Optimal content of wustite can be achieved by a proper alteration of spraying parameters. Magnetite (Fe_3O_4) with solid lubricant properties is also found in the coating and its presence is considered advantageous. However, the occurring hematite (Fe_2O_3) is hard and its impact on the interaction of the ring and the cylinder body has not been assessed yet. Barbezat [6] claims that it should be avoided for it accelerates wear, whereas Shin [136] suggests that hematite increases resistance to wear.

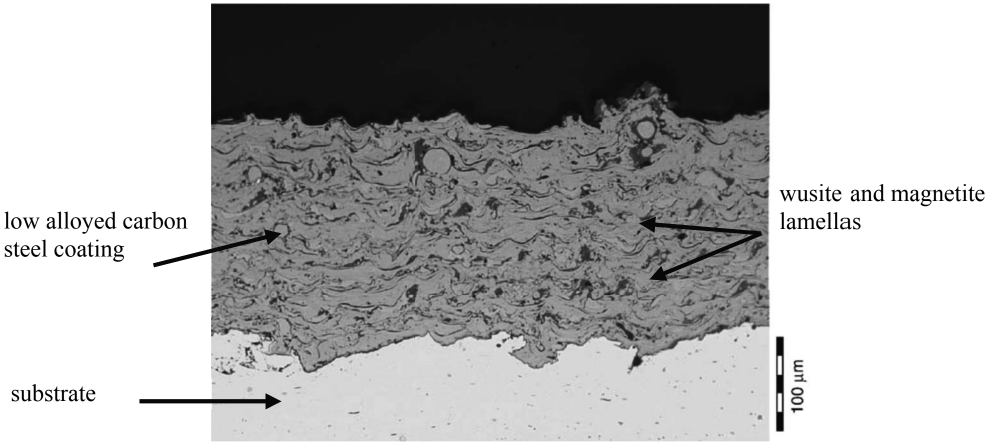

Fig. 3.8. Typical microstructure of low alloyed carbon steel with wustite and magnetite as solid lubricants [6].

The process of honing allows to obtain proper substrate topography, which allows lubricant retention in micropores. Unlike abrading or turning treatment, it does not close pores. Rest products obtained as the result of interaction together with foreign matter are embedded in hollows formed during this process and they do not accelerate wear. Substrate porosity after honing ought to be below 0.2 μm [29] or 0.3 μm [6, 135]. Higher values of porosity result in increased oil consumption, whereas too smooth cylinder body is prone to seizure. Exploitation tests have shown that plasma spray coatings have much better properties than cast-iron cylinder bodies. Coefficient of friction is 30% lower. It is of paramount importance, as 40% mechanical losses in the engine occur between the cylinder and the piston unit. As a result of applying plasma spray coatings on cylinder bodies in aluminium blocks, fuel consumption dropped by 4%. Moreover, oil consumption has also been significantly decreased, which is vital taking environmental protection into consideration. Also, the wear of coatings is lower than in the case of cast-iron cylinders. The value of wear is 5 nm/h in the end limit position of the piston. It has to be highlighted that the achieved results are the outcome of the research on mutual interaction of the whole tribological unit comprising a cylinder, a piston ring as well as lubricating; it also has a crucial impact on its efficiency [6, 41]. Ford has introduced a competitive system with the RotaPlasma® one. The PTWA® (Plasma Transfered Wire Arc) system developed by Ford allows to use a low-carbon steel wire (0.1% C) which is inserted perpendicularly into the plasma beam and in the spray direction. The electric arc is first striking between an infusible cathode and copper anode and then moved onto the sprayed wire (Fig. 3.9).

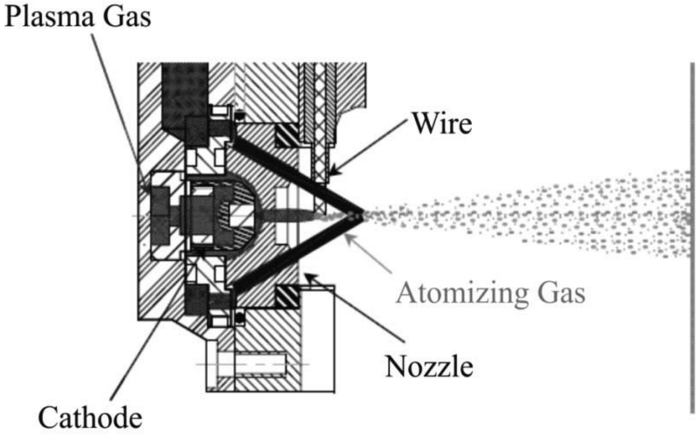

FIG. 3.9. Schematic of the PTWA plasma spray apparatus [46].

Both the composition and microstructure of the coating depend on the composition of plasma gas and curtain gas with an adjustable content of oxygen. It allows to obtain gradient coating containing between 10 and 30% of wustite which hardness is 70% higher than that of the steel matrix. Such microstructure and phase composition of the spray coating provides its high resistance to wear. The coating after spaying is 120-150 μm thick and its porosity does not exceed 2%. After honing its measurement ranges from 70 to 170 μm. This solution (US patent 6,559,407) won the IPO National Inventor of the Year Award in 2009 in the USA and was applied in Mustang GT500 Shelby and Nissan GTR, where the weight of the engine was reduced by 50 kilograms [46, 133, 135].

The properties of coatings on the surface of cylinders in aluminium blocks can also be improved by applying h-BN. For this reason, composite powder was made by sintering cast iron with a 5% addition of h-BN at 1,300°C. As a result of sintering, 1.86% of graphite was educed in cast iron powder. The test conducted with plasma spray coatings from this powder proved perfect properties of such a coating; it had a lower coefficient of friction and increased wear resistance than a sprayed coating from pure cast iron powder [107, 159]. Identical procedure of obtaining composite powder was also applied iron boride powder with a 5% addition of h-BN. Plasma spray coating contained 4.58% of h-BN and it exhibited a significantly lower coefficient of friction and wear in comparison to cast iron cylindrical sleeve [105]. Promising results were achieved for WC-12Co coating with HVOF sprayed onto the surface of the cylinder, which, in comparison with Fe-alloy, FeCrMo, and TiO_2/TiC turned out to have the lowest coefficient of friction [127]. Sub-stoichiometric titanium oxides are also alternative materials for the previously used powders. Plasma spray Ti_nO_{2n-1} (APS) and $TiO_{1.95-x}$ (VPS) coatings as well as grey cast iron used on cylinder sleeves were tested. The piston ring with plasma spray Mo-NiCrBSi coating served as a countersample. In the conditions of mixed and boundary friction, the best results were achieved for Ti_nO_{2n-1} (APS) [140].

3.2. Thermal Sprayed Nanostructured Coatings

Nanostructured materials provide new possibilities, which enable creating composite structures with much better properties than composites obtained from conventional materials. Such a solution facilitates combining selected features of different nanomaterials in order to obtain a composite with the required durability, thermal, insulation, tribological, etc. properties. Finally, we obtain a nanostructured composite material with much better properties than the ones comprising it. In the case of composite containing a solid lubricant, it is comprised of a nanostructured matrix, providing mechanical durability, and evenly distributed nanostructured solid lubricant.

Research concerns materials which have found wide utilization in industry, e.g. Al_2O_3, Cr_2O_3, TiO_2, Y_2O_3, ZrO_2, or hydroxyapatites [20, 47, 50, 61, 63, 81, 83, 87, 89, 98, 155, 185]. In thermal spray processes nanostructured coatings can be obtained by spraying powder of typical granulation (15-53 μm), the grains of which are built out of nanocrystals (Fig. 3.10) or by spraying suspensions, which have them [68, 124]. Nanostructured powder for thermal spray processes are currently produced on an industrial scale [44, 88].

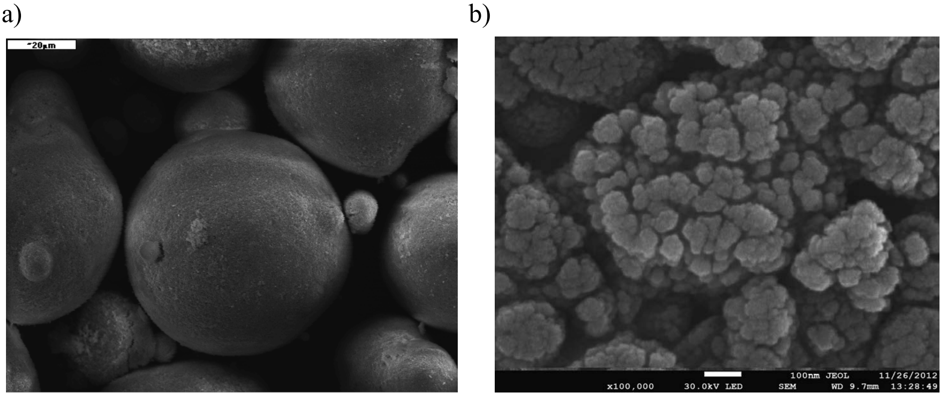
a) b)

Fig. 3.10. Al_2O_3-13TiO_2 nanostructured powder: a) powder grains (1000x); b) nanocrystals on the surface of powder grain (100000x).

Chromium oxide is the material with a high resistance to wear. That is why, in many utilizations, it occurs independently or as a component of the sprayed composite coatings [32, 60]. Comparative study of the plasma spray coating from the powder containing nanograins, 50 nm in size, showed that it has a lower coefficient of friction and increased hardness as well as resistance to wear than sprayed with micrometric grains of chrome oxide coating [81, 90]. The properties of supersonically sprayed coatings from chromium oxide can also be improved with an addition of TiO_2 [165]. HVOF-sprayed coatings made from nanostructured titanium dioxide exhibited over 2.5 times greater adhesion than plasma spray hydroxyapatite coatings. Their hardness was by 61% higher than that of sintered hydroxyapatite. In addition, there are areas on the coating substrate in which partially remelted nanostructured grains of TiO_2 are present. Such areas may additionally increase adhesion of osteoblastic cells due to improved mutual interaction with such proteins as fibronectin. Moreover, in comparison with hydroxyapatite coatings, titanium dioxide does not dissolve in human tissue, it is absolutely stable, and retains its properties throughout its use [86, 93]. Supersonically sprayed nanostructured coatings made from an alloy on the basis of iron had a better erosive resistance than widely-used HVOF-sprayed WC-CoCr coatings [110]. This kind of coatings has also better corrosion resistance in sea water and salt fog, being an alternative for the used galvanised chromium coatings [17]. Utilizing HVOF-sprayed MCrAlY nanostructured coating as a layer bonding a coating which acts as heat insulation caused a 50% increase in its durability in comparison with conventional interlayer [69]. Plasma spray nanostructured Fe-Si coatings possessed magnetic properties [23]. Also, applying the process of cold-gas spraying, nanostructured coatings with better properties can be obtained [167, 184].

In plasma sprayed nanostructured composite abrasive coatings, there can be differences in homogeneity of their microstructure. It is caused by diverse physical properties of the materials, which are simultaneously sprayed, i.e. CoNiCrAlY alloy, polyester, and h-BN as a solid lubricant. The conducted comparative tests with a nanostructured ZrO_2-7wt% Y_2O_3 coating showed that they can be an alternative solution to previously used conventional composite coatings, simultaneously eliminating problems with inhomogeneity of their microstructure [85].

Spraying suspensions is an alternative to coatings sprayed with powders containing nanostructured grains. Very fine powders, below 10 μm, are difficult to transport. The problem is in their susceptibility to dampness and to electrostatic forces, which leads to their agglomeration. Particularly, it concerns light ceramic powders, such as metal oxides. They are also problematic to insert into gas stream, which results in their presence mainly in an external and cooler area, where their heating is less intense. It is much more convenient to transport and insert fine powders in the form of suspension into the gas stream. The problem of agglomerating them is solved by its constant stirring and adding superficially active materials. Such a suspicion easily penetrates the gas stream in which, under the influence of aerodynamic forces, it decomposes into fine drops. The dissolvent evaporates being affected by a high temperature of the gas stream, and very fine powder grains are deposited on the substrate. Suspensions can be sprayed by either plasma or supersonic spraying (Fig. 3.11) [14, 40, 113, 114].

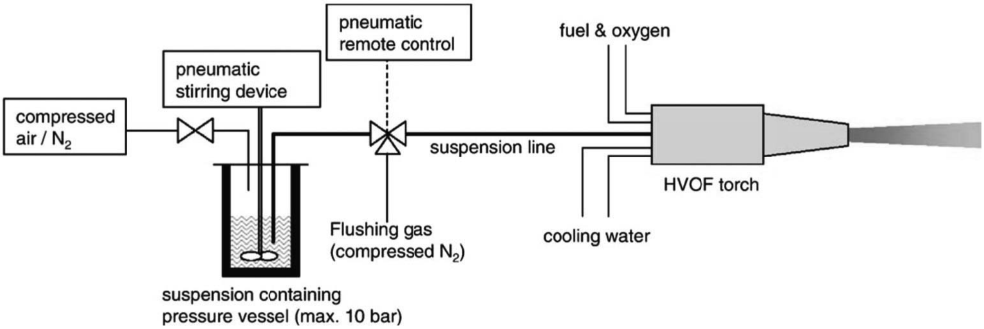

FIG. 3.11. Schematic diagram of High Velocity Suspension Flame Spraying (HVSFS) [14].

Retaining the nanocrystals, which are in the suspension, in the sprayed coating is the elementary problem. Nanograins can be subject to sintering when they melt during their dwelling time in the spray stream. This results in having substantially larger grains, micrometric in size at the moment of impacting the substrate and solidifying on it. Considerable deformation of the liquid particle impacting the substrate as well as its further decomposition into smaller ones are also possible. Each of them solidifies and the size of the solidified crystal is very often smaller than 100 nm, particularly when the substrate is intensely cooled (Fig. 3.12).

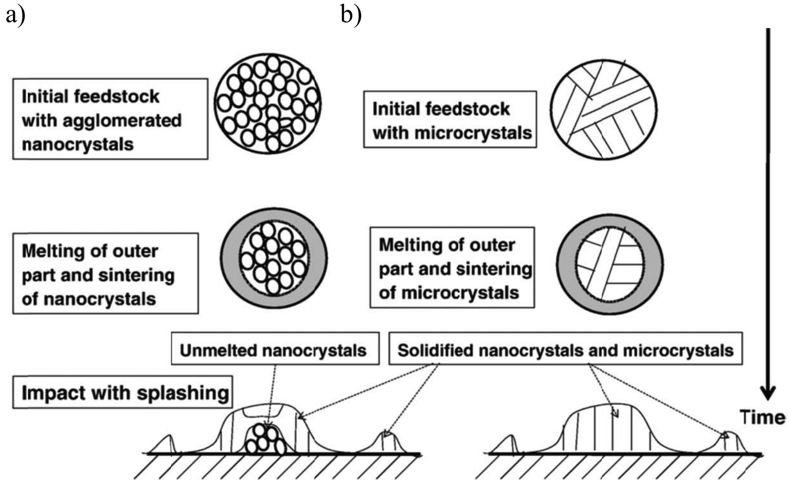

Fig. 3.12. Evolution of crystals size at thermal spraying of different feedstocks: nanostructured (a) and conventional (b) [4].

Research on the coefficient of friction of plasma spray Al_2O_3, Al_2O_3-ZrO_2 suspension coatings proved their excellent tribological properties. The coefficient decreased fourfold after decreasing the size of grains from 36 μm to 0.3 μm. It was also concluded that the composition of plasma-generating gas affects coating microstructure and the coefficient of friction [31]. This technique of spraying facilitates obtaining composite coatings. Plasma spray ZrO_2-$13Y_2O_3$ suspension coating, with grain size $d_{50} = 400$ nm and 16% addition of SiC grains, $d_{50} = 3$ μm in size, caused an increase in wear resistance, compared to a coating without SiC, by several times. Nevertheless, the presence of hard SiC grains led to increase in the coefficient of friction [30]. In the sprayed coatings made from suspensions containing TiO_2 grains, 20-30 nm in size, the influence of cooling the coating on its phase structure could be observed. In air-cooled coatings, both phases, rutile, and anatase were evenly distributed in the coating, whereas in the water-cooled coating, soft anatase was on the surface, while hard rutile was underneath. It significantly affected their tribological properties. In the scratching resistance test, soft anatase exhibited lower level of wear and a higher coefficient of friction than hard rutile [128]. Supersonically sprayed Al_2O_3 suspension coatings had a fivefold higher electric resistance than the coatings sprayed with a conventional powder [157].

Nanostructured powders also facilitate obtaining composite coatings. An improvement in properties of PS304 coatings, utilized on turbine bearings, was possible as a result of using one of the components in a nanostructured form. Investigating PS304 powder, which is a mixture of NiCr, Cr_2O_3, Ag, and BaF_2-CaF_2 powders, showed that component grains are substantially different in terms of size and morphology. It influences various behaviour of grains in the plasma stream and does not allow obtaining a coating with evenly distributed components, which lowers its properties. For this reason, composite powder was made; its grains contained all the components, and chromium oxide was in a nanocrystal form. Plasma spray composite coating made from this sort of powder had a more homogeneous mimcrostructure, increased hardness and adhesion. Solid lubricant more evenly distributed in the coating contributed to its lower coefficient of friction and wear [25, 26, 179]. Substantially better properties of the sprayed nanostructured WC-Co, TiO_2, and ZrO_2-Y_2O_3 coatings were confirmed by Marple and Lime. Yet, it requires a thorough selection of granulometric composition of powders and a careful selection of parameters in order to limit coarseness of nanostructured grains [97].

Tungsten carbide is the material used for numerous investigations. Taking its high level of hardness into consideration, it is most often used in the form of sinter with cobalt, which guarantees its high durability. Its outstanding wear resistance contributed to the use of WC-Co to increase durability of various machine parts. The structure of the sprayed coatings is composed of hard WC grains deposited in a cobalt matrix [186, 188, 194]. Supersonic spraying is currently used for their application. As a consequence of reaction of high temperature plasma and the presence of oxygen, the previously-used processes of plasma spraying led to its decomposition, decarburization and oxidation according to the following reactions:

$$2WC \rightarrow W_2C + C,$$

$$W_2C \rightarrow 2W + C,$$

$$2C + O_2 \rightarrow 2CO.$$

In consequence, significant changes in the phase composition considerably worsened exploitation properties of the coatings [48, 121, 201, 204]. The process of supersonic spraying, at a relatively low temperature of the spray stream and a short dwelling time of the powder grain in the spray stream, limited those unfavourable phenomena to a large extent. The next stage facilitating even better results is the possibility to take advantage of the nanostructured tungsten carbide powders, whose grains with granulation ranging from 15 to 45 μm are agglomerates of grains of nanostructured size.

The most common methods of obtaining WC-Co grains are as follows: spray conversion, mechanical alloying, chemical co-precipitation, and high-energy ball milling. In the case of sintering the grains, the issue of controlling the process occurs, because, as a result of high activity of nanograins, they undergo sudden growth. High-energy ball milling of nanograins from W(Co,C) composite powders allows limiting this process. Obtaining the WC phase during sintering, causes the consumption of the energy cumulated in composite W(Co,C) nanograins and limits the growth of WC-Co nanograins. The distribution of phases in the grain of W(Co,C) composite powder after milling in a high-energy ball mill is illustrated in Figure 3.13.

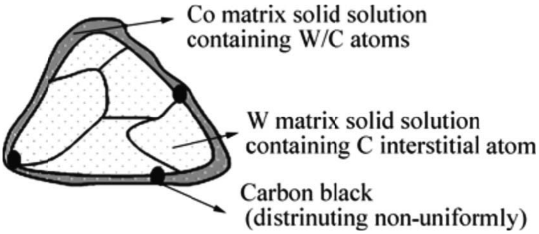

FIG. 3.13. Schematic illustration of distribution of W, Co and C phases in as-milled powders [19].

Solid solution of tungsten possesses dispersed carbon atoms, whereas a solid solution of cobalt has the atoms of tungsten and coal. Sintering at a temperature of 700°C for ca. 30 minutes leads to forming the following phases: WC, W_2C, W, and Co_3W_3C. The conclusion to be drawn from these facts is that, W and C present in the grains of nanopowder reacted forming new WC and W_2C phases, whilst cobalt reacted with tungsten and carbon forming Co_3W_3C (η-carbide).

$$W + C \rightarrow WC$$

$$2W + C \rightarrow W_2C$$

$$3W + 3Co + C \rightarrow Co_3W_3C$$

Co_3W_3C (η-carbides) occur mainly during sintering at 800°C as a result of coercive force. Furthermore, Co_6W_6C carbide is formed at this temperature and the following reactions take place [19]:

$$2W + C \rightarrow W_2C$$

$$2Co_3W_3C + W \rightarrow Co_6W_6C + WC$$

$$Co_3W_3C + 2C \rightarrow 3WC + 3Co.$$

During supersonic spraying, WC nanocrystals are more susceptible to the spray stream owing to smaller sizes and a larger ratio of capacity to area [5, 8, 21, 24, 137, 203]. Unfavourable reaction of the surrounding upon the nanocrystals of tungsten carbide during spraying can be avoided by applying cold-gas spraying. As it is the process in which the stream of gases has a low temperature, the coating material is in a solid state and no phase changes occur. The coating is formed as a result of very high kinetic energy of powder grains, not because of their high-plastic state or melted while impacting the substrate, which takes place in other processes of thermal spraying. During the process of cold-gas spraying, there is almost an absolute consolidation of the coating, after which their porosity is hardly noticeable (Fig. 3.14) [3, 72, 73, 82, 84, 197, 202].

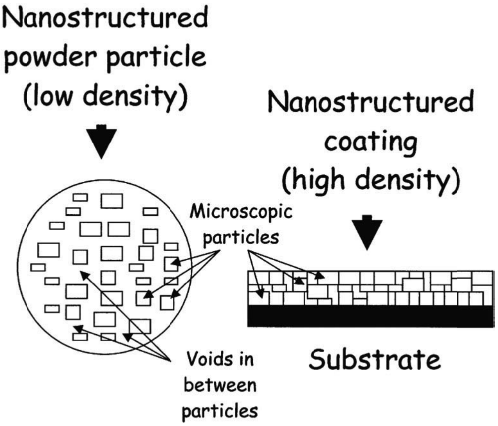

FIG. 3.14. Schematic of the particle densification upon impact at a high velocity [84].

3.3. HVOF Spraying as an Alternative to Galvanic Chromium Plating

Research on the further increase of the properties of supersonically sprayed WC-Co is associated with searching new technologies which enable elimination of galvanic chromium plating. In industry, galvanic chrome plating have found wide application in covering new elements and the regeneration of machine parts owing to the following merits of these coatings: high hardness level of the chrome layer (higher than in the case of the hardest sorts of hardened steel), high abrasion resistance, chemical and high temperature resistance, aesthetic appearance and relatively low deposition costs. However, the solutions used in the process, which contain hexavalent chromium and which allow obtainingcoatings of the best properties, pose a very big threat to people and environment. Hexavalent chromium is carcinogenic and it also causes allergies, irritation of skin and the respiratory tract. The fog which forms during this process and the possibility of skin contact with the solution have a direct influence on people. Moreover, the technological process of galvanic chromium plating is the source of many harmful waste materials, such as used up solutions, solutions removedalong with chromium plated parts, big amounts of rinse water and polluted masking materials. The utilization of these materials is troublesome and costly. The above mentioned problems associated with the use of galvanic chromium plating and the introduction of new rules concerning environment protection made it necessary to search for new technologies enabling replacement of chromium plating. The importance of the harmfulness of hexavalent chromium has been reflected in the new standards concerning its admissible emission within 8 hours introduced by OSHA (Occupational Safety and Health Administration USA).It refers to the increasingly higher requirements regarding processes which pose an extremely big threat to the environment. The current PEL (Permissible Exposure Level) index, i.e. 5 $\mu g/m^3$, is 10% of the previous PEL value, i.e. 52 $\mu g/m^3$. Apart from that, the plants where exposure exceeds 2.5 μg/m^3 are obliged to monitor it constantly and are strongly advised not to go beyond 1 μg/m^3. The progress in terms of supersonic spraying allows obtaining coatings with better properties, without hazardous effect on the surrounding. The initially-applied plasma spraying [79, 95] enabled substituting chromium plating in many cases. However, it was the introduction of supersonic spraying and its variations (HVOF, HVOLF, HP-HVOF, HVAF) that expanded the possibilities of using this method. It allows obtaining coatings from numerous materials, which replace galvanic chromium plating and are significantly more resistant to wear and corrosion, which is crucial to human health and environment protection [11, 18, 42, 115, 131].

Chapter 4

State of the Art Analysis

On the basis of the analysis of literature, the following conclusions can be drawn: although solid lubricants have been used for many years, the subject matter regarding their obtaining and application is still researched. In particular, the newest PVD and CVD methods, together with their variations, facilitate obtaining DLC (diamond-like carbon) or GLC (graphite-like carbon coatings) with outstanding tribological properties. Research involves also thermal spray processes, especially supersonic and plasma spraying; in these processes composite coating with a lower coefficient of friction is possible to obtain through the use of solid lubricants. The range of the analysed coatings involves materials with high wear resistance (Al_2O_3, Cr_2O_3, MCrAlY, NiCr, NiMoAl, WC-Co, and Cr_2C_3-NiCr) and the materials with the properties of a solid lubricant (graphite, MoS_2, WS_2, BaF_2, CaF_2, Cu, Ag, and PTFE). Such a wide range of the used materials in combination with the advantages of the applied techniques of thermal spraying facilitates a number of industrial utilizations. Thermally-sprayed coatings on the basis of iron, used for cylinders in aluminium blocks belong the most technologically-advanced ones. As part of the Oil-Free Turbomachinery research program, NiMoAl-Cr_2O_3-Ag-BaF_2-CaF_2 coatings for shaft pivots in bearings of air turbines were developed; they are a unique solution enabling their operation at 650^{o}C. Current jet efficiency is possible due to spraying abrasive casings on compressors and turbines. The research carried up till now concerns nanostructured composite coatings with a decreased coefficient of friction only to a limited extent. In particular, there is a lack of systematic comparative research of the supersonically sprayed coatings which allow for selecting coating materials for: the matrix and solid lubricant. Additionally, there is a shortage of indications concerned method of preparing the substrate prior to spraying and also the processes of coating finishing. The properties of the sprayed nanonstructural solid lubricants, Fe_3O_4 ferro-ferric oxide in particular (which, regarding the previous research, has an important influence on the properties of the coatings), are extremely interesting. However, determining its tribological properties remains to be seen, especially in supersonically sprayed coatings which operate in friction conditions without external lubrication. Also, the properties of the sprayed nanostructured composite coatings are yet to be researched.

Chapter 5

Theses and Aims of the Research

The research on HVOF spray nanostructured composite coatings with a reduced coefficient of friction has been insufficient because such coatings have not yet been produced on a large scale; the literature on spray coatings containing solid lubricants is also scarce. The data obtained so far indicate that adding nanostructured iron oxide (Fe_3O_4) to a nanostructured WC-Co matrix should contribute to a reduction in the coefficient of friction and the wear of surfaces in contact. The results of the theoretical and experimental studies were used to formulate the following theses.

1. **The properties of nanostructured iron oxide, Fe_3O_4 (magnetite), indicate that, by adding it to a nanostructured WC-Co matrix, we can alter the tribological properties of that matrix and form a nanostructured coating with functional properties superior to those of a conventional coating.**
2. **The proportions and distribution of the composite constituents need to be precisely specified as these factors are responsible for the tribological properties of a coating (lower friction resistance and lower wear).**

The aims of the fundamental research formulated on the basis of the above theses include:

1. Identifying the properties of the nanostructured coating materials.
2. Determining the effect of the low temperature/high velocity gas stream on the grains of the powders differing in physical and chemical properties.
3. Analyzing the process of formation of an HVOF spray coating and establishing its influence on the coating properties.
4. Determining the influence of the composition of the coating material and the HVOF spraying parameters on the tribological properties of the composite coatings.
5. Analyzing the process of lubrication by applying a ball-on-disc tribotester for the HVOF spray conventional and nanostructured coatings containing a solid lubricant (Fe_3O_4).
6. Developing a model of interaction of the outer layer of the composite coating with the counter surface under dry friction conditions.

The purposes of the applied research include:

1. Forming an HVOF spray nanostructured WC-Co/Fe_3O_4 coating with optimal tribological properties to operate under dry friction conditions, using the results of the optimization experiment.
2. Developing a method of spray deposition of nanostructured composite coatings on elements of friction pairs in a sliding contact operating under dry friction conditions.

Chapter 6

Test Procedure, Methods and Equipment

6.1. Test procedure

On the base of insightful analysis of available data the following research procedure has been applied:

1. Material for the composite matrix should be selected in order to provide high possible resistance to wear and to guarantee good maintenance properties of the composite with lowered friction coefficient.
2. Material for a solid lubricant which enables lowering the coefficient of friction and reducing wear of the composite coating should be selected.
3. Research should be conducted on the basic properties of the coating material used for the matrix; its granulometric composition, grain morphology, and phase composition.
4. Research should be carried out on the basic properties of the coating material used for the solid lubricant; its granulometric composition, grain morphology, and phase composition.
5. Test on microstructure, chemical composition, and phase composition of the sprayed coatings should be conducted.
6. A program should be drawn up and Taguchi optimization experiment of both nanostructural and conventional properties of composite coatings should be executed.
7. Verifying research should be undertaken on the basis of the results obtained from the optimization experiment.

6.2. Test Methods and Equipment

6.2.1. Analysis of the Granulometric Composition of the Thermal Spray Powders

Laser size measurement is the most effective method of analyzing granulometric decomposition of powder. It enables measuring grains ranging from 10 nm for wet-dispersed samples in suspension and from 100 nm dry-dispersed powder in the airstream. A single measurement lasts from 5 to 10 seconds, whereas the whole measurement cycle lasts approximately 2 or 3 minutes. The measurement is carried out through laser diffraction. The tested sample is illuminated with a laser beam which, going through opaque grains of powder that operate as diffraction grating, undergoes partial deflection behind the tested sample where Fournier lens forms the diffused light into rings. The obtained unit is measured by detectors fixed on a plate made from photosensitive silicon. Grains of smaller diameter cause larger diffraction of laser beams and thus form diffraction rings which are widely set. Larger grains, in turn, form rings which are closely set. Diffraction formulas dependent on the size of grains are shown in Figure 6.1.

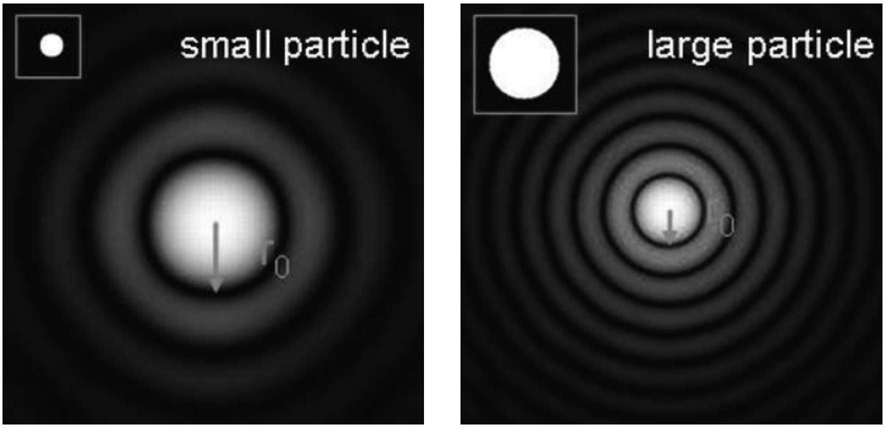

FIG. 6.1. Diffraction rings dependent on the size of grains. [http://www.sympatec.com/EN/LaserDiffraction/LaserDiffraction.html]

The range of grain size of powders used for thermal spraying is given according to American norm – ASTM B214. Labelling the range of grain size of powder with A-B μm indicates that powder should not have more than 2% of grains larger than B and not more than 5% of grains smaller than A. The test on granulometric composition was conducted with HELOS laser diffraction sensor constructed by SympatecGmbh. The measurement range of the sensor enables determining the size of the grains in 31 ranges from 0.9 to 175 μm, which are presented as cumulative distribution and relative density distribution of q_{3lg}grains calculated according to the following formula (6.1):

$$q_{3lg} = 2.3 \cdot 100 \cdot q_3 \cdot x_{lg} \tag{6.1}$$

where: $x_{lg} = (x_o + x_u)/2$ – the average range of measurement referred to logarithmic scale, x_o – the lower measuring range, x_u – the upper measuring range.

6.2.2. Analysis of the Morphology and Chemical and Phase Composition of the Thermal Spray Powders and Coatings

Metallographic microsections and microsctructures of coatings have been tested in the Department of Metal Science and Materials Technologies at Kielce University of Technology. Elements for metallographic research were cut out from the samples with “ISOMET – low speed saw” (BUEHLER) equipped with a diamond saw.

Coating microsections were made using “LaboPol – 5” (STRUERS) polishing machine. The research of the spray coatings was conducted with JSM Jeol 7100F and Jeol JSM 5400 scanning microscopes. This microscope is equipped with an ISIS 300 Oxford (EDS) microprobe, which enables analysing chemical composition of the coating. SEM FEI COMPANY Nova™NanoSEM 200 scanning microscope as well as TEM Philips CM20 with EDAX EDX transmission microscope were used to research powder and coating microstructures. The research of phase composition was conducted with D500 and D8 Advance diffractometers developed by Bruker company, and also with filtered radiation of the Cu and Co lamps. Measurements were done for every sample in one selected area of the coating substrate without initial preparation.

6.2.3. Coefficient of Friction Test

Tests of the coefficient of friction were conducted with the ball on disc T-01 tribological tester produced Institute for Sustainable Technologies National Research Institute in Radom. Figure 6.2 illustrates functioning of the tester. In a tester of this kind, a friction pairs composes of a ring-shaped sample (Fig. 6.3) and a countersample which can be either a pin or ball. A ball with the diameter of ¼’’ made from 100Cr6 steel was applied in the research. During the test, the ball is pressed onto the frontal substrate of the plasma spray ring. The force influencing the ball is determined by the use of weights. Rotational speed of the ring and the weight of the ball are set before the test commenced. The tester enables continous measurement of the friction force at a set load by computer. The test was carried out for rings supersonic plasma spray coatings abraded and grinded for one hour. The following parameters were selected: linear velocity – 0.5 m/s, ball weight – 4.9 N, test time – 1 h. The test was repeated three times for each of the coatings.

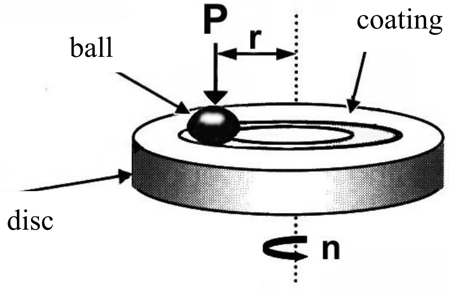

FIG. 6.2. Diagram illustrating the operation of ”ball on disc” T-01 tribological tester.

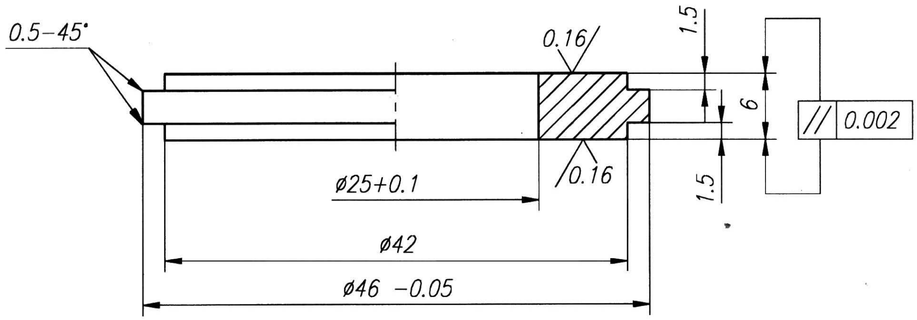

FIG. 6.3. The ring (a sample in T-01 tester).

6.2.4. Wear, Microhardness and Porosity Tests

Samples and countersamples were weighed on the Denver Instrument Company scale to an accuracy of 0.0001 g.

Testing of microhardness for the optimization experiment was conducted with the MMT-X3 Ahardometer (developed by Matuzawa Co., Ltd.) with an automatic microhardness reading. The result of the test was determined by an average of 10 measurements.

The measurements of substrate porosity were carried out with Talysurf 4 device and the SUFORM programme in the Laboratory of Computer Measurement of Geometrical Quantities at the Department of Mechanical Technology and Metrology at Kielce University of Technology (Fig. 6.4). The result of the test was determined by an average of 5 measurements.

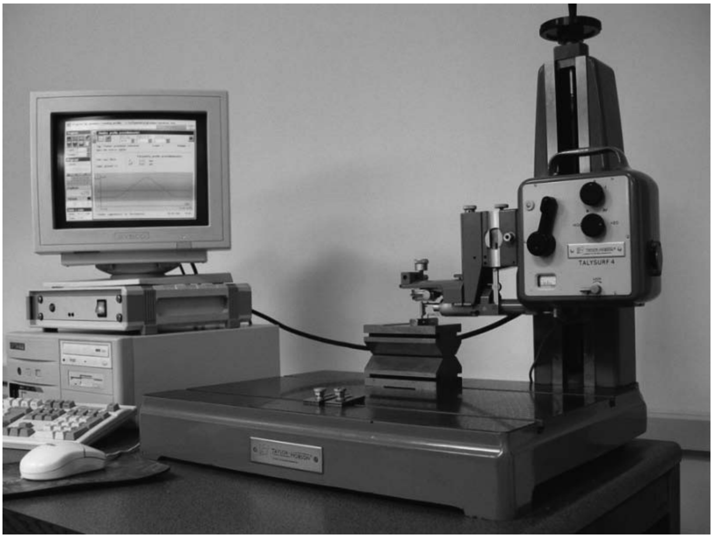

FIG. 6.4. Testing stand: Talysurf 4 with program SUFORM.

6.2.5. Seizure Resistance Test

The research on seizure resistance for supersonic sprayed coatings was conducted in dry friction conditions with FalexT-09 tribological tester, developed by Institute for Sustainable Technologies National Research Institute in Radom. Figure 6.5 illustrates the diagram of the tester performance. In the Falex tester the friction pair is composed of a countersample in the form of a roll made from steel 45 (Fig. 6.6a), fixed to a transmission shaft with a copper pin clamped by two samples in the form of prismatic blocks (Fig. 6.6b) placed in the lever arm of the head. During the research, the turning ratchet causes gradual increase in the tension of springs which load lever arms of the head. Prismatic blocks, which are in the head, clamp themselves with a gradually increasing force in a countersample rotating at a constant velocity, i.e. 290 rpm. The resistance to seizure (i.e. the value of the force at which the copper peg is cut) or, in the case of lack of seizure, the highest possible value of sample load is the result of the research. The course of the research is supervised by the computer which registers the course of the load and friction force in time function. The tests were carried out in the friction condition without external lubrication. The result was the average value of three tests.

For carried out experiment coatings were sprayed onto the vee blocks which were fixed in special holder (Fig. 6.7) enabled simultaneously spraying six samples in the same conditions.

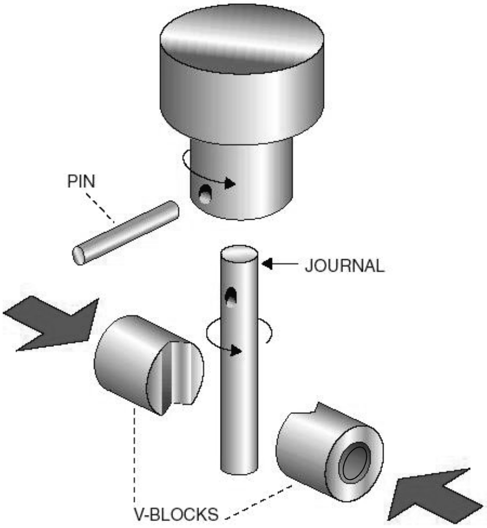

FIG. 6.5. The flow diagram of FalexT-09 tribological tester.

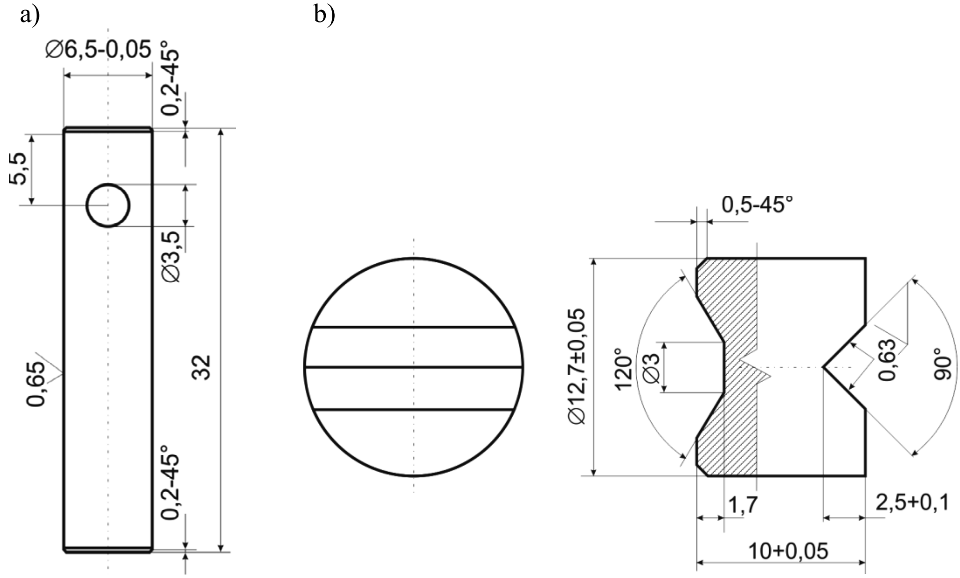

Fig. 6.6. Test elements in T-09 tribological tester: a) pin, b) vee block.

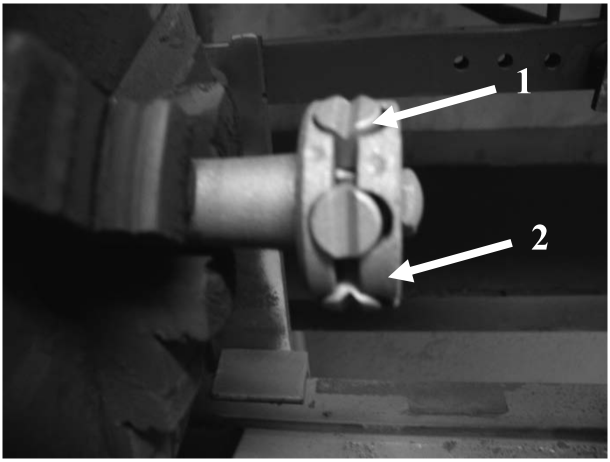

Fig. 6.7. Clamping device holding samples for T-09 tester during supersonic spraying: 1 – vee blocks, 2 – device.

6.2.6. Coating Adhesion Test

Testing of coating adhesion was conducted according to the Polish Norm PN-EN 582 (“Thermal Spraying – Determination of Tensile Adhesive Strength”). Three B-type samples, made from PA6 alloy, were prepared for each sprayed material (Fig. 6.8). Frontal surfaces of the samples were vapour-blasted with APR

600 device (compressed air pressure – 0.5 MPa). Electocorund EB16 was used as abrasive material (grain size 0.6-1.6 mm). The porosity of frontal surfaces of the samples after treatment reached R_a = 7,1 µm.

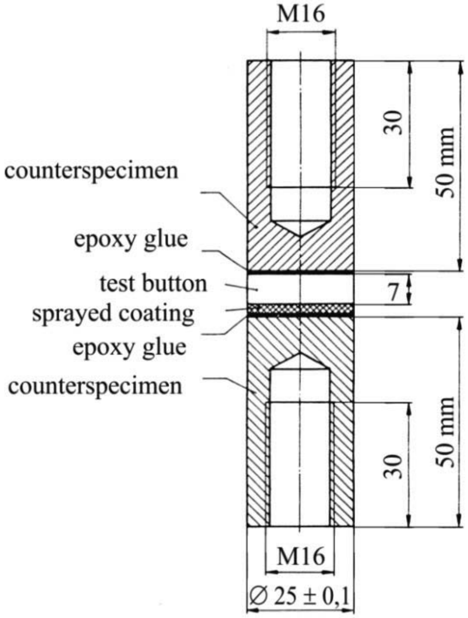

Fig. 6.8. Samples for porosity testing (B).

Next, the samples were fixed on the girth of a special handle (270 mm in diameter) which enables spraying all the samples in identical conditions (Fig. 6.9). Rotational speed of the handle was 40 rpm, whereas sweep speed of the gun was 3.5 mm/revolution.

Fig. 6.9. Handle for sample spraying in porosity testing.

Coating thickness was measured using Minitest 2100 magnetic inductive coating thickness gauge Minitest 2100 developed by ElektroPhysik. The thickness of the coating was measured three times. After spraying, the coatings were not subject to finishing treatment. Samples with the coating were glued with countersample (by PN-EN 582) without coating, which frontal surface was subjected to grit blasting process. Coated samples were glued to the countersample after 24 hours (according to PN-EN 582) and placed on a special stand guaranteeing their vertical position and concentricity during bonding of the adhesive. Adhesion tests were carried out at the Centre for Laser Technologies of Metals with Instron 8501 universal testing machines. The samples, after adhesive bonding, were screwed into handles with ball joints, and then fixed in self-locking hydraulic grips. The sweep speed was 0.05 mm/s. Adhesion (R_H) was calculated as the average value of breaking three samples.

6.2.7. Optimization of the Properties of the HVOF Spray Coatings by Using the Taguchi Method

The process of supersonic spraying is a typical technological process in which the final effect is determined by the quantity value which is a basic criterion in coating assessment. Properties of the obtained coatings illustrate the output system and they depend on the input data as well as interfering factors. Model spray analysis process shows that output parameter (optimization parameters) cannot be explicitly determined with input parameters due to the influence of interfering factors; that is why spraying is a stochastic process.

Researching such processes requires applying statistical methods of planning the experiment. Their aim is to utilize optimally and control all the independent input factors. Multifactor experiments are used in order to achieve this goal. They permit to obtain such input parameters which, in turn, will permit to obtain an extreme value of the tested property of the coating (e.g. wear resistance, adhesion, and porosity). In thermal spray processes it is assumed that optimized property of the coating (the output parameter) is related to input factors of the spray process in the form of a mathematical relationship. For this reason, an experiment should be planned in such a way that a mathematical model of the spraying process with the lowest possible number of input factors could be found. In the Taguchi method the existence of an ideal level (not necessarily real) of the input factor, i.e. the existence of optimal function of optimization, is assumed. It is also considered that increasing deviations of the process from its optimal values causes squared, although not proportional, quality losses. The method includes a few procedures permitting to choose such parameters of the process with which the required quality of the product is obtained and, at the same time, the process itself is as barely sensitive to interfering factors as possible. Such a procedure is aimed at determining the influence of particular input factors and the so-called loss function (depicted as the SN coefficient) illustrating the changeability (the scatter of values) of the tested output factor resulting from the interferences (deviations) of the process. Obtaining such data enables optimization in order to minimize deviation squares or variances of the ultimate factor value from the optimal one. Selecting input factors, determining adequate area, and determining methods and numbers of measures is conducted in the same manner as in the case of other factorial experiments; however, input factors do not need to be measurable. Experiments can be conducted according to Taguchi plans, but it is also possible to apply two- and three-factorial plans, Latin squares, or other plans of this kind [51,74].

The SN coefficient is calculated for the following cases [150]:

a) for the features with a nominal value (e.g. diameter deviation)

$$SN_{Ni} = 10\log\left(y_i^2/s^2\right)$$

where: y_i – the tested output factor, s^2 – sum of standard deviations in the conducted experiment;

b) for the “the larger, the better” features (e.g. coating adhesion)

$$SN_{Bi} = -10\log\left[(1/n)\sum\left(1/y_{ij}^2\right)\right]$$

where: y_{ij} – the tested output factor;

c) for the “the smaller, the better” features (e.g. the coefficient of friction)

$$SN_{Si} = -10\log\left[(1/n)\sum\left(1/y_{ij}^2\right)\right]$$

where: y_{ij} – the tested output factor.

Taguchi method has found numerous applications in industry, where it is widely used [9, 150, 151, 152]. It is also applied to optimize the properties of coatings in surface engineering [42, 132].

On the basis of literature and own research, the following factors have been considered as important in the three-level experiment [59, 102, 173]:

- content of Fe_3O_4 in the blend, η [% weight]
- ratio of oxygen to propane, λ
- spraying distance, d
- intensity of air flow, Q [l/min].

On the basis of Taguchi tables (P = 4, the number of input parameters, L = 3, the number of level of parameter changes) (Table 6.1), a system of parameter changes for supersonic spraying was designed (Table 6.2) and an optimizing experiment was conducted (according to Table 6.3) in order to determine the influence of the assumed factors on:

- coefficient of friction,
- coating microporosity,
- sample wear,
- countersample wear,
- coating porosity,
- porosity adhesion.

TABLE 6.1. Orthogonal Taguchi table, $P = 4$, $L = 3$.

Experiment	*A*	*B*	*C*	*D*
1	1	1	1	1
2	1	2	2	2
3	1	3	3	3
4	2	1	2	3
5	2	2	3	1
6	2	3	1	2
7	3	1	3	2
8	3	2	1	3
9	3	3	2	1

TABLE 6.2. Range of supersonic spray parameter changes.

Level	Parameter			
	A (η % wag. Fe_3O_4)	*B* (λ, O_2/C_3H_8)	*C* (*d*, mm)	*D* (*Q*, l/min)
1	5	4.4	180	336
2	10	4.7	200	375
3	15	5.0	230	414

TABLE 6.3. Plan of the optimization experiment.

Experiment	η, % wag. Fe_3O_4	λ, O_2/C_3H_8	*d*, mm	*Q*, l/min
1	5	4.4	180	336
2	5	4.7	200	375
3	5	5.0	230	414
4	10	4.4	200	414
5	10	4.7	230	336
6	10	5.0	180	375
7	15	4.4	230	375
8	15	4.7	180	414
9	15	5.0	200	336

6.2.8. HVOF Equipment

Supersonic spraying High Velocity Oxy-Fuel (HVOF) belongs to the group of flame spraying processes in which continuous stream of gases which exits the nozzle of the gun have the hypersonic velocity. Such high velocity allows to obtain by grains of powder significantly higher velocities than in the case of the others thermal spray processes. High velocity of the grains cause forming coatings with much better properties and adhesion to the substrate. These advantages generated intensive development of systems for supersonic spraying fed not only by gases but by kerosene or alcohol too (HP-HVOF, HVAF) [112]. Coatings with comparable properties can be obtain by detonation or cold spraying systems [52].

Supersonic spray coatings were deposited with the use of Hybrid Diamond Jet supersonic spray system developed by SulzerMetco company. It is a fuel-oxygen spraying device with supersonic stream speed and axial injection of the coating material (Fig. 6.11). The above-mentioned system is composed of the following sub-assemblies: Diamond Jet gun, gas flow meter units, gas reduction units, pneumatic feeding and regulatory unit, cooling system with a blockade (Fig. 6.10).

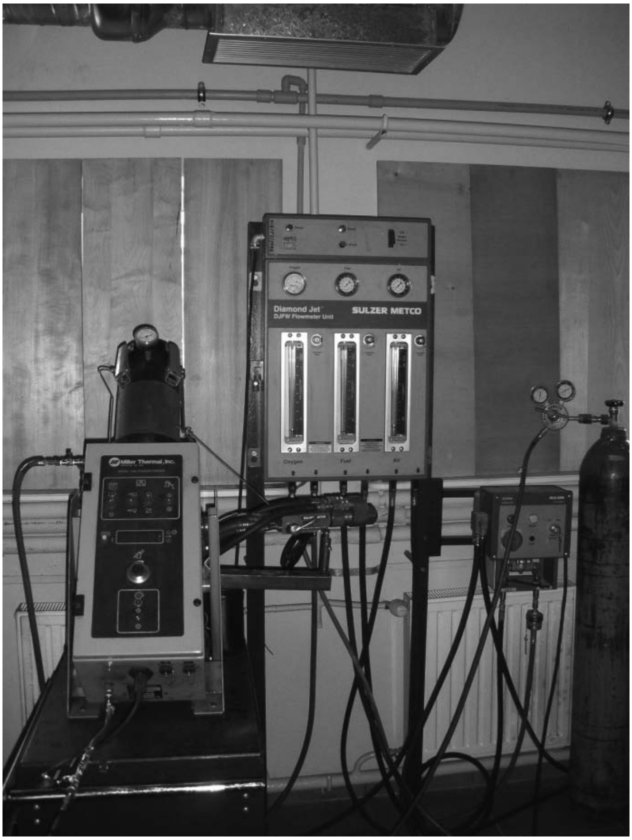

FIG. 6.10. Hybrid Diamond Jet system for supersonic spraying.

Hybrid Diamond Jet gun is the main element of the supersonic spray system. Regulated flow of oxygen stream with combustible gas and compressed air causes acceleration of the melted material in gas stream. During gun operation, a mixture of oxygen and flammable gas is used; the gas can be propylene, propane, or hydrogen depending on requirements resulting from the type of deposited coating. The gun operating in the Department of Operation Engineering is equipped with a nozzle unit to operate with propane which flows through the siphon unit, where it is precisely mixed with oxygen (Fig. 6.11). Next, the gas mixture flows through the nozzle and is ignited outside the gun. Ignited gases form a flame with a circular configuration. Combustion temperature reaches 2970 K.

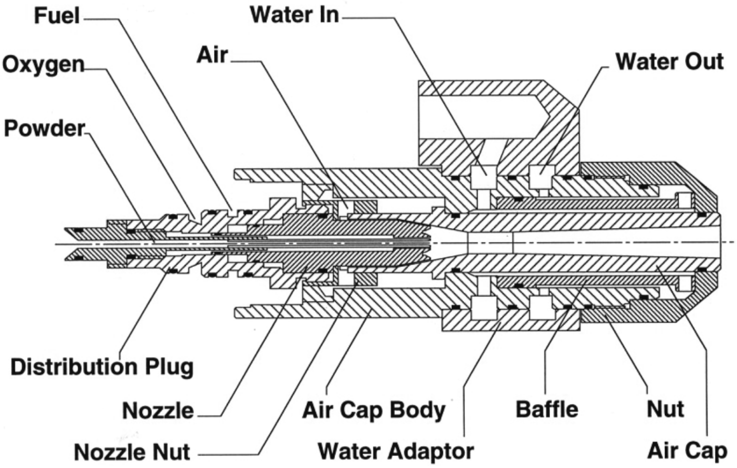

FIG. 6.11. Diagram illustrating Hybrid Diamond Jet Gun for supersonic spraying.

TABLE 6.4. Parameters of supersonic spraying.

Parameter	Value
Oxygen pressure, MPa	1.03
Oxygen volume flow, Nl/min	253
Propane pressure, MPa	0.69
Propane volume flow, Nl/min	77
Air pressure, MPa	0.72
Air volume flow, Nl/min	375
Spraying distance, mm	200

Spraying parameters included in the Hybrid Diamond Jet System Manual formed the basis for Taguchi plan (Table 6.4). Before spraying, the samples had been degreased and grit blasting with electrocorund EB14 at air pressure of 0.5 MPa.

6.2.9. Preparation of the Powder Mixture

The main problem regarding the use of coating materials in the form of mixtures is their transport capability within the spray stream used in the powder feeder. Such factors as density, size, and shape of powder grains forming the mixture affect transport capability of the spray stream. If small powder grains are taken into consideration, then they have a growing tendency of adhering one to the other. It is a result of the increasing ratio of size to weight; therefore, friction and cohesion forces dominate gravity forces. An increased influence of these forces lowers their transport capability with gas owing to the fact that they easily solidify. In the case of spraying a mixture composed of powders with different density, size, and grain shape, segregation of components may occur during their transport from the feeder to spraying gun, which leads to coating in homogeneity or to blocking the cord feeding the coating material to the gun.

The following mixtures with given powder proportions were prepared for both supersonic and plasma spraying (Table 6.5):

- WC-12CoAmperit™ 519.074 + Fe_3O_4Inflox™26FE23,
- WC-12CoNanox™S7412 + Fe_3O_4 Nanox™26FE23.

TABLE 6.5. Components of mixtures for spraying.

Mixture of conventional powders [% wt.]	
I	95% WC-12Co Amperit + 5% Fe_3O_4 Inflox
II	90% WC-12Co Amperit + 10% Fe_3O_4 Inflox
III	85% WC-12Co Amperit + 15% Fe_3O_4 Inflox
Mixture of nanostructured powders [% wt.]	
IV	95% WC-12Co Nanox + 5%Fe_3O_4 Nanox
V	90% WC-12Co Nanox + 10%Fe_3O_4 Nanox
VI	85% WC-12Co Nanox + 15%Fe_3O_4 Nanox

Mixtures for spraying composite coatings were obtained by stirring weighed out quantities of components in a V-type mixer (Fig. 6.12) for one hour.

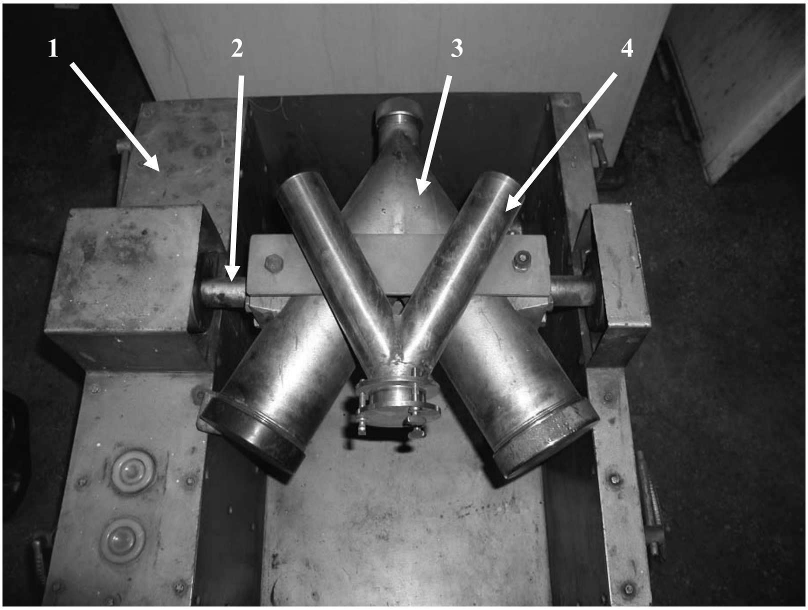

FIG. 6.12. V-type mixer: 1 – housing of mixer, 2 – shaft rotating containers for powder, 3 – container for big quantity of powder, 4 – container for small quantity of powder.

6.2.10. Residual Stresses in the HVOF Spray Coatings

Tests of residual stresses in coatings were conducted using Brucker D-8 Advance (λCoKα) diffractometer at the Faculty of Materials Engineering and Ceramics at the AGH University of Science and Technology. The measurements were carried out by applying a brand-new $g - \sin^2\psi$ method [145].

In order to measure factual and absolute elastic deformation and lattice tension of the crystal sample, it is necessary to measure the distance between atomic planes d_{hkl} in particular directions of the half-space above the sample (Fig. 6.13). To achieve this, appropriate systems of sample inclination (of the $S(i)$ coordinate system of the sample) against the measurement system $L(i)$ and diffraction plane are used.

The X-ray diffraction methods are based on the factual elastic deformations of crystal lattice in particular phases of crystal material and, therefore, they are used as model or verifying ones. They are measured with the distance between the crystallographic planes $\{hkl\}$.

The X-ray "$\sin^2\psi$" diffraction method enables determining both the directions and the values of main stresses; it also permits to measure anisotropic elastic constants E_{hkl} and ν_{hkl} related to the so-called X-ray elastic constants $1/2S_2(hkl)$ and $S_1(hkl)$, when having a determined external load.

The "$\sin^2\psi$" method combines Hooke's equations with for the plane state of tensions with deformation ellipsoid constituents in the coordinate system (S) and measurement system (L) of the sample (Fig. 6.13).

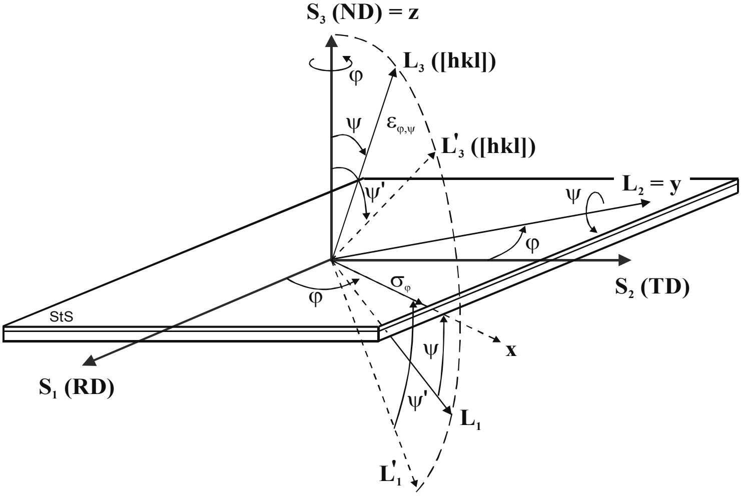

FIG. 6.13. Spatial system of beam course as well as deformations and tensions with a plane state of stresses on the sample substrate in the *S*(*i*) coordinates of the sample and the measurement system *L*(*i*). Diffraction register in the Bragg-Brentano symmetrical geometry [145].

The basic equation is as follows:

$$\varepsilon_{\varphi\psi} = S_{1,hkl}(\sigma_{11}^I + \sigma_{12}^I) + \frac{1}{2}S_{2,hkl}(hkl)(\sigma_{11}^I\cos^2\varphi + \sigma_{22}^I\sin^2\varphi + \sigma_{12}^I\sin^2\varphi)\sin^2\psi$$

$$= \frac{a_{\varphi\psi} - a_0}{a_0}$$

After certain simplifications and assuming a plane state of stresses, the following is obtained:

$$\varepsilon_{\varphi\psi} = 1/2S_2\sigma_\varphi\sin^2\psi + S_1(\sigma_1 + \sigma_2) = \frac{d_\psi - d_0}{d_0}$$

where: d_ψ, d_o – distances of crystallographic planes (*hkl*), $\varepsilon_{\varphi\psi}$– deformation in the direction of axis L_3.

Practical measurement consists in calculating deformations in the crystal lattice in given directions of the half-space above the sample, which are determined with angles φ and ψ. Several angles ψ are selected, depending on the expected measurement accuracy (in practice from 5 to 10); nevertheless, due to geometrical reasons, they should be angles ranging from 0^o to 60^o.

In order to calculate absolute value of stresses, the measurement of model material d_{hkl} is not necessary without stresses (d_0), since σ_φ is calculated with differentiation of the equation above. In this case, the following substitution is possible:

$$d^{hkl_o} = d^{hkl_\psi} = d_0$$

Such procedure makes this method a non-model one. Due to the procedure of measurement and calculations, measurement error is calculated for $n - 2$ degrees of freedom for confidence intervals $1 - \alpha = 0.9$; where α is the assumed error probability.

The principles if the $\sin^2\psi$ method can be applied in both types of goniometers, i.e. ψ and ω. In the case of the classical $\sin^2\psi$ method, there is a problem of changing X-ray penetration depth while altering angle ψ. It causes measurement errors, especially in the case of occurring tension gradients and heterogeneity of the structure and texture.

Such drawbacks and methodological limitations can be avoided by applying the geometry of constant angle of incidence for the diffraction measurement of crystal lattice deformations. This kind of measurement geometry can only be applied in goniometers ω. A variation of this method is given the term $g - \sin^2\psi$. General principles of measuring internal macrostressesin this variation of the method are similar to the typical $\sin^2\psi$ one.

The most substantial benefit of the $g - \sin^2\psi$ method is almost constant X-ray penetration depth, which is parallel to measurement depth. This measurement depth can be regulated with a selection of wavelength and angle of incidence. As can be concluded form the previous cases of applying a diffraction of the constant angle of incidence, particular benefits can be gained for thin and very thin coatings of substrate layers [141–147].

Internal stresses tests in supersonic spray coatings were performed on 30x30x3 mm samples made from PA6 aluminium alloy and steel C45.

Chapter 7

Properties of the Materials Used in the Composite Coatings

Constituting composite coatings is of particular interest when deposited in some areas, they enable considerable increase in functional properties of machine parts. The process of supersonic spraying provides a wide range of possibilities of obtaining composite coatings from composite materials, which are to constitute composite powders as well as mixtures of different powders. Applying composite coatings facilitates achieving much better properties of the coatings; however, it incurs huge costs [44, 88]. Those mixtures of powders that enable selecting composite components in a wide range are used most often.

7.1. Tungsten Carbide

Tungsten carbide is among those materials that have found a wide application in numerous branches of industry to increase resistance to wear and to reclaim machine parts. Its origin dates back to 1897, when a French chemist Henri Moissan conducted the first synthesis of tungsten carbide. The following tungsten carbides have found the widest application: W_2C (3.10% of C) and WC (6.13% of C). Tungsten dissolves ca. 0.05% of C at 2400°C. The first eutectic between a solid solution, rich in tungsten, and W_2C occurs at 1.5% of C at 2475°C. Tungsten W_2C has a melting point at 2850°C. A change of W_2C from αphase to γ phase at 2400°C takes place to the accompaniment of clearly audible cracks. Mechanical processing also contributes to a change of non-durable α W_2C into γ. The second eutectic, i.e. W_2C – WC, melts at 2525°C and contains ca. 4.5% of C. Tungsten carbide WC disintegrates at 2800°C into a liquid rich in tungsten, W_2C and carbon. The basic features of tungsten carbide are: a high melting point, high level of hardness, resistance to wear and corrosion at ambient and high temperatures. The boiling point of tungsten carbides is extremely high (6000°C - WC). Tungsten carbide WC (6.13% of C) is a grey metallic powder. Acids have an inhibited impact upon it, i.e. a mixture of nitric and hydrofluoric acids at a ratio of 1:4 does not dissolve WC, though it dissolves W_2C. It is Cl-resistant until 400°C, whilst a violent reaction occurs at 600-800°C. Tungsten carbide W_2C (6.13% of C) is resistant to the impact of cold non-organic acids. Nitric acid dissolves it when hot. In an oxygen stream W_2C burns at 600°C to obtain WO_2. The hardness of W_2C on the Mohs scale reaches 9, whilst microhardness 30,000 N/mm^2 with a load of 500 N, whereas the microhardness of WC reaches 24,000 N/mm^2 with a load of 500 N (or 25,000 N/mm^2 with 300 N). It is impossible to determine the exact melting point of WC due to the fact that it disintegrates while melting. The melting point of WC is 2700-2800°C. Carbides used in pure form are very hard and resistant to the impact of high temperatures, but then particular grains are loosely connected with one another and the substrate. For this reason, tungsten carbide WC is applied in the form of a sinter with cobalt which guarantees high durability. Moreover, its hardness is not subject to changes because of temperature. Sintered tungsten carbide was first used in Germany during World War I to manufacture drawing dies used to produce tungsten lamp filaments. Next, tungsten carbides were applied to produce cutting tools and machine parts. Positive results of applying sintered tungsten carbides resulted in introducing into the market a sinter containing 6% of cobalt under the name "Widia" (wie Diamant) and its popularization in numerous applications. The introduction of plasma spraying into the industry opened new possibilities in mid-50's. Plasma-sprayed coatings WC-Co had very good properties; however, the impact of a plasma stream at a high temperature as well as the presence of oxygen caused partial disintegration of WC. Detonation-sprayed coatings, which were introduced into industry at the same period of time, possessed much better properties. Nevertheless, this method was patented by Union Carbide (currently Praxair S.T., Inc.) and due to commercial considerations was not popularized. Breaking the monopoly of Union Carbide Inc. took place at the beginning of 1980's [52, 112], when Browning Engineering developed continuous supersonic spraying process, i.e. High Velocity Oxygen Fuel Spraying (HVOF) which was competitive to detonation spraying. The current supersonically-sprayed coatings WC-Co have found a wide range of applications in industry with the purpose of increasing the resistance of machine parts to abrasive wear, erosion and corrosion [24, 27, 34, 158, 187, 189, 193, 200].

In this work, conventional powder WC-12Co developed by Amperit 519.074 and the nanostructured powder WC-12Co Nanox™S7412 developed by Inframat Advanced Materials were applied onto the composite coatings matrix.

7.2. Iron Oxides

In nature, iron oxides are present in three forms depending on the temperature of the surrounding and the pressure.

Ferric oxide FeO, called wustite, is a body, black in colour, in which iron occurs in the II degree of oxidation. It rarely occurs in a single state, it constitutes a solid phase only at a temperature higher than 575°C. During slow cooling, below this temperature, it is subject to disintegration into magnetite Fe_2O_3 or ferro-ferric oxide Fe_3O_4. Ferrous oxide is a non-stoichiometric compound, formula FeO does not correspond to its actual composition. It usually contains less iron, whose content varies between 0.8150 and 0.9460. Regardless of the composition, the same crystal structure is retained; wustite has a regular crystallographic lattice space-centred type NaCl (Fig. 7.1).

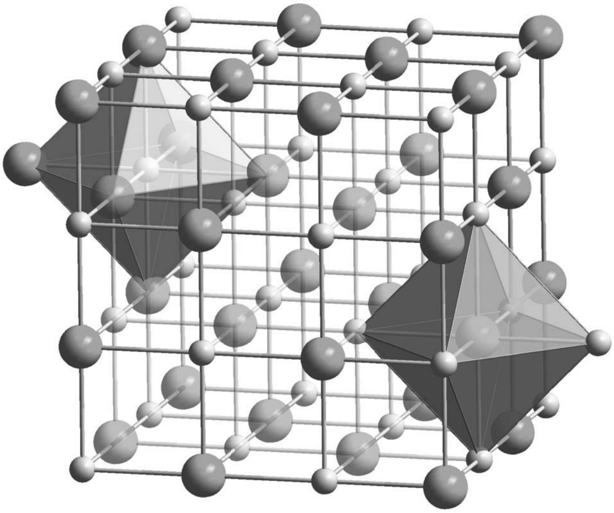

FIG. 7.1. Face-centred cubic structure of FeO [46].

Ferrous oxide **Fe_2O_3** occurs in two polymorphic forms. Type α- Fe_2O_3 is durable in normal conditions, pink and red in colour, and occurs in the form of hematite. Its crystal lattice is rhombohedral, corundum-type with an elementary cell which comprises 30 atoms. Ions O^{2-} constitute a hexagonal sublattice within it, whilst ions Fe^{2+} are octahedral filling in 2/3 of such lattice units. A slight loss of oxygen ions causes transforming the rhombohedral lattice of this type into a spinel-type space-centred lattice (a regular system) which is correspondent to the ferromagnetic type γ- Fe_2O_3. It is a non-durable type and, while losing further oxygen ions, gradually transforms into magnetite. Type γ- Fe_2O_3 called maghemite is non-durable and it possesses ferromagnetic properties. It is obtained during a careful oxidation of magnetite. During heating at 427°C it is transformed into a hematite.

Ferro-ferric oxide Fe_3O_4, ($FeO{\cdot}Fe_2O_3$) is a black-coloured body in which oxygen occurs at the II and III degrees of oxidation. Its melting point is 1538°C. In nature it is present as a mineral called magnetite which possesses ferromagnetic properties. It is obtained as a result of burning iron in oxygen; it is present on the surface of iron heated to the temperature of a glow. It has a reverse-spinel type space lattice, whose elementary cell is composed of 32 oxygen atoms and 24 atoms of iron (Fig. 7.2). It possesses high resistance to acids and reagents with an oxidation effect.

Iron oxides are currently a component of many composite coatings, in which they are responsible for their tribological properties. For plasma-sprayed and PTWA-sprayed coatings on the surfaces of cylinders of combustion car engines, in the conditions of heavy loads and high temperatures, oxides FeO and Fe_3O_4 play a fundamental role in friction processes. The presence of Fe_2O_3 in the coating considerably increases resistance to wear [Barb-2006, Ford]. Composite materials for spraying containing iron oxides in their composition have been used in numerous applications for many years. It is recommended to apply a mixture of 40% of Cr_3C_2 and 60% of Fe_3O_4 for one of the solutions for plasma spraying of piston rings and cylinder liners [15]. The presence of a thin film of wustite on the sprayed steel substrate additionally increases the adhesion of the sprayed coatings [164].

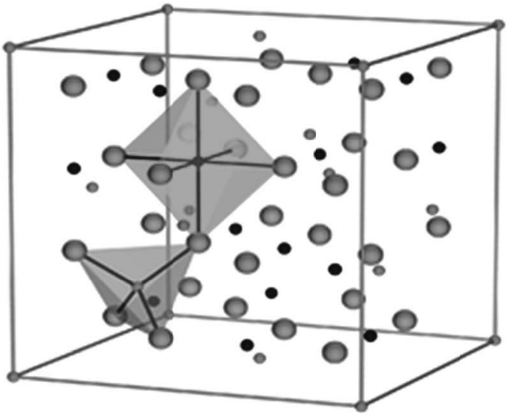

FIG. 7.2. Space lattice of Fe_3O_4 (the ball: grey – ion O^{2-}, green – tetrahedral ions of iron (Fe^{3+}); sublattice A: blue – octahedral ions of iron (Fe^{2+}, Fe^{3+}), sublattice B.

Ferro-ferric oxide Fe_3O_4 was applied as a solid lubricant for the composite coating. Its crystal structure as well as the findings in literature allow to assume that it has the properties of a solid lubricant [6]. In this work, a composite powder Fe_3O_4Inflox™26FE23 and nanostructured Fe_3O_4 Nanox™26FE23 were applied, both of them delivered by Inframat Advanced Materials.

Chapter 8

Properties of the Spray Powders

Powders utilized for supersonic spraying have a vital impact on the course of the very spraying process and the properties of the obtained coating. Basic properties of powder include chemical and phase composition, and granulometric decomposition. Additionally, the morphology of powder grains is of paramount importance due to the fact that even powders with identical chemical composition and granulometric decomposition may vary because they were made with use of different methods. As a consequence, their mutual interaction with the stream proceeds disparately, which affects the properties of the sprayed coating. Determining these properties is essential since producers do not provide information about them, whereas the given data do not always coincide with test results.

8.1. Granulometric Composition of the Spray Powders

The course of cumulative decomposition curves and relative decomposition of grain density for WC-12Co Amperit powder (Fig. 8.1) illustrates that it is powder with a narrow range of granulation utilized in thermal spraying. It is evident having analysed the tangent of the cumulative decomposition curve $n = 4.07$, and the following values $d_{10} = 21.59$ μm, $d_{50} = 31.68$ μm, and $d_{90} = 43.37$ μm determining granulation of 10, 20, and 90% of the test on the basis of cumulative decomposition. The results of the granulometric test showed that the range of grain size for this powder does not coincide with the one provided by the producer, i.e. 15-45 μm. This powder has a minute percentage of grains larger than 15 μm, i.e. 3.88% for 18 μm and a greater percentage of grains larger than 45 μm, i.e. 97.18% for 51 μm. On the basis of the analysis, grain size ranges from 18 to 55 μm.

The course of cumulative decomposition curves and relative decomposition of grain density for WC-12Co Nanox S7412 powder (Fig. 8.2) indicates that it is also powder with granulation range utilized in thermal spraying but wider than in the case of WC-12Co Amperit powder. It is visible having analysed lower tangent of the cumulative decomposition curve $n = 2.33$, and the following values $d_{10} = 22.70$ μm, $d_{50} = 34.52$ μm, and $d_{90} = 61.28$ μm determining granulation of 10, 20, and 90% of the test on the basis of cumulative decomposition. The results of the granulometric test showed that the range of grain size for this powder does not coincide with the one provided by the producer, i.e. 5-45 μm. This powder has a minute percentage of grains larger than 5 μm, i.e. 5.83% for 21 μm and a greater percentage of grains larger than 45 μm, i.e. 97.79% for 103 μm. On the basis of the analysis, grain size ranges from 21 to 103 μm.

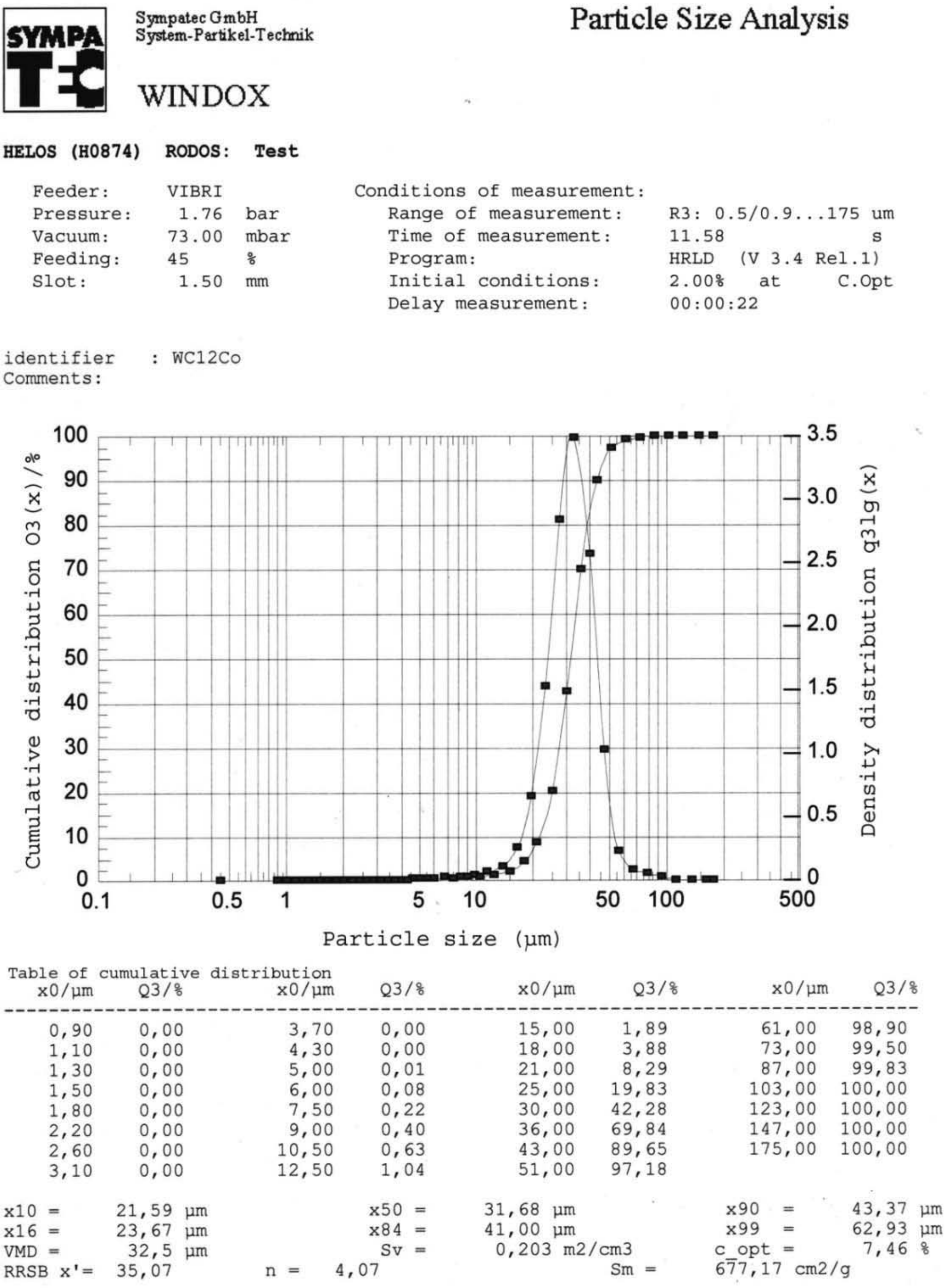

Sympatec GmbH
System-Partikel-Technik

WINDOX

Particle Size Analysis

```
HELOS (H0874)  RODOS:  Test

   Feeder:     VIBRI            Conditions of measurement:
   Pressure:    1.76  bar          Range of measurement:    R3: 0.5/0.9...175 um
   Vacuum:     73.00  mbar         Time of measurement:     11.58             s
   Feeding:    45     %            Program:                 HRLD  (V 3.4 Rel.1)
   Slot:        1.50  mm           Initial conditions:      2.00%   at    C.Opt
                                   Delay measurement:       00:00:22

identifier   : WC12Co
Comments:
```

```
Table of cumulative distribution
   x0/µm     Q3/%          x0/µm     Q3/%          x0/µm      Q3/%          x0/µm     Q3/%
--------------------------------------------------------------------------------------------
   0,90      0,00          3,70      0,00          15,00      1,89          61,00     98,90
   1,10      0,00          4,30      0,00          18,00      3,88          73,00     99,50
   1,30      0,00          5,00      0,01          21,00      8,29          87,00     99,83
   1,50      0,00          6,00      0,08          25,00     19,83         103,00    100,00
   1,80      0,00          7,50      0,22          30,00     42,28         123,00    100,00
   2,20      0,00          9,00      0,40          36,00     69,84         147,00    100,00
   2,60      0,00         10,50      0,63          43,00     89,65         175,00    100,00
   3,10      0,00         12,50      1,04          51,00     97,18

x10 =      21,59 µm              x50 =    31,68 µm              x90   =     43,37 µm
x16 =      23,67 µm              x84 =    41,00 µm              x99   =     62,93 µm
VMD =       32,5 µm               Sv =    0,203 m2/cm3          c_opt =      7,46 %
RRSB x'=   35,07         n =    4,07                   Sm =     677,17 cm2/g
```

FIG. 8.1. Cumulative distribution and density distribution WC-12Co Amperit powder.

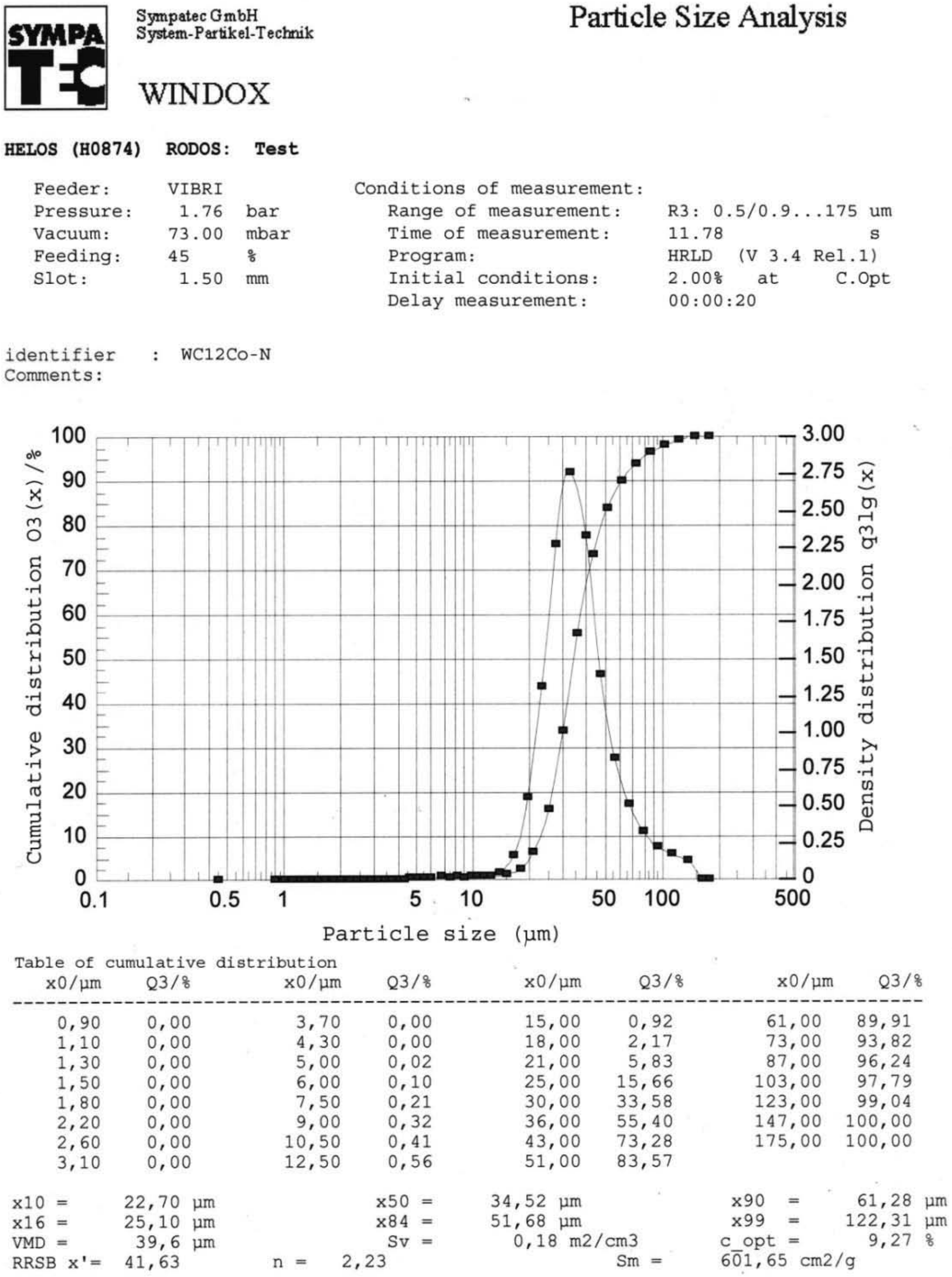

Sympatec GmbH
System-Partikel-Technik

WINDOX

Particle Size Analysis

```
HELOS (H0874)   RODOS:   Test

  Feeder:       VIBRI           Conditions of measurement:
  Pressure:      1.76   bar        Range of measurement:     R3: 0.5/0.9...175 um
  Vacuum:       73.00   mbar       Time of measurement:      11.78               s
  Feeding:      45      %          Program:                  HRLD  (V 3.4 Rel.1)
  Slot:          1.50   mm         Initial conditions:       2.00%    at      C.Opt
                                   Delay measurement:        00:00:20

identifier    :  WC12Co-N
Comments:
```

```
 Table of cumulative distribution
   x0/µm     Q3/%          x0/µm     Q3/%          x0/µm      Q3/%          x0/µm     Q3/%
-------------------------------------------------------------------------------------------
    0,90     0,00           3,70     0,00          15,00      0,92          61,00    89,91
    1,10     0,00           4,30     0,00          18,00      2,17          73,00    93,82
    1,30     0,00           5,00     0,02          21,00      5,83          87,00    96,24
    1,50     0,00           6,00     0,10          25,00     15,66         103,00    97,79
    1,80     0,00           7,50     0,21          30,00     33,58         123,00    99,04
    2,20     0,00           9,00     0,32          36,00     55,40         147,00   100,00
    2,60     0,00          10,50     0,41          43,00     73,28         175,00   100,00
    3,10     0,00          12,50     0,56          51,00     83,57

 x10 =       22,70 µm              x50 =      34,52 µm              x90   =      61,28 µm
 x16 =       25,10 µm              x84 =      51,68 µm              x99   =     122,31 µm
 VMD =        39,6 µm               Sv =       0,18 m2/cm3          c_opt =       9,27 %
 RRSB x'=    41,63        n =    2,23                        Sm =   601,65 cm2/g
```

FIG. 8.2. Cumulative distribution and density distribution WC-12Co Nanox powder.

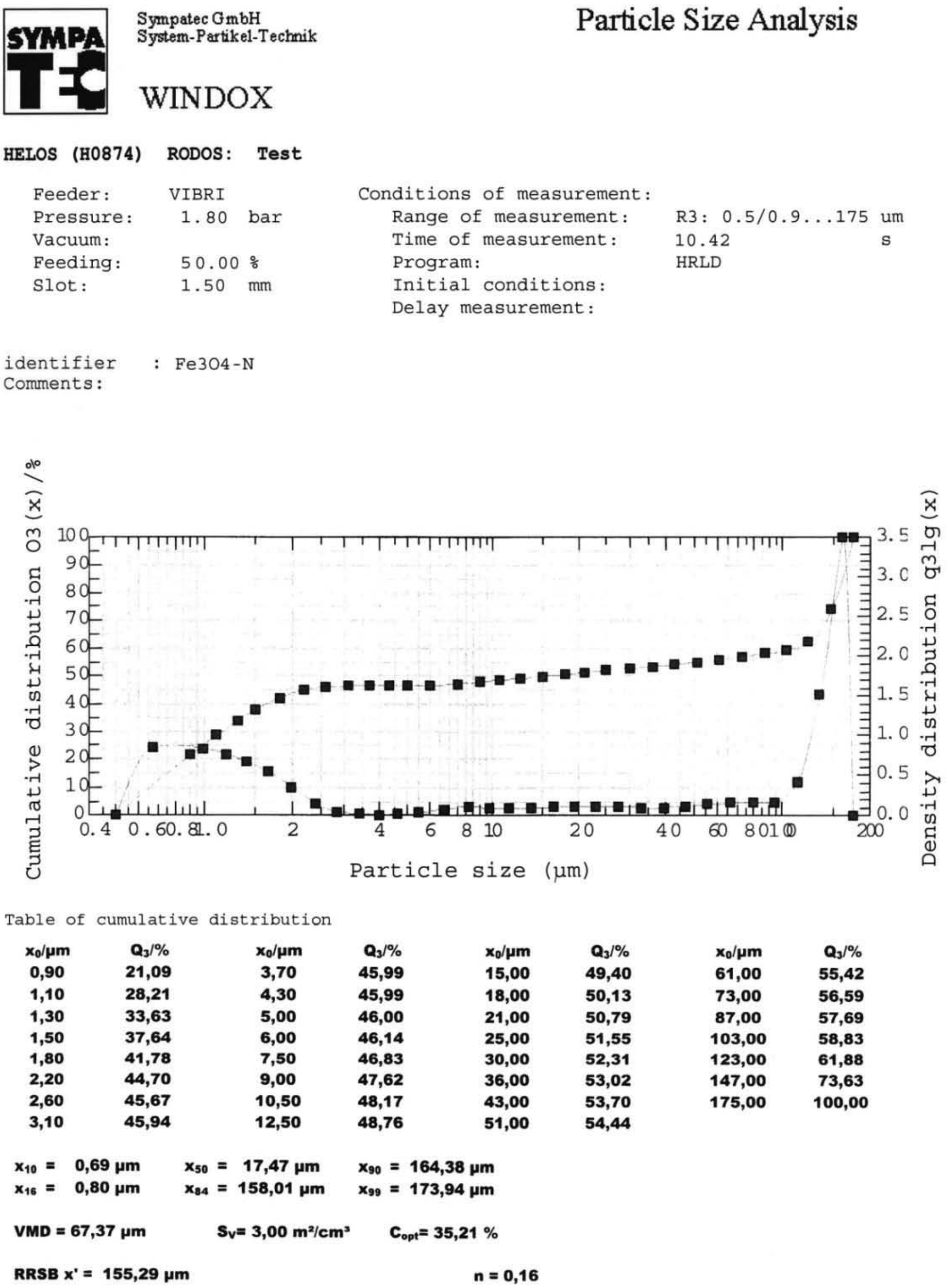

Sympatec GmbH
System-Partikel-Technik

WINDOX

Particle Size Analysis

HELOS (H0874) RODOS: Test

```
Feeder:      VIBRI          Conditions of measurement:
Pressure:     1.80  bar        Range of measurement:     R3: 0.5/0.9...175 um
Vacuum:                        Time of measurement:      10.42            s
Feeding:      50.00 %          Program:                  HRLD
Slot:         1.50   mm        Initial conditions:
                               Delay measurement:

identifier   : Fe3O4-N
Comments:
```

Table of cumulative distribution

x_0/µm	Q_3/%	x_0/µm	Q_3/%	x_0/µm	Q_3/%	x_0/µm	Q_3/%
0,90	21,09	3,70	45,99	15,00	49,40	61,00	55,42
1,10	28,21	4,30	45,99	18,00	50,13	73,00	56,59
1,30	33,63	5,00	46,00	21,00	50,79	87,00	57,69
1,50	37,64	6,00	46,14	25,00	51,55	103,00	58,83
1,80	41,78	7,50	46,83	30,00	52,31	123,00	61,88
2,20	44,70	9,00	47,62	36,00	53,02	147,00	73,63
2,60	45,67	10,50	48,17	43,00	53,70	175,00	100,00
3,10	45,94	12,50	48,76	51,00	54,44		

x_{10} = 0,69 µm **x_{50} = 17,47 µm** **x_{90} = 164,38 µm**
x_{16} = 0,80 µm **x_{84} = 158,01 µm** **x_{99} = 173,94 µm**

VMD = 67,37 µm **S_V= 3,00 m²/cm³** **C_{opt}= 35,21 %**

RRSB x' = 155,29 µm **n = 0,16**

FIG. 8.3. Cumulative distribution and density distribution Fe_3O_4 Inflox™26FE23 powder.

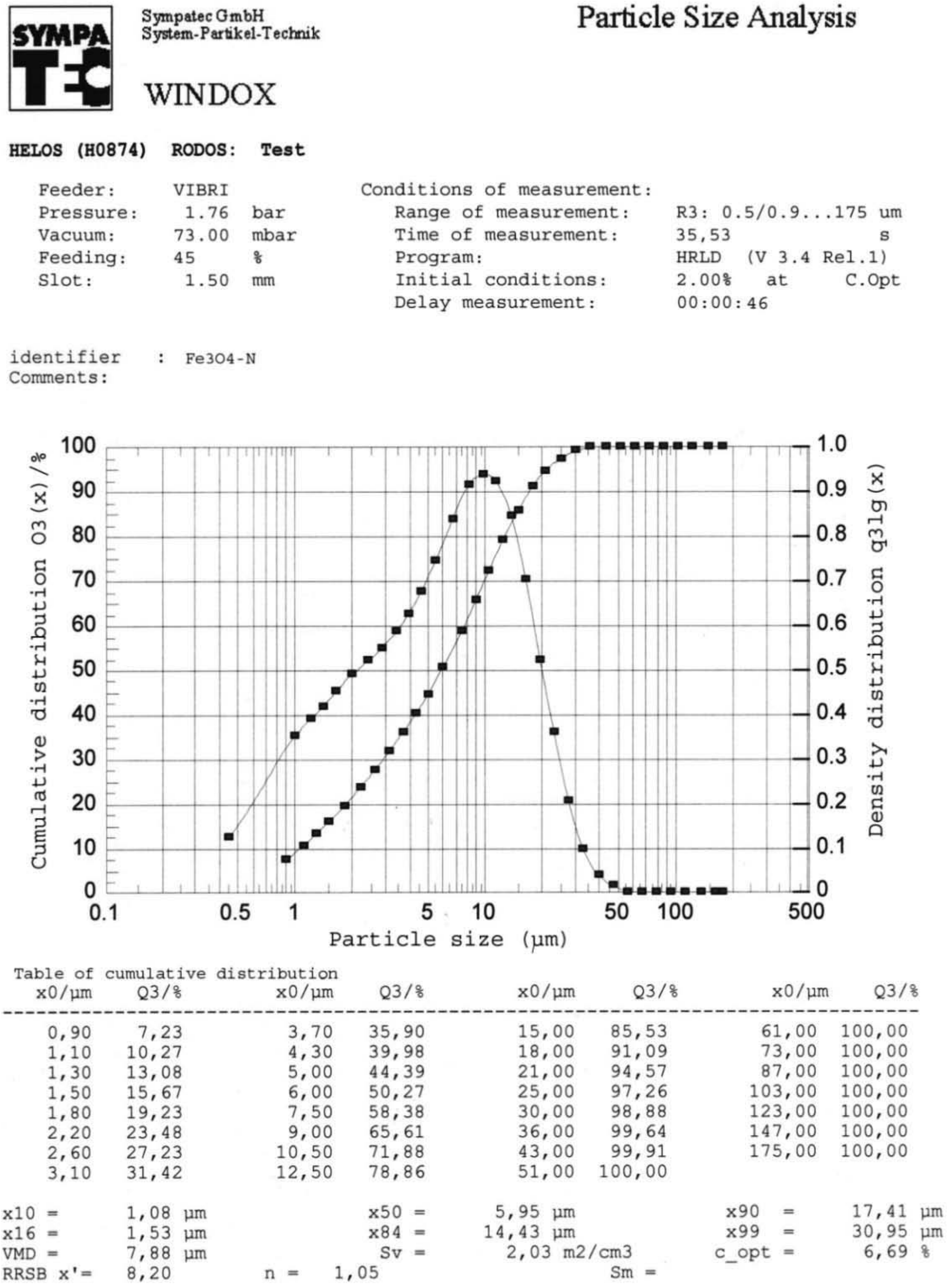

Sympatec GmbH
System-Partikel-Technik

WINDOX

Particle Size Analysis

```
HELOS (H0874)  RODOS:  Test

   Feeder:      VIBRI             Conditions of measurement:
   Pressure:     1.76   bar          Range of measurement:     R3: 0.5/0.9...175 um
   Vacuum:      73.00   mbar         Time of measurement:      35,53             s
   Feeding:     45      %            Program:                  HRLD   (V 3.4 Rel.1)
   Slot:         1.50   mm           Initial conditions:       2.00%    at      C.Opt
                                     Delay measurement:        00:00:46

identifier   :  Fe3O4-N
Comments:

 Table of cumulative distribution
   x0/µm     Q3/%          x0/µm     Q3/%         x0/µm     Q3/%         x0/µm     Q3/%
-------------------------------------------------------------------------------------
     0,90     7,23          3,70    35,90         15,00    85,53         61,00   100,00
     1,10    10,27          4,30    39,98         18,00    91,09         73,00   100,00
     1,30    13,08          5,00    44,39         21,00    94,57         87,00   100,00
     1,50    15,67          6,00    50,27         25,00    97,26        103,00   100,00
     1,80    19,23          7,50    58,38         30,00    98,88        123,00   100,00
     2,20    23,48          9,00    65,61         36,00    99,64        147,00   100,00
     2,60    27,23         10,50    71,88         43,00    99,91        175,00   100,00
     3,10    31,42         12,50    78,86         51,00   100,00

x10 =        1,08  µm                x50 =     5,95 µm           x90   =     17,41  µm
x16 =        1,53  µm                x84 =    14,43 µm           x99   =     30,95  µm
VMD =        7,88  µm                Sv =      2,03 m2/cm3       c_opt =      6,69  %
RRSB x'=     8,20           n =    1,05                 Sm =
```

FIG. 8.4. Cumulative distribution and density distribution Fe_3O_4 Nanox™26FE23 powder.

The course of cumulative decomposition curves and relative decomposition of grain density for Fe_3O_4Inflox™26FE23 powder (Fig. 8.3) indicates that it is powder with a very wide range of granulation. The tangent of the cumulative decomposition curve $n = 0.16$. The range of granulation takes values from 0.9 to as many as 175 μm; however, grains of a size smaller than 0.9 μm constitute as much as 21.09% of the powder.

The course of cumulative decomposition curves and relative decomposition of grain density for Fe_3O_4Nanox™26FE23 powder (Fig. 8.4) illustrates the fact that it is powder with a wide range of granulation as well, especially in the case of minute grains. It is noticeable having analysed lower tangent of the cumulative decomposition curve $n = 1.05$, and the following values $d_{10} = 1.08$ μm, $d_{50} = 5.95$ μm, and $d_{90} = 17.41$ μm determining granulation of 10, 20, and 90% of the test on the basis of cumulative decomposition. The conclusion to be drawn from the above analysis is that this powder has a substantial percentage of minute grains. The quantity of grains smaller than 0.9 μm is 7.23%, whereas 97.23% are grains smaller than 25 μm. On the basis of the analysis, grain size ranges from 0.9 to 25 μm.

8.2. Morphology of the Powder Particles

Powders for thermal spraying can be obtained by diverse technologies; that is why, their morphology is heterogeneous. Ball-shaped grains are the most desirable; the ball-shape increases its looseness thus facilitating its insertion into the spray stream. Moreover, spherical shape permits even heating of the whole grain during its dwelling time in the spray stream.

8.2.1. Morphology of the Amperit 519.074 WC-12Co Powder Particles

The shape of WC-12Co Amperit powder grains is shown in Figures 8.5a and 8.5b. The grains are ball-shaped which is typical of powders obtained by agglomerating and sintering. A considerable difference in the size of grains is noticeable, especially the percentage of minute grains, up to 18 μm, which is 3.88% (Fig. 8.2). Powder producer claims in its description that a single grain is composed of tungsten carbide grains which are 1 μm. Analyse of the surface of the powder grain (Fig. 8.6) confirms this information: grains of tungsten carbide of the given size on its surface and in microsections of powder grains (Fig. 8.7a and 8.7b). Microsections of powder grains exhibit considerable porosity, which is supported by linear analysis, i.e. in the places of pore occurrence there is neither tungsten nor cobalt.

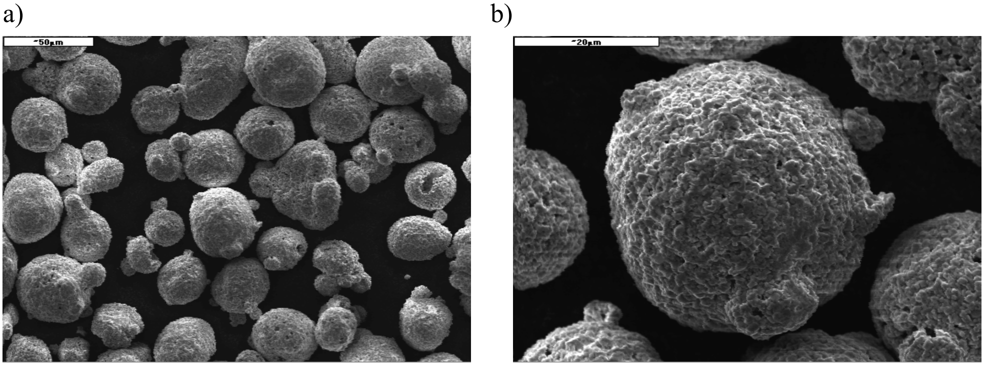

Fig. 8.5. Morphology of WC-12Co Amperit powder grains: a) magnified 500x, b) magnified 2000x.

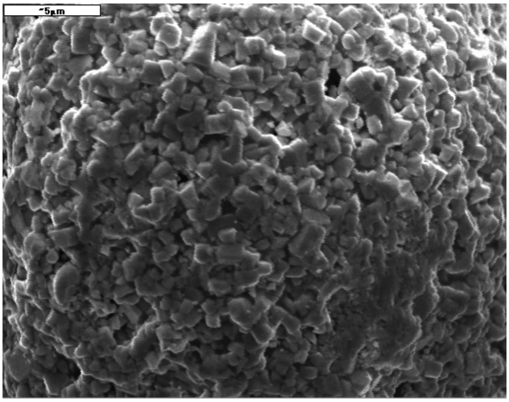

Fig. 8.6. Morphology of the surface of WC-12Co Amperit powder grains; magnified 5000x.

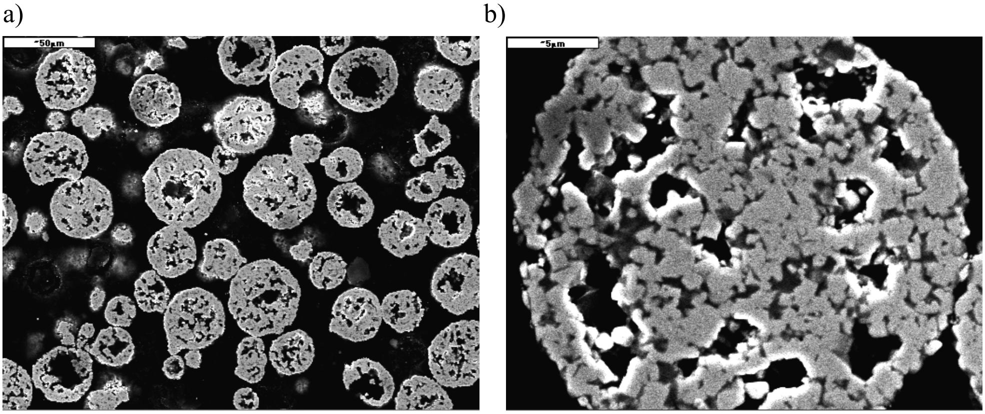

Fig. 8.7. Morphology of the cross section of WC-12Co Amperit powder grains: a) magnified 500x, b) magnified 5000x.

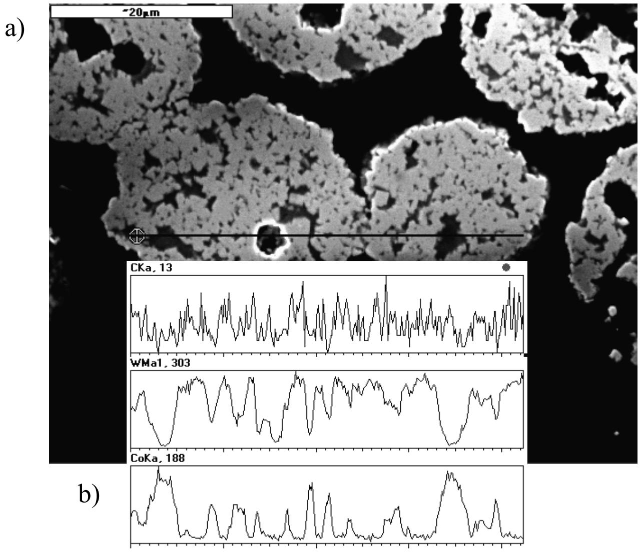

FIG. 8.8. Morphology of the cross section of a WC-12Co Amperit powder grain: a) magnified 2000x, b) linear analysis.

8.2.2. Morphology of the Nanox WC-12Co Powder Particles

The shape of the grains WC-12Co Nanox is presented in Figures 8.9a and 8.9b. The grains are of irregular shape; a part of them is spherical. The structure of the grains is typical of the powders formed as a result of agglomeration and sintering. Significant diversity in powder grains which could result from the analysis of granulometric composition is not apparent; nor is the presence of large grains in the obtained powder sample. The producer of the powder in the description states that a single grain of the powder is built from wolfram carbide sized 100 to 500 nm. The analysis of grain surface (Fig. 8.9c) makes it possible to confirm this information, particularly in comparison to the surface of a grain of conventional structure (Fig. 8.6c). Tungsten carbide particles sized 100 to 500 nm are visible on the powder grain surface, however, the accurate definition of their size requires analyzing the grain at higher magnification. Significant porosity can be seen in the microsection of powder grains (Fig. 8.10a). The linear analysis conducted in the site of the dark phase showed high level of cobalt count and low level of tungsten count, which indicates the lack of tungsten carbide in the analyzed site (Fig. 8.11a and 8.11.b). Therefore, it appears that the dark phase is an area were the cobalt wrap is present.

The conducted analysis of the grain surface of the WC-12Co Nanox powder at high magnification (Fig. 8.11a) showed that the grain is built from the WC particles of very various shape and size. This diversification is visible in Figure 8.11b; the tungsten carbide grains comprising the composition of a single powder grain measure from several dozen nanometers to one micrometer.

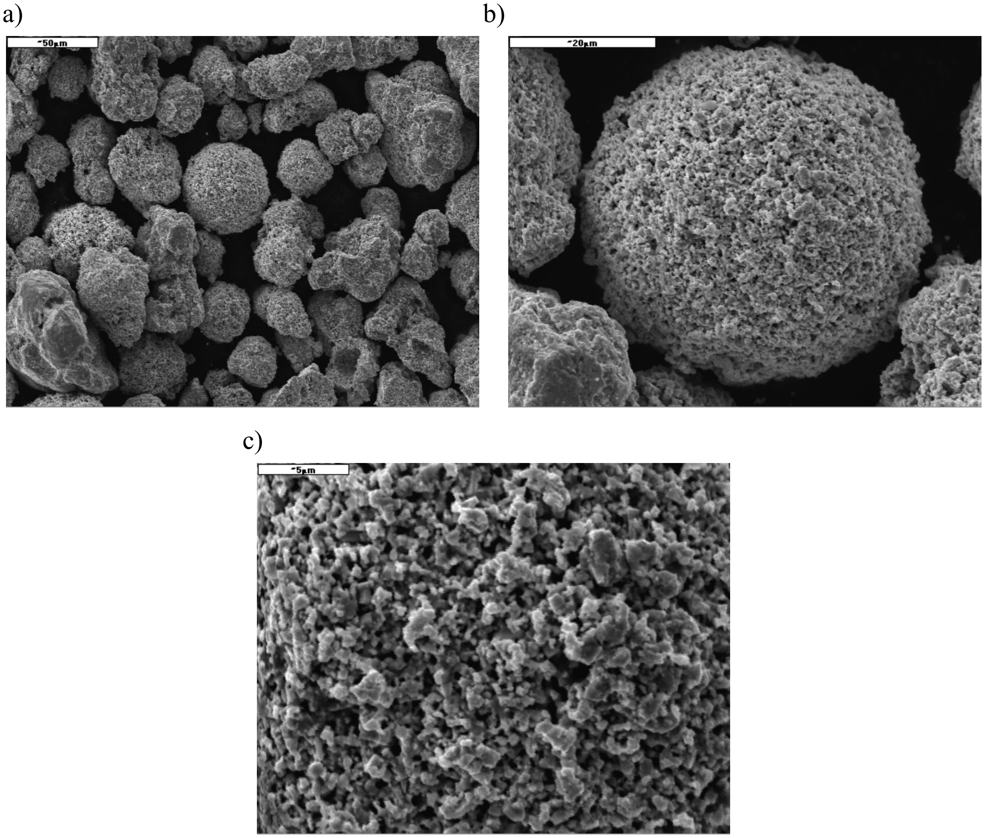

Fig. 8.9. Morphology of WC-12Co Nanox powder grains: a) magnification 500x, b) magnified 2000x, c) magnified 5000x.

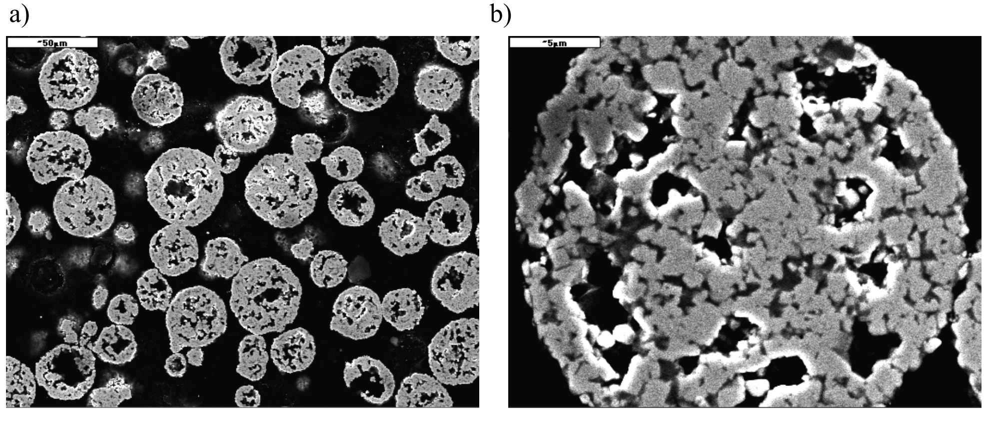

Fig. 8.10. Morphology of WC-12Co Nanox powder grains cross-section: a) magnified 500x, b) magnified 5000x.

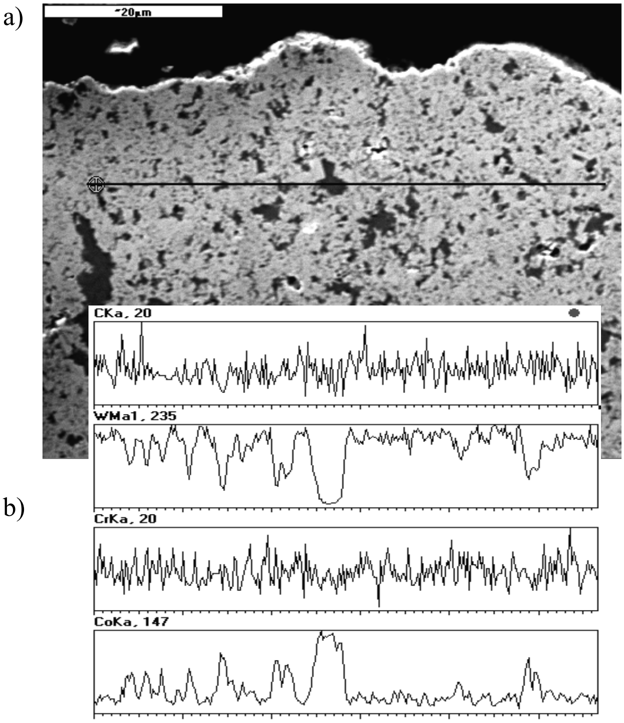

FIG. 8.11. Morphology of WC-12Co Nanox powder grains cross-section: a) magnified 2000x, b) linear analysis.

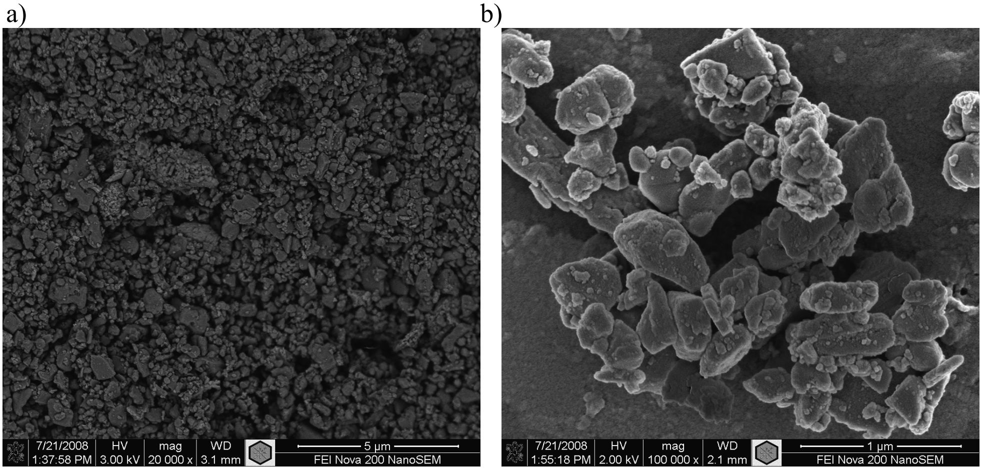

FIG. 8.12. Morphology of WC-12Co Nanox powder grains surface: a) magnified 20 000x, b) magnified 100 000x.

Figure 8.13a illustrates the HAADF picture of WC particle which dimension is 1 μm. Changing contrast within the grain is related to a different orientation of two neighbouring grains the size of which is over 500 nm. EDS spectra made from points indicated in the HAADF picture point to the occurrence of the WC grain with a scarce content of cobalt (Fig. 8.13b).

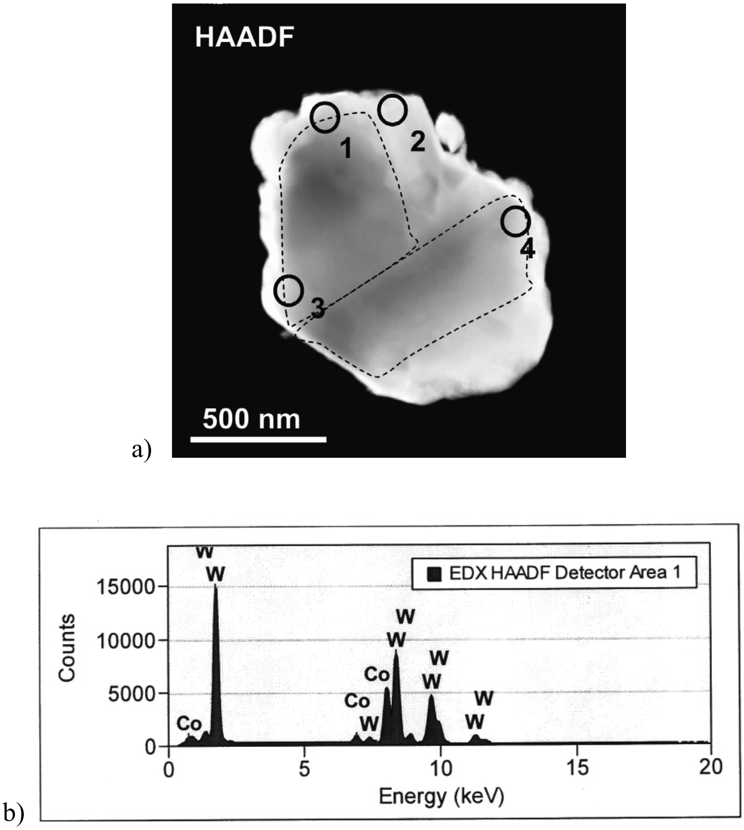

FIG. 8.13. WC particle: a) HAADF picture, b) EDS analysis.

Figure 8.14a illustrates the HAADF picture of two WC grains, which dimensions are 1 μm. The conducted EDS analysis from three places of the first grain and from the square surface of the second grain proves the occurrence of WC and Co. Quantitative analysis from the square surface pointed out that there is ca. 3.5% of weight (10.5% of atoms) of Co in WC grain.

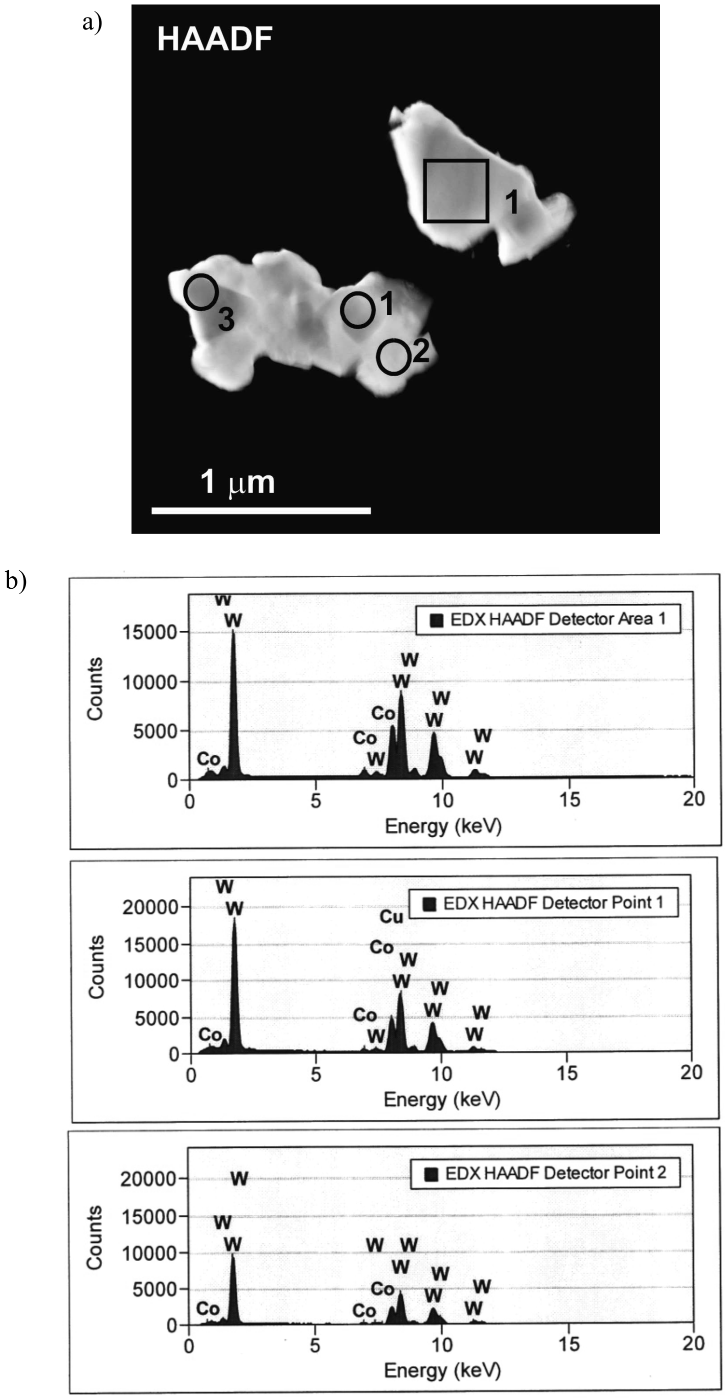

FIG. 8.14. Two WC grains: a) HAADF picture, b) EDS analysis.

Figure 8.15 shows the BF picture (Figs. 8.15a and 8.15b) and the SADP picture (Fig 8.15c) of the WC grain analysed in Figure 8.14. Point diffraction taken from one WC grain is noticeable in the picture of electron diffraction. The diffraction was completed with an outstanding adjustment to the hexagonal phase of WC with a lattice parameter $a = b = 2.9065$, $c = 8366$ Å and orientation [110].

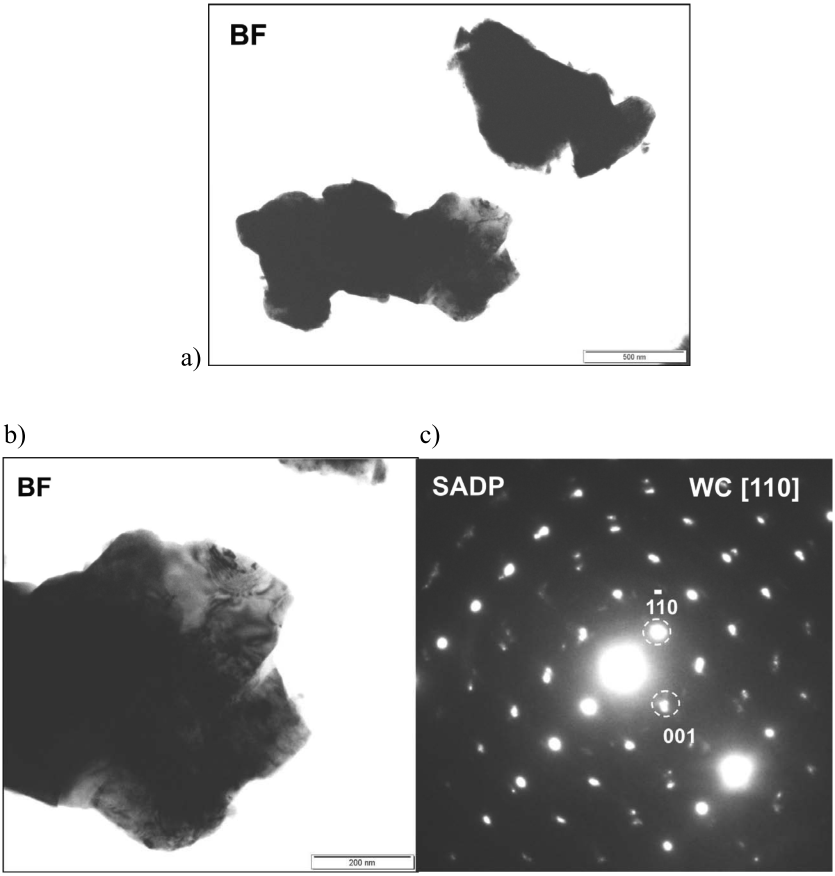

FIG. 8.15. WC grains: a) picture in the bright field (BF), b) electron diffraction (SAADF).

Figure 8.16a presents the HAADF picture of two WC grains (size 1 μm) and the map of decomposition of chemical elements taken from the area marked with a rectangle. In the HAADF picture it is noticeable that the size of single grains in the elongated grain is 300 nm. It is confirmed by the decomposition of particular chemical elements (Fig. 8.16b). In the picture of CoKα concentration there are minute, several nanometres in size, Co grains homogeneously distributed in the WC grain.

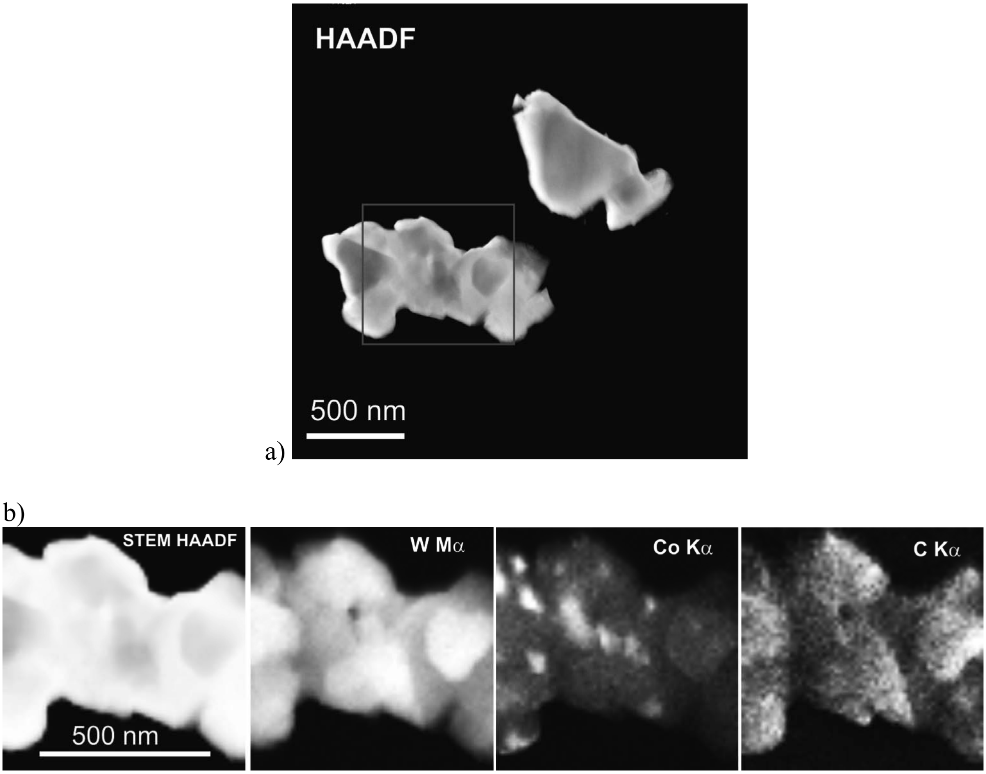

FIG. 8.16. WC grains: a) the HAADF picture, b) map of elements distribution.

8.2.3. Morphology of the Inflox™26FE23 Fe_3O_4 Powder Particles

The shape of Fe_3O_4Inflox™26FE23 powder grains is shown in Figure 8.17. Some powder grains have a regular spherical shape which is typical of powders obtained by agglomerating and sintering. Several spherical grains are damaged and have cracks. A huge percentage of fine grains is noticeable, with flake structure, which very often adhere to larger spherical grains (Fig. 8.17a). Analysing the surface of spherical powder grain (Fig. 8.17b and 8.17c) leads to a statement that they are composed of submicrometric and nanometric Fe_3O_4 grains among which there are pores. These grain were formed as result of sintering nanocrystals of nanometric size (Fig. 8.17d). Significant amount of pores can be seen in the powder cross-section (Fig. 8.18a). Linear analysis (Fig. 8.19a and 8.19b) depicted a varied course of calculations for oxygen and iron at different levels, which is probably related to the occurrence of micropores among Fe_3O_4 grains.

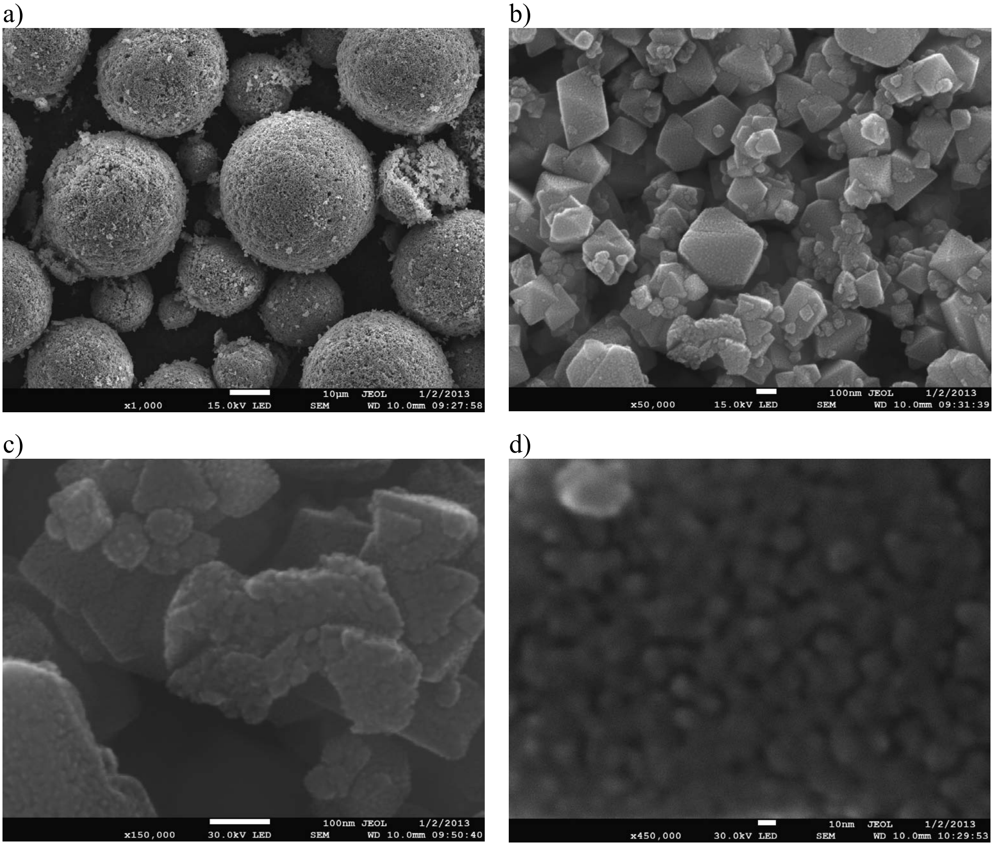

FIG. 8.17. Morphology of Fe_3O_4 Inflox powder grains: a) magnified 1000x, b) magnified 5000x, c) magnified 150000x, d) magnified 450000x.

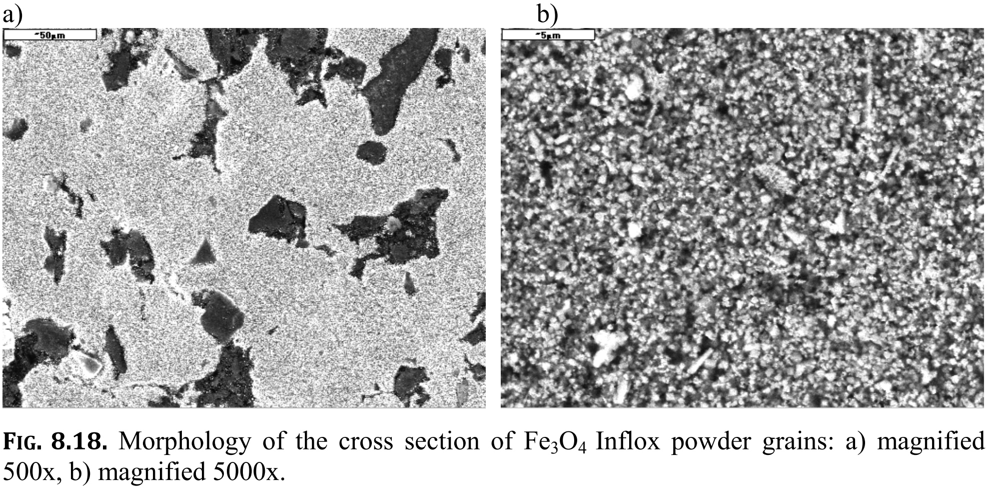

FIG. 8.18. Morphology of the cross section of Fe_3O_4 Inflox powder grains: a) magnified 500x, b) magnified 5000x.

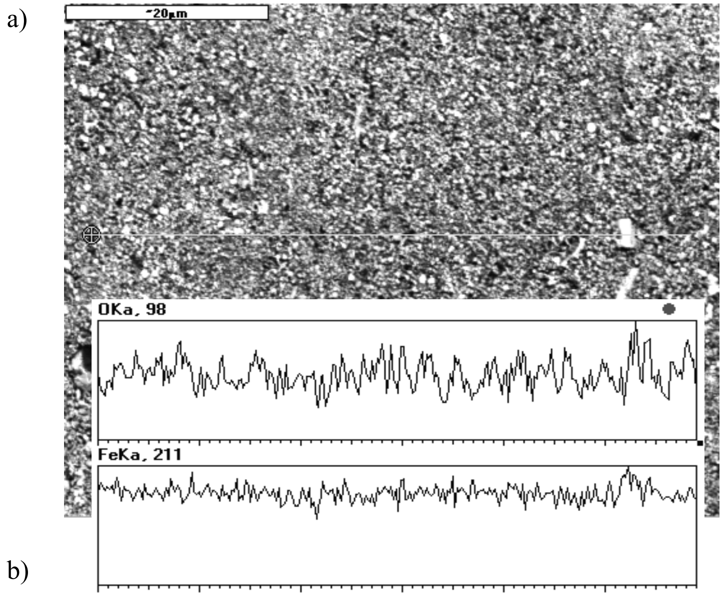

FIG. 8.19. Morphology of the cross section of a Fe_3O_4 Inflox powder grain: a) magnified 2000x, b) linear analysis.

8.2.4. Morphology of the Nanox™26FE23 Fe_3O_4 Powder Particles

The shape of Fe_3O_4 Nanox™26FE23 powder grains and the morphology of their surface are illustrated in Figure 8.20. Some of the grains have irregular spherical shape. Powder was obtained as a result of agglomerating and sintering of Fe_3O_4Inflox™26FE23 minute grains of diverse size and irregular shapes. There are also visible fine grains, of much smaller size (Fig. 8.20a). Analysis of the surface of spherical powder grain (Figs. 8.20b,c,d) leads to a statement that they are composed of submicrometric Fe_3O_4 nanocrystal grains. Substantial porosity is observable in the microsections of powder grains (Figs. 8.21a and 8.21b). Diverse grain composition is visible in the powder grain microsection at a magnification of 5000x. The conducted linear analysis (Figs. 8.19a and 8.19b) shows quite diversified course of calculations for oxygen and iron, which is probably connected with the occurrence of micropores among Fe_3O_4 grains.

Figure 8.23 illustrates a picture of microstructure of Fe_3O_4 powder particle in the bright field (BF) (Fig. 8.23a), in the dark field (DF) (Fig. 8.23b), and the correspondent electron diffraction (SADP) (Fig. 8.23 c). A circle in the diffraction picture indicates the positions of the lens diaphragm used to take the picture in the dark field. In fact, it gives a picture of crystallites (bright particles with the correspondent orientation to two chosen reflections – crystallographic planes). For this reason, the size of crystallites can be precisely estimated from the picture in the dark field. In this case it is 13 nm ± 3 nm.

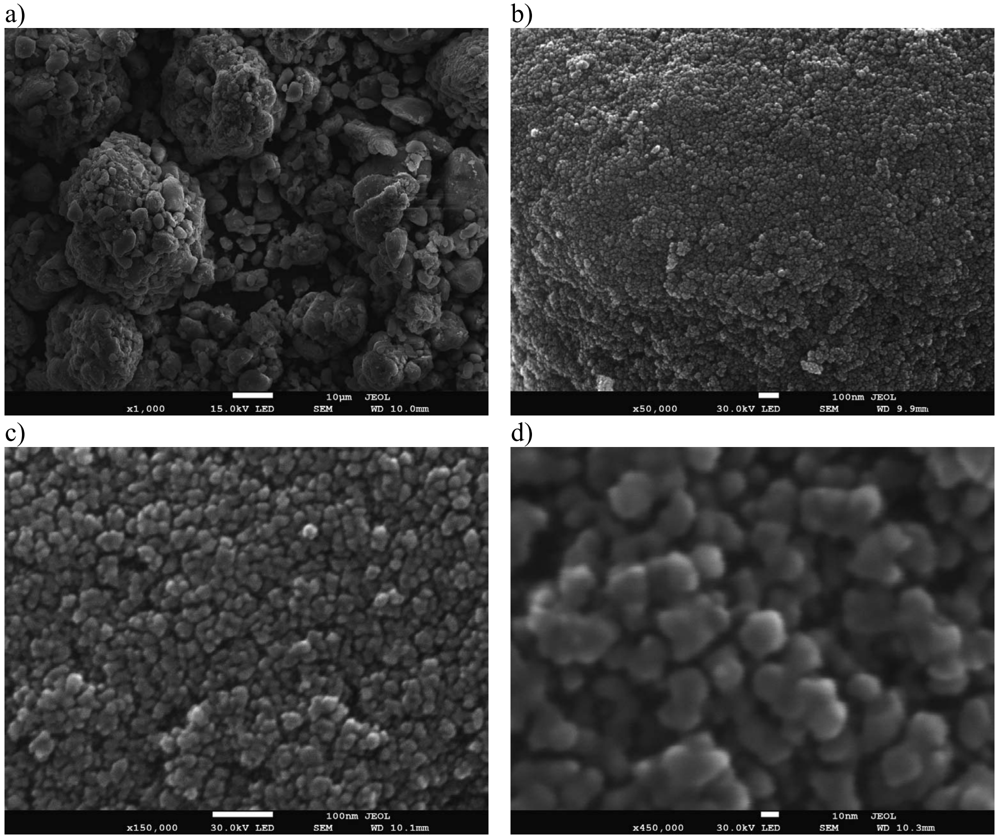

FIG. 8.20. Morphology of Fe_3O_4 Nanox grains: a) magnified 1000x, b) magnified 50000x, c) magnified 150000x, d) magnified 450000x.

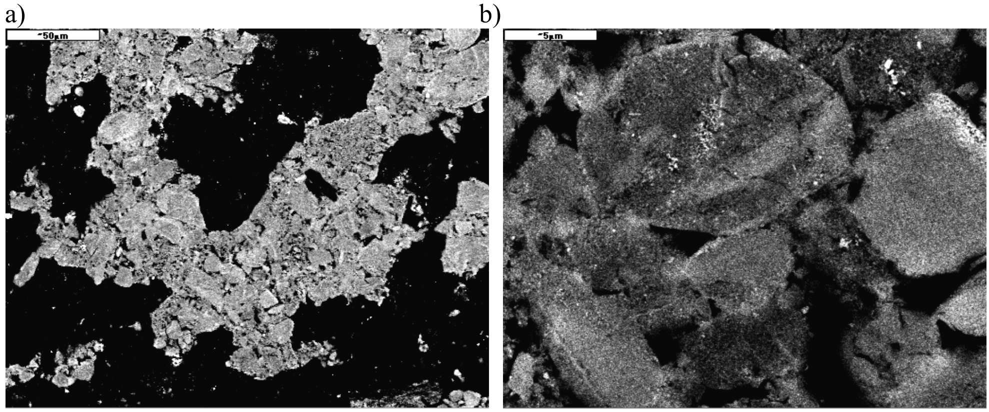

FIG. 8.21. Morphology of the cross section of Fe_3O_4 Nanox powder grains: a) magnified 500x, b) magnified 5000x.

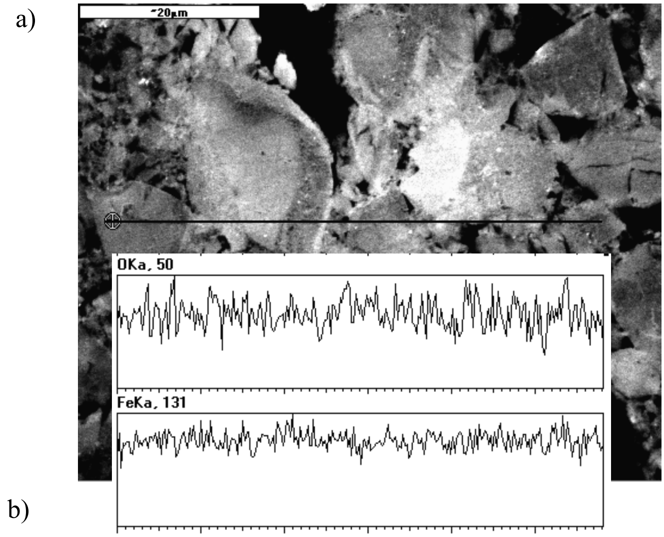

Fig. 8.22. Morphology of the cross section of a Fe_3O_4 Nanox powder grain: a) magnified 2000x, b) linear analysis.

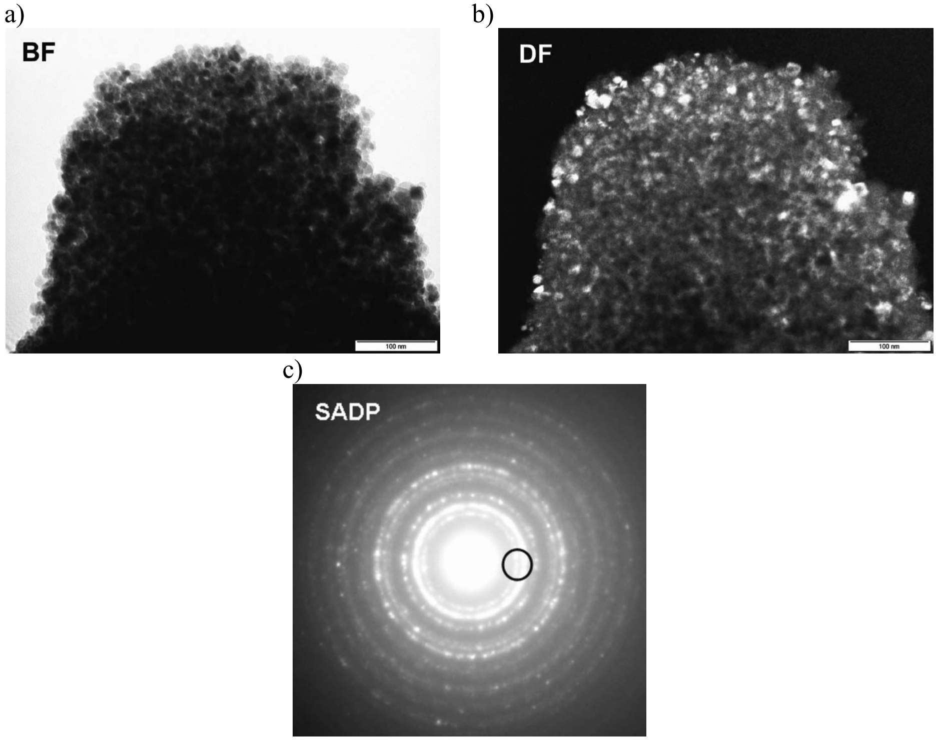

Fig. 8.23. The picture of microstructure of Fe_3O_4 powder: a) in the bright field (BF), b) in the dark field (DF), c) electron diffraction (SADP).

The crystallographic structure of powder was determined on the basis of electron diffraction. Five most intense diffraction rings were used to conduct the analysis (Fig. 8.24). Interplane distances are given in Table 8.1 calculated on the basis of diffraction picture and theoretical for iron oxide (Fe_3O_4) with face-centred cubic and lattice parameter a = 8.3958 Å. It can be seen that the values measured with utmost precision correspond to the theoretical ones, which proves the existence of the Fe_3O_4 phase with the above-mentioned crystallographic structure.

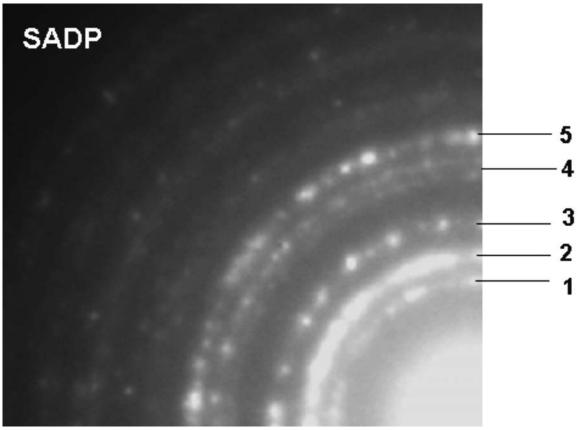

FIG. 8.24. Picture of electron diffraction (SADP) of Fe_3O_4 powder particle: 1-5 – the most intense diffraction rings.

TABLE 8.1. Calculated and theoretical values of interplane distances for Fe_3O_4 with the RSC structure.

d_{hkl} – computational, Å	d_{hkl} – theoretical, Å	*hkl*
3.066	2.968	220
2.597	2.531	311
2.153	2.099	400
1.666	1.616	333
1.527	1.484	440

Figure 8.25a shows the picture of microstructure of Fe_3O_4 particle powder in the bright field and a relevant HAADF picture (Fig. 8.25b), in which contrast is “sensitive” to both atomic mass of elements and thickness of the preparation. Dark areas correspond to lighter elements. Figure 8.25c presents a model spectrum of radiation, typical of the one analysed in point 2, proving the occurrence of iron oxide.

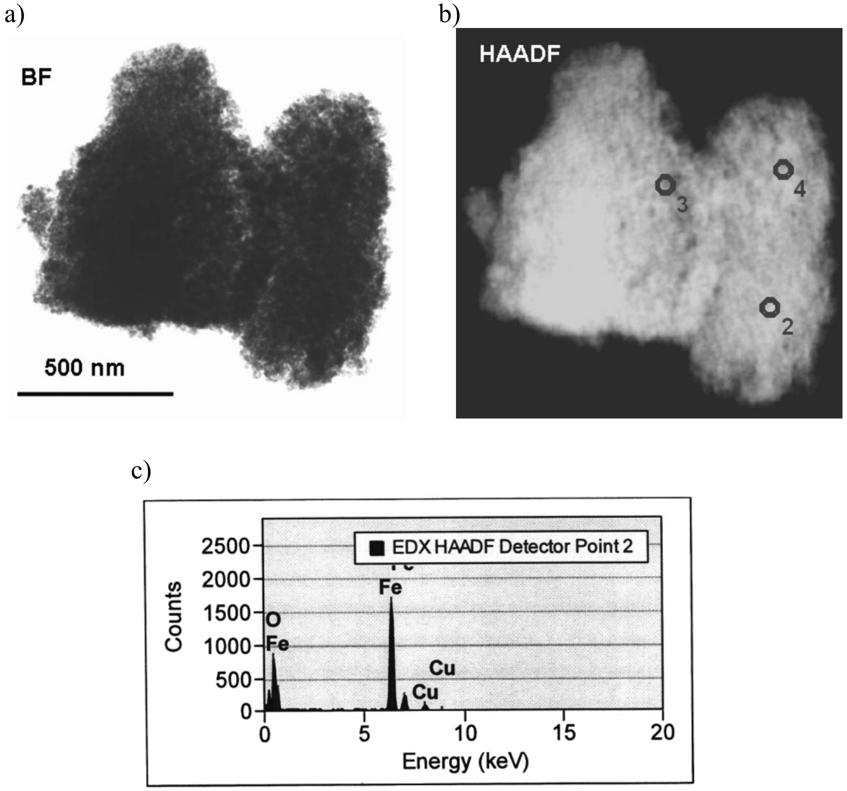

Fig. 8.25. Microstructure of Fe_3O_4 powder particle: a) in the bright field (BF), b) HAADF picture, c) the result of EDX analysis in point 2.

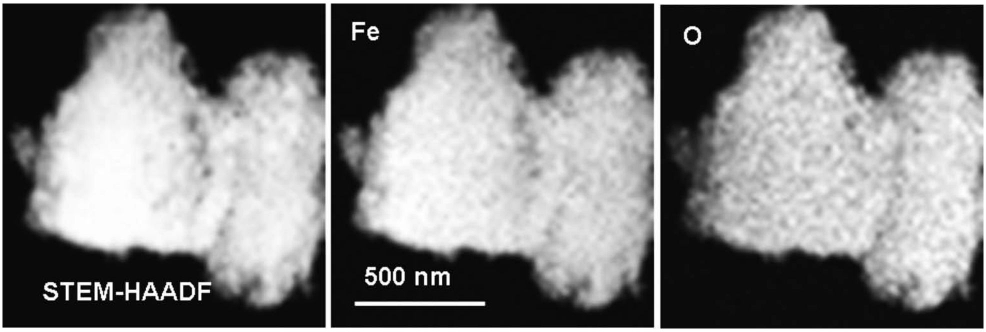

Fig. 8.26. The picture of microstructure of Fe_3O_4 powder particle obtained by scanning with an electron beam in the HAADF operating mode.

The picture of microstructure of powder particles is obtained by scanning them with an electron beam in the HAADF operating mode, in which contrast is “sensitive” to atomic mass of elements enabling to obtain a map of their decomposition, is shown in Figure 8.26. In the pictures on the right it is visible that particles have high chemical homogeneity, which is proved by signal homogeneity (the intensity of the greyness level) both for iron and oxygen. Insignificant differences in brightness occurring in the pictures indicate a different thickness of the particles (induced stronger signal). Occurrence of any other elements was not confirmed.

8.3. Phase Composition of the Powders

Examination of phase composition was carried out with the use of the diffractometers D500 and D8 Advance of the Bruker Company with Co-Kα radiation of wavelength λ = 1.78897 Å. Measurements were carried out for all four applied powders. Analysis of WC-12Co Amperit and WC-12Co Nanox showed that they are composed of WC and Co and they do not have any other phases (Fig. 8.27).

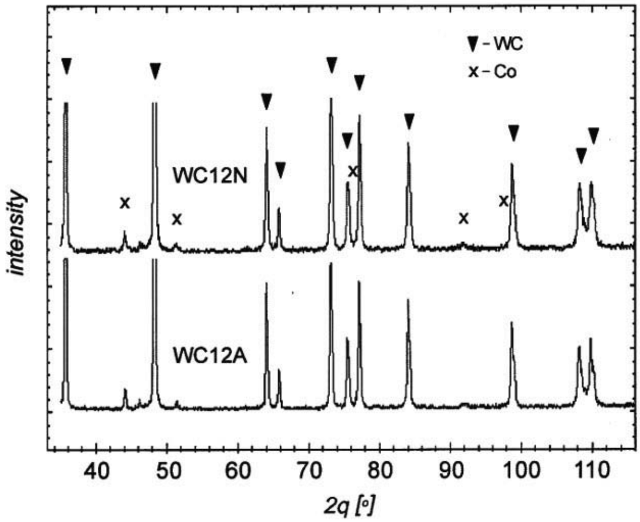

FIG. 8.27. Diffractograms of WC-12Co Amperit (WC12A) and WC-12Co Nanox (WC12N) powders made according to the Bregg-Brentano geometry. The positions of lines from the identified phases are highlighted in the picture.

Analysis of Fe_3O_4Inflox and Fe_3O_4 Nanox indicated that they do not have any impurities and are composed merely of pure magnetite (Fig. 8.28).

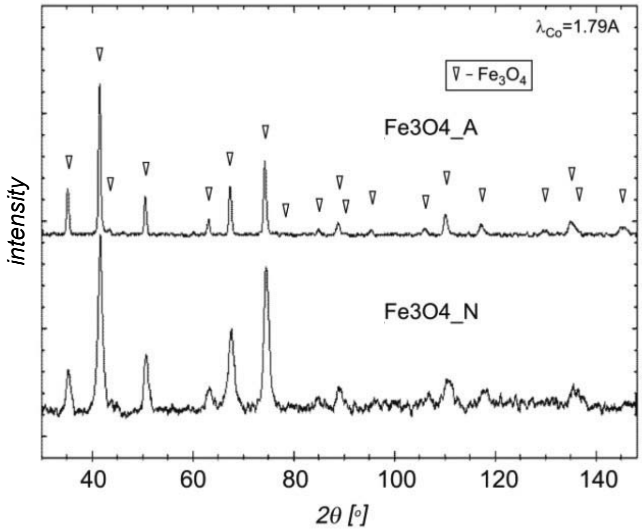

FIG. 8.28. Diffractograms of Fe_3O_4Inflox (Fe3O4_A) and Fe_3O_4 Nanox (Fe3O4_N) powders according to the Bregg-Brentano geometry. The positions of lines from the identified phases are highlighted in the picture.

Chapter 9

Microstructure and Chemical Composition of the Coatings

One of the elementary features of a coating is its microstructure which has a significant influence on physico-mechanical properties; therefore, its analysis is a key factor in quality assessment of the coating [71, 112].

Figure 9.1a and b show the microstructure of the supersonically sprayed WC-12Co Amperit coating. The pores with diversified shape and size occurring in the structure of the coating are observable. Their presence results from incomplete filling of the substrate by the particle hitting it. It is an intrinsic feature of all thermally sprayed coatings. Tungsten carbides constitute the bright phase on the sprayed coating. Its diversely-shaped grains embedded in the cobalt matrix are noticeable (Fig. 9.1b). Linear analysis (Fig. 9.1b) illustrates an uneven distribution of elements, which is a result of composite-like structure of the WC-12Co coating. The analysis of the element contents in the coating enables identifying the presence of pores in the coating structure, which, without a thorough analysis of its structure, can be classified as a different phase occurring in the coating. In the areas of pore occurrence, there is a substantially lower level of cobalt and tungsten. The noticeable substantial decrease in tungsten counts together with an increase in cobalt counts proves the occurrence of cobalt not a pore in that particular place. The qualitative analysis (Fig. 9.3) illustrates the distribution of elements in the coating.

Figure 9.4a and b present the microstructure of the supersonically sprayed WC-12Co Nanox coating. The difference in the shape of tungsten carbide grains is visible in both types if the coating, i.e. the nanostructural and conventional one. The coating sprayed with powder with a nanostructural composition has a fine-grained structure to a larger extent, in which nanocrystals are retained. It also exhibits a lower level of porosity despite the fact that nanostructural powder has a higher percentage of grains with a higher level of granulation. One of the reasons of increased porosity of the coating sprayed with conventional powder is greater porosity in the microsections of its grains than in the case of nanocrystal powder. The linear analysis of the coating bears resemblance to the one of the WC-12Co Amperit coating (Figs. 9.5a and 9.5b). In the place of increased tungsten counts, there is a decrease in cobalt counts. The distribution of elements in the coating (Fig. 9.6) shows a denser and more even distribution of elements than in the case of the WC-12Co Amperit coating (Fig. 9.3), which proves much smaller size of tungsten carbide grains in the sprayed coating.

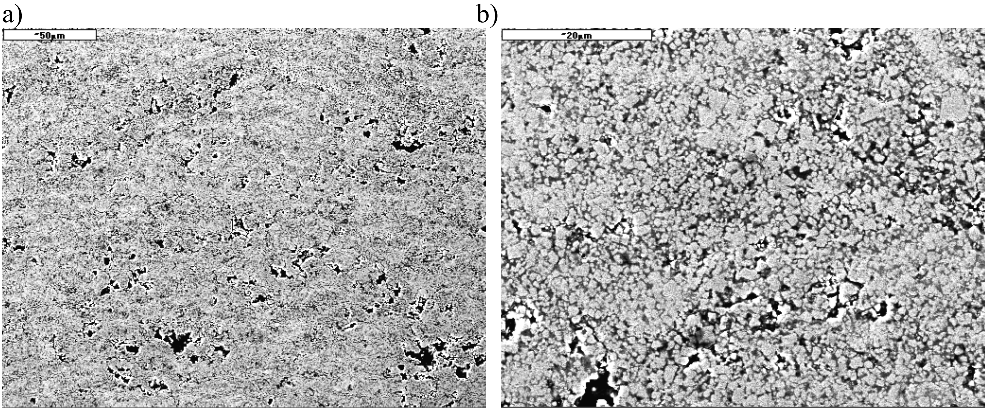

FIG. 9.1. Microstructure of supersonic sprayed WC-12Co Amperit coating: a) magnified 500x, b) magnified 2000x.

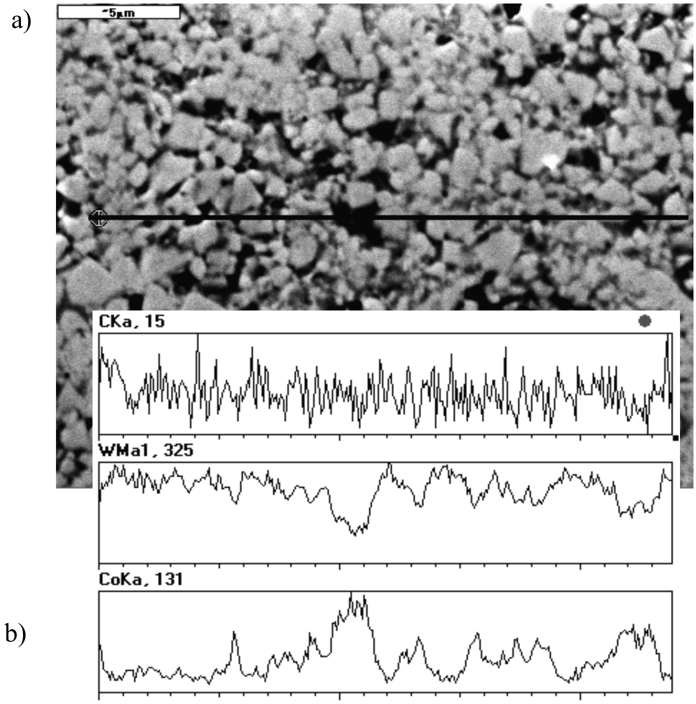

FIG. 9.2. Microstructure of supersonic sprayed WC-12Co Amperit coating: a) magnified 5000x, b) linear analysis.

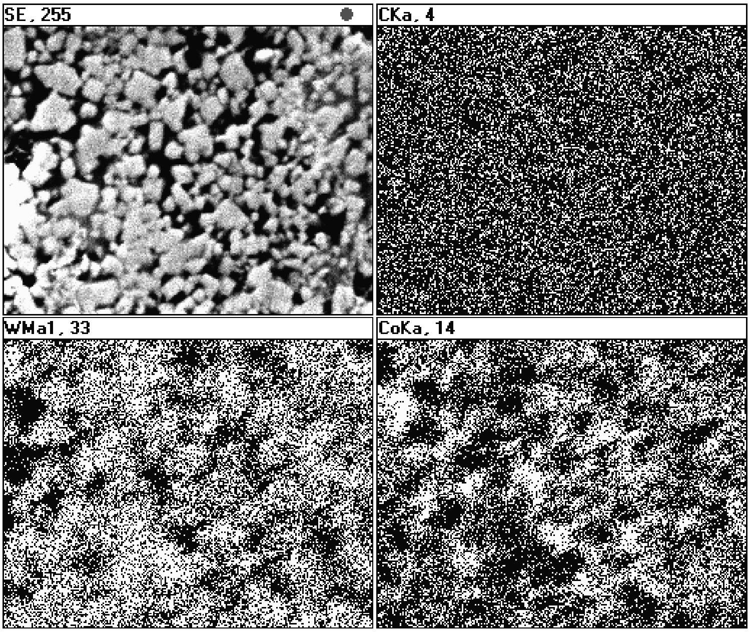

Fig. 9.3. The qualitative analysis of supersonic sprayed WC-12Co Amperit coating (magnified 5000x).

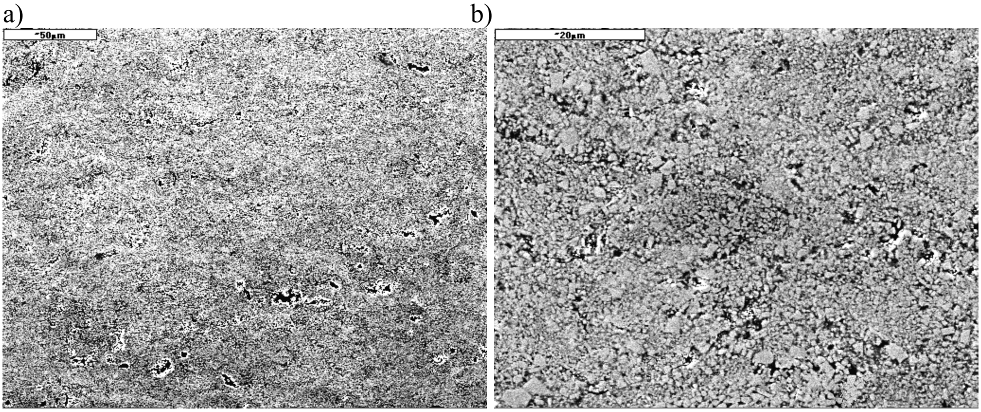

Fig. 9.4. Microstructure of supersonic sprayed WC-12Co Nanox coating: a) magnified 500x, b) magnified 2000x.

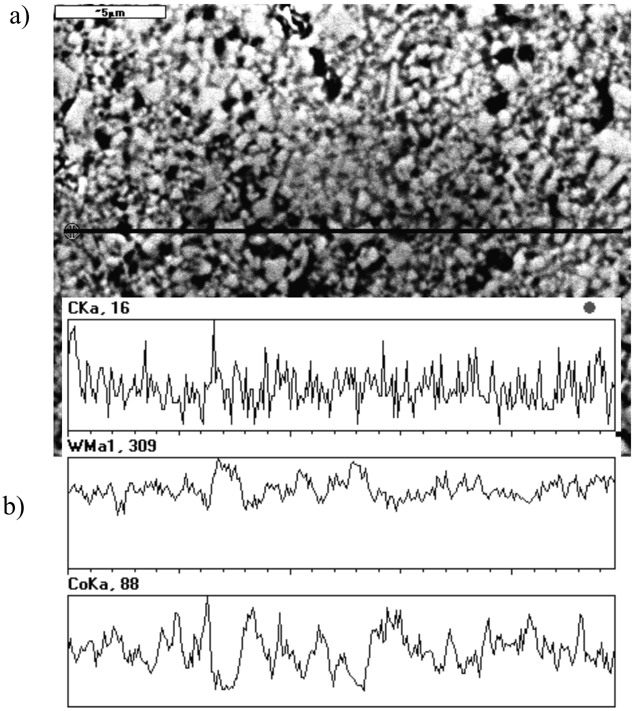

FIG. 9.5. Microstructure of supersonic sprayed WC-12Co Nanox coating: a) magnified 5000x, b) linear analysis.

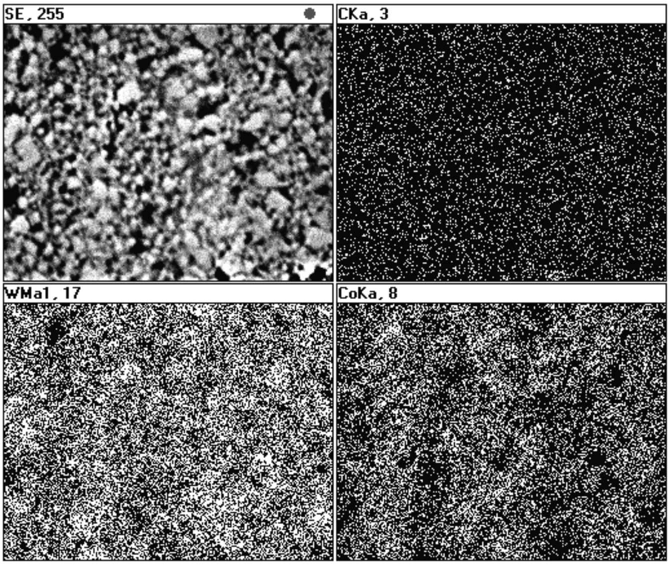

FIG. 9.6. The qualitative analysis of supersonic sprayed WC-12Co Nanox coating (magnified 5000x).

Both the microstructure of two WC grains in the WC-12CoNanox coating in the bright field and diffraction correspondent to them are shown in Figure 9.7. The grains are surrounded by an amorphous cobalt warp. The size of grains ranges from 200 to 500 nm. The selected area diffraction pattern is correspondent to the hexagonal structure of WC with [102]. Microstructures in the bright field and their correspondent electron diffractions from the areas with grains of different content of Co are presented in Figure 9.8. In the area of an increased content of Co, there is a completely amorphous structure, whereas crystal grains have a hexagonal structure of WC.

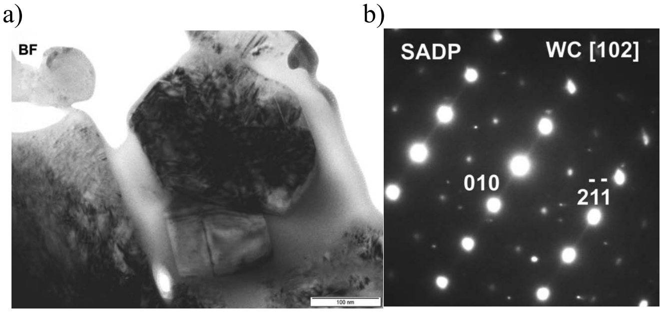

FIG. 9.7. Microstructure of supersonic sprayed WC-12Co Nanox coatings: a) WC grains, b) electron diffraction (SADP).

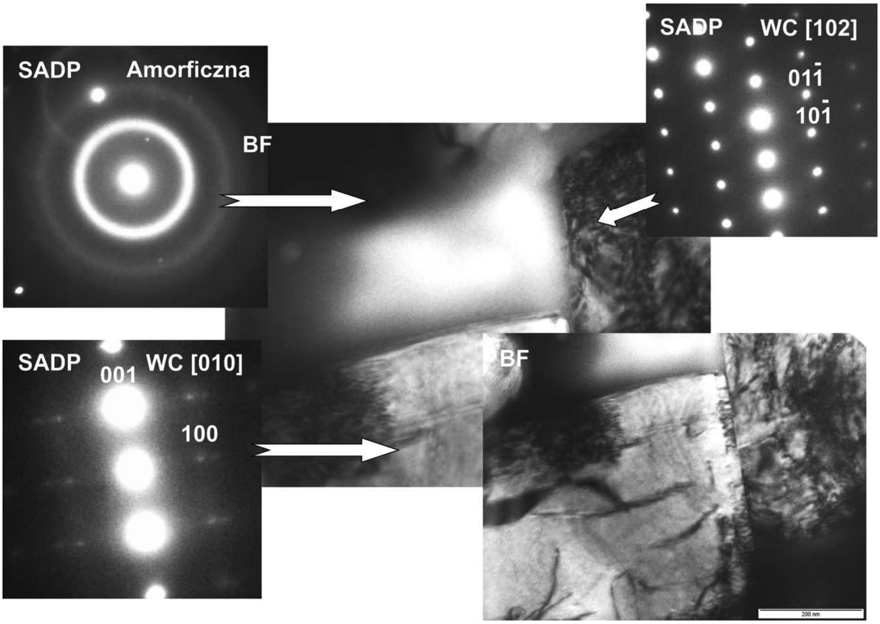

FIG. 9.8. Crystal grains of tungsten carbides and amorphous cobalt structure in supersonic sprayed microstructure of WC-12Co Nanox coating in the bright field (BF) and connected electron diffractions.

The microstructure of the WC-12CoNanox coating in the bright field and its correspondent HAADF picture are shown in Figures 9.9a and 9.9b. Sample spectra of the EDS analysis (Fig. 9.9, points 1, 2, 3 and 4) confirm the presence of tungsten carbide and varied contents of Co (Fig. 9.9c). The results of chemical analysis showing the differences in the construction of particular grains have been collated in Table 9.1.

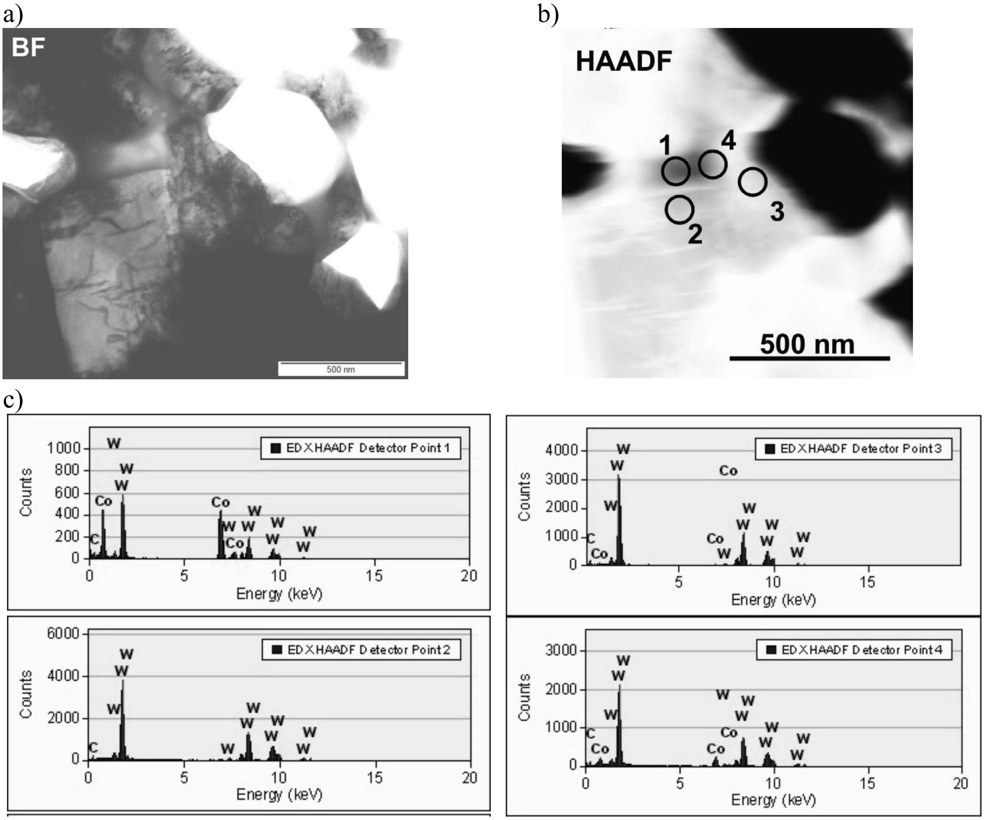

FIG. 9.9. Supersonic sprayed WC-12Co Nanox coating: a) microstructure in the bright field (BF), b) HAADF picture of microstructure, c) results of EDX analysis.

TABLE 9.1. Results of chemical analysis of supersonic sprayed WC-12Co Nanox coating.

Point	% at.		
	W	C	Co
1	31.3	13.2	55.5
2	52.6	47.1	0.3
3	50.1	49.9	1.0
4	49.6	40.3	11.1

Figures 9.10a and 9.10b also illustrate the microstructure of the WC-12CoNanox coating in the bright field and its correspondent HAADF picture of the selected fragment of the coating with a visible round grain, being 20 nm in size, inside a larger equiaxed grain embedded in an amorphous matrix. Analysis the smaller grain led to a conclusion that it is TiN. Sample spectra of the EDS analysis (Fig. 9.10b, points 1, 2, 3 and 4) confirm the presence of tungsten carbide and varied contents of Co and the grain of titanium nitride (Fig. 9.9c).

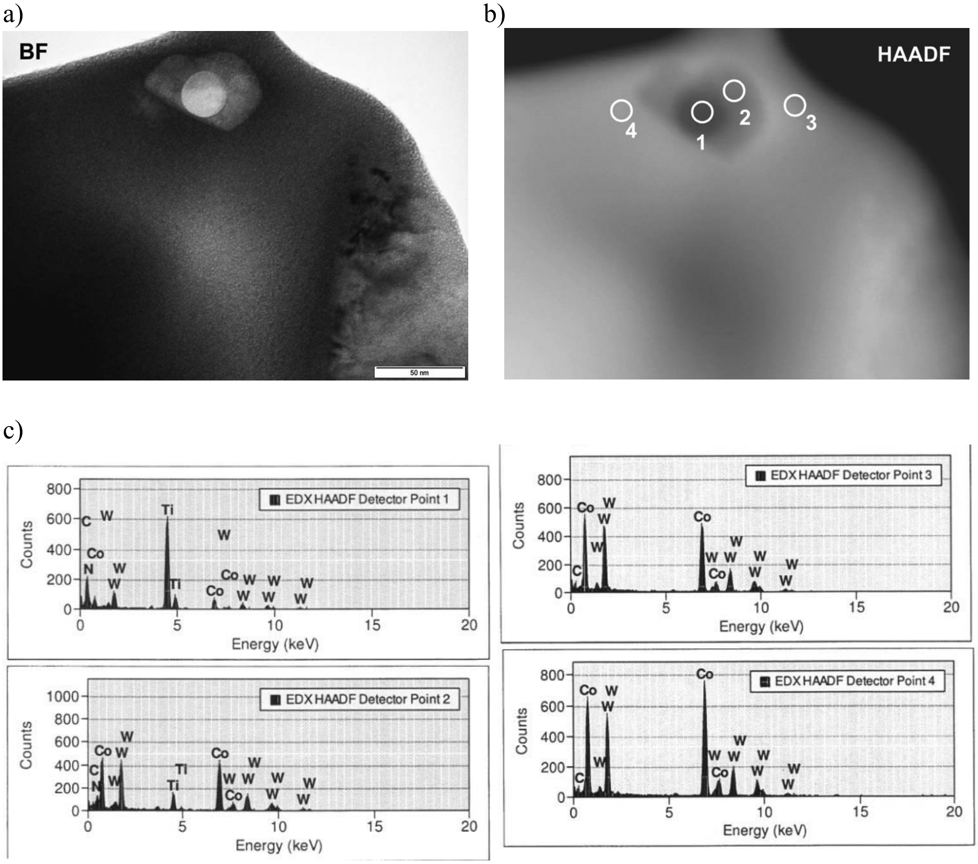

FIG. 9.10. Supersonic sprayed WC-12Co Nanox coating: a) microstructure in the bright field (BF), b) HAADF picture of microstructure, c) results of EDX analysis.

Figures 9.11a,b,c and d illustrates the microstructure of the WC-12CoNanox coating in the bright field in varied magnifications of the selected areas of the coating. There are all visible types of grains: crystal, amorphous, and circular.

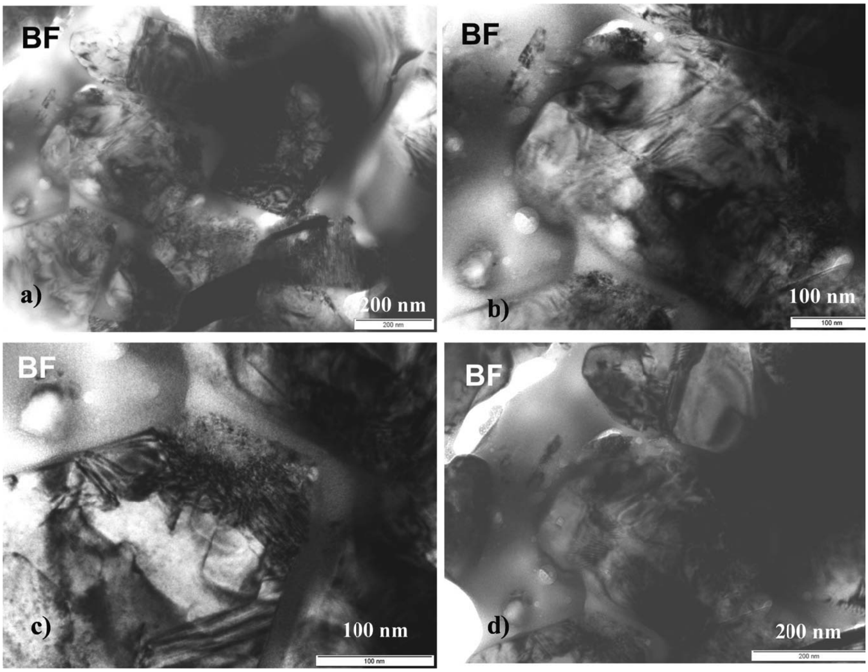

FIG. 9.11. Microstructure of supersonic sprayed WC-12Co Nanox coating in the bright field (BF) with different magnification.

The conclusion to be drawn from the analysis of the microstructure of the WC-12Co Nanox coating (Figs. 9.7–9.11) is that nanocrystal grains of tungsten carbide, which were present in the sprayed powder, have been retained. It proves the fact that during supersonic spraying at a relatively low temperature of the spray stream and short time of dwelling of powder grains in the spray stream does not cause their decomposition in spite of their tiny size. Considerable alteration in the phase composition of WC, which particularly occur during plasma spraying, lower operating properties of the coatings to a large extent. The influence of heat from the supersonic spray stream on the sprayed WC-12Co Nanox powder is noticeable in the case of cobalt which forms an amorphous structure surrounding nanocrystal grains of tungsten carbide.

Figures 9.12a, b and c show the microstructure of the supersonically sprayed Fe_3O_4 Inflox coating. The boundaries between the slightly distorted grains and pores are observable in the sprayed coating. Despite higher melting temperature of iron oxide and its utilization in plasma spraying, this oxide forms a solid coating also during supersonic spraying. Equal occurrence of oxygen and iron in the sprayed coating is noticeable on the map of element distribution (qualitative distribution) in Figure 9.13. There is not diffusive connection between the coating and the aluminium substrate according to the linear analysis of the substrate-coating adhesion area (Figs. 9.14a and 9.14b).

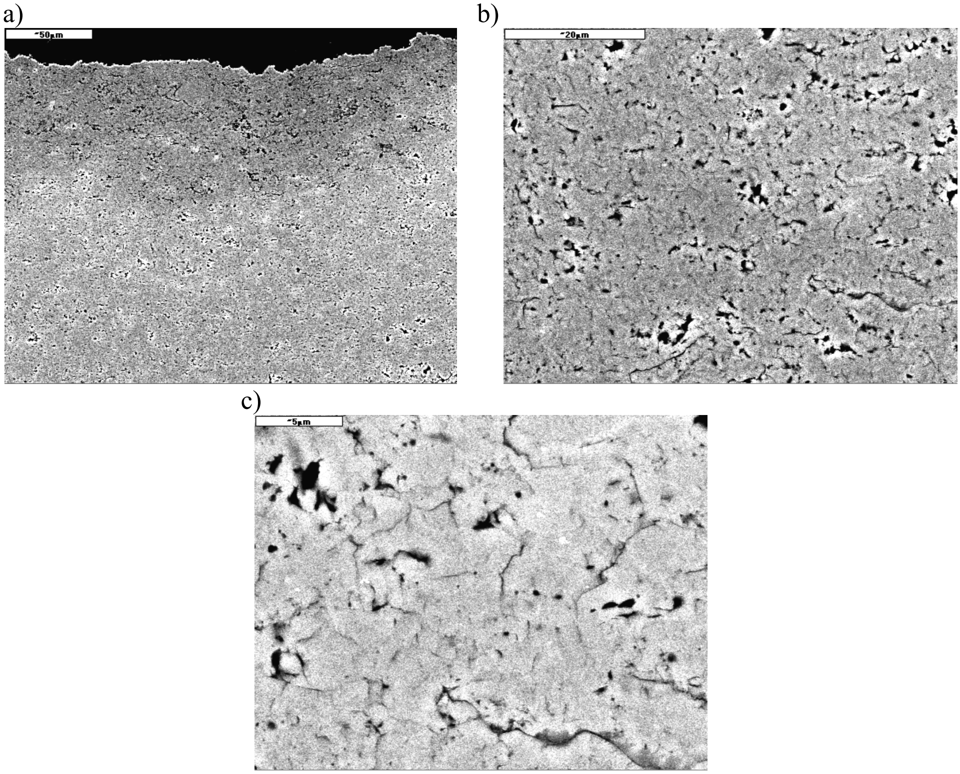

Fig. 9.12. Microstructure of supersonic sprayed Fe_3O_4 Inflox coating: a) magnified 500x, b) magnified 2000x, c) magnified 5000x.

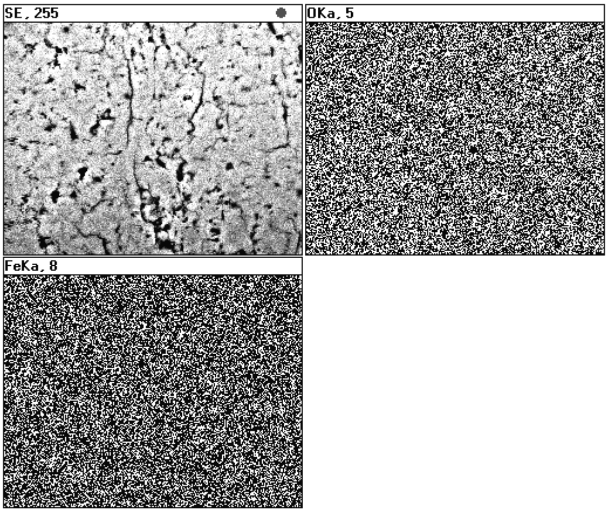

Fig. 9.13. The qualitative analysis of supersonic sprayed Fe_3O_4 Inflox coating (magnified 5000x).

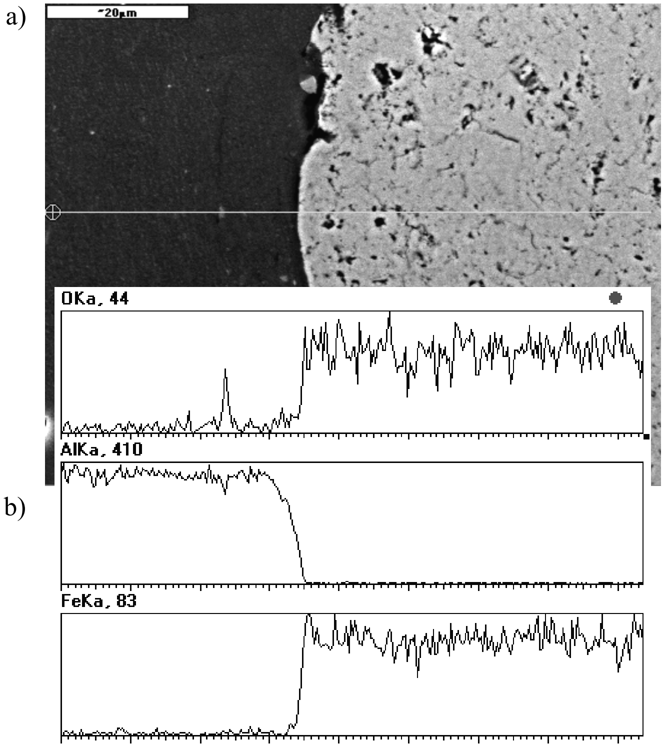

FIG. 9.14. Microstructure of supersonic sprayed Fe_3O_4 Inflox coating: a) magnified 2000x, b) linear analysis.

Figures 9.15a and 9.15b present the microstructure of the supersonically sprayed Fe_3O_4 Nanox coating. Despite the differences in granulometric distribution of Fe_3O_4 Inflox and Fe_3O_4 Nanox powders, there are no distinct differences in the morphology of both coatings. As in the case of the Fe_3O_4 Inflox coating, one can observe clearly noticeable boundaries between slightly distorted powder grains as well as pores (Fig. 9.15c). On the basis of the linear analysis in the area of adhesion of the Fe_3O_4 Nanox coating to the substrate, it can be concluded that there is no diffusive connection between the Fe_3O_4 Nanox coating and the aluminium substrate, which was also the case with the Fe_3O_4 Inflox coating (Fig. 9.16).

Figure 9.17 shows equal occurrence of oxygen and iron in the Fe_3O_4 Nanox sprayed coating on the map of element distribution. A dark grain (400 nm in size, present in the spherical area with coarse grains and a distinct boundary between columnar grains much smaller in sizes) is visible in the picture showing the microstructure of the bright phase (Fig. 9.18a). Electron diffraction (Fig. 9.18b) from the dark field corresponds to Fe_3O_4 phase with axial orientation of the strip [411] with a considerable accuracy.

Figure 9.19a presents the microstructure of Fe_3O_4 Nanox coating with a boundary between the area of columnar nanograins and coarse equiaxed grains, whereas Figure 9.19b shows the picture of equiaxed grains. HAADF picture of the microstructure with a boundary between the area of columnar nanograins and coarse equiaxed grains is given in Figure 9.20a. Point chemical analyses of the area (1, 2, 3, and 4) show the composition of Fe_3O_4 Nanox coating (Fig. 9.20b). In all cases there is present Fe_3O_4 and lack of a signal from aluminium.

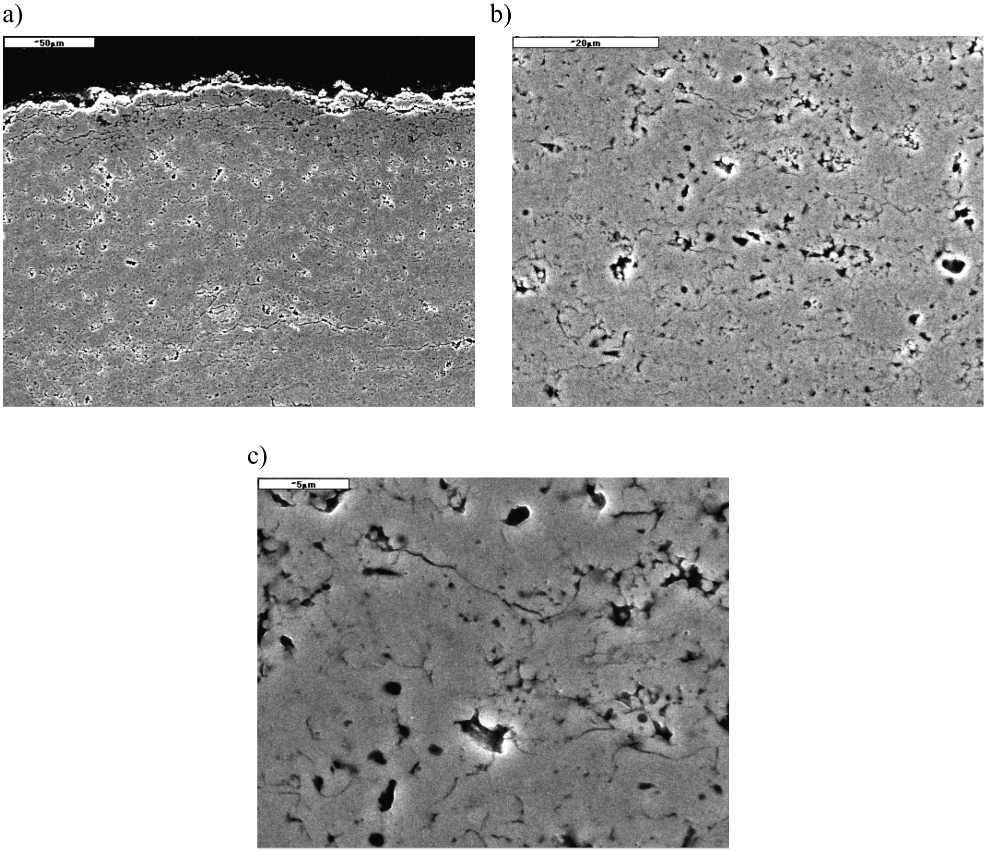

Fig. 9.15. Microstructure of supersonic sprayed Fe_3O_4 Nanox coating: a) magnified 500x, b) magnified 2000x, c) magnified 5000x.

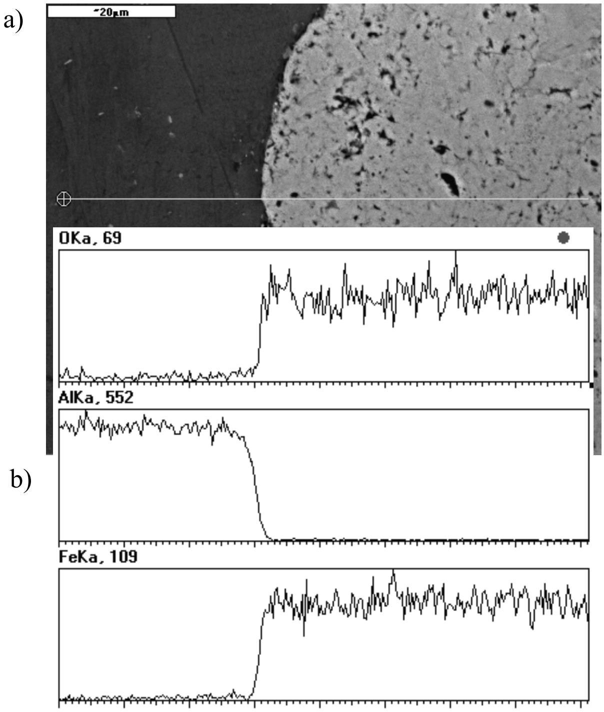

FIG. 9.16. Microstructure of supersonic sprayed Fe_3O_4 Nanox coating: a) magnified 5000x, b) linear analysis.

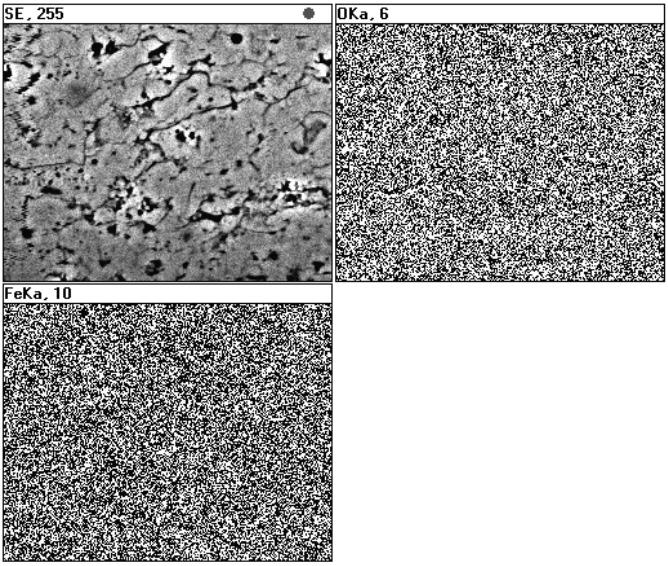

FIG. 9.17. The qualitative analysis of supersonic sprayed Fe_3O_4 Nanox coating (magnified 5000x).

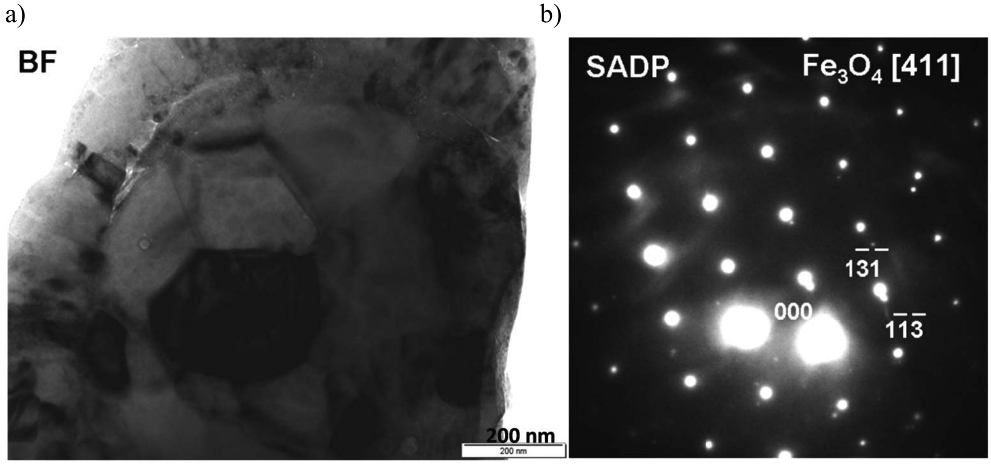

FIG. 9.18. Particles of supersonic sprayed Fe_3O_4 Nanox coating: a) microstructure in the bright field (BF), b) electron diffraction (SADP).

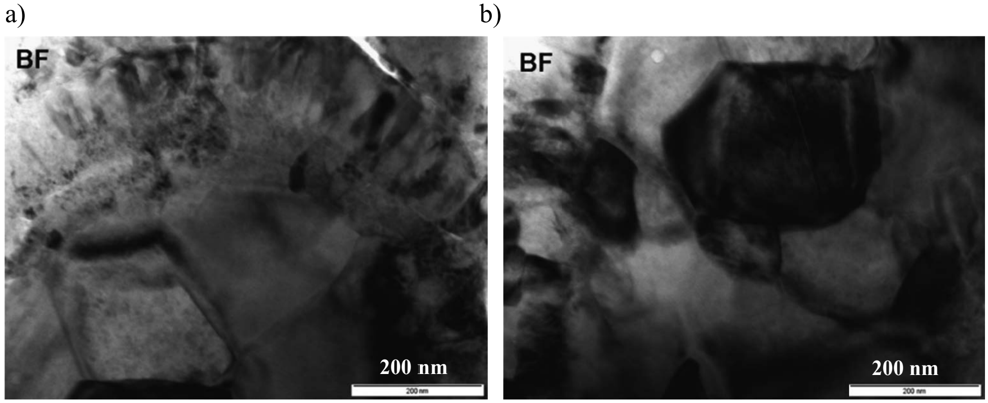

FIG. 9.19. Nanograins of supersonic sprayed Fe_3O_4 Nanox coating: a) column-shaped and uniaxial, b) uniaxial.

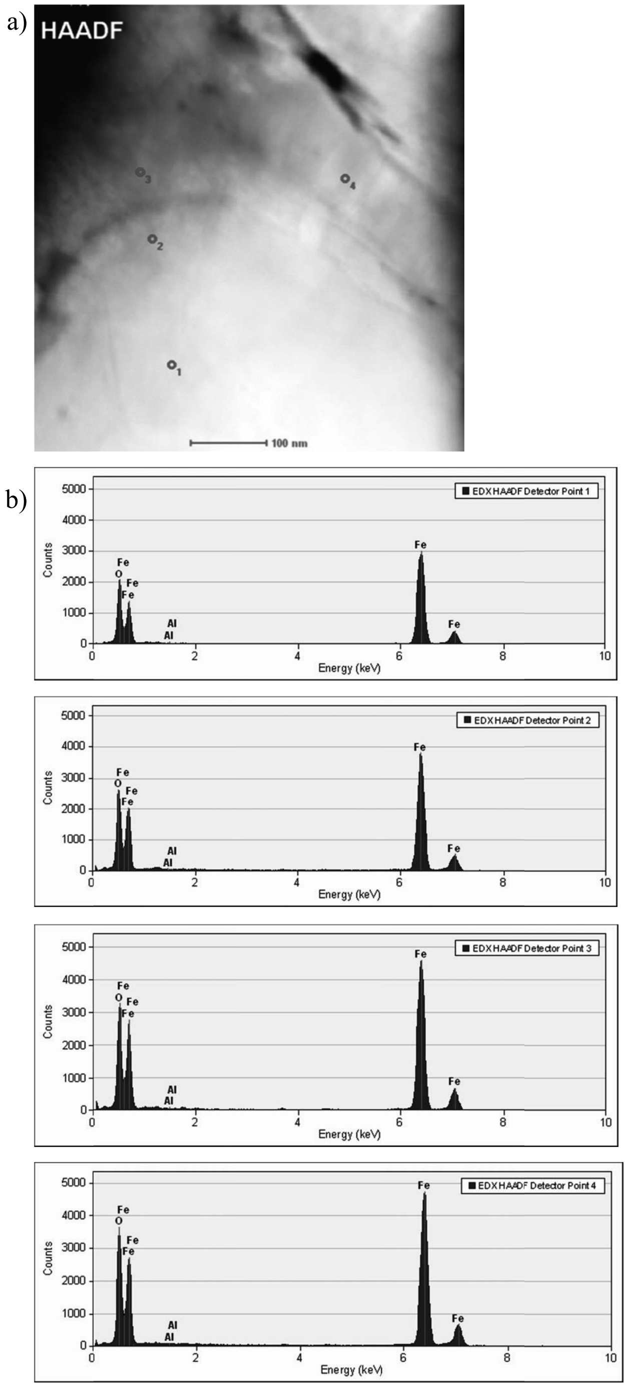

FIG. 9.20. Particle of supersonic sprayed Fe_3O_4 Nanox coating: a) HAADF picture, b) EDX analysis.

One can observe the microstructure of the coating in the bright and dark fields in Figures 9.21a and 9.21b, whilst in Figure 9.21c – their correspondent electron diffraction with the largest diffraction diaphragm (200 μm), i.e. from almost whole area of the picture. Grains which are less than 100 nm in size are visible as well. The diffraction corresponds to Fe_3O_4 phase and is identical to the one obtained in the sprayed powder. Figures 9.22a and 9.22b illustrate microstructures in the bright field from boundary areas; typical large-in-size equiaxed grains are seen as well. Figure 9.23c presents the microstructure of Fe_3O_4 Nanox coating in the dark and bright fields (Figs. 9.23a and 9.23b), and the correspondent electron diffraction conducted with the largest diffraction diaphragm (200 μm), i.e. from almost whole area of the picture. Columnar grains, less than 50 nm in width, can be seen as well. The obtained diffraction corresponds to Fe_3O_4 phase and is exactly the same as the diffraction of sprayed powders.

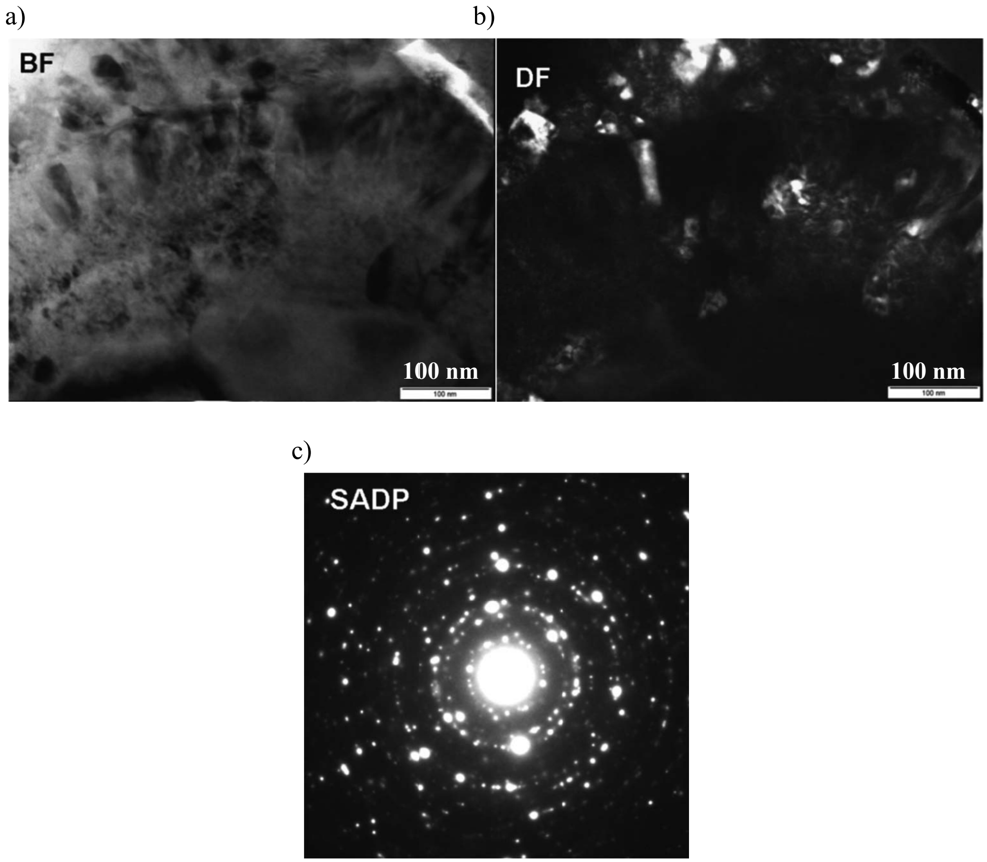

FIG. 9.21. Supersonic sprayed Fe_3O_4 Nanox coating: a) microstructure in the bright field (BF), b) microstructure in the dark field (DF), c) electron diffraction (SADP).

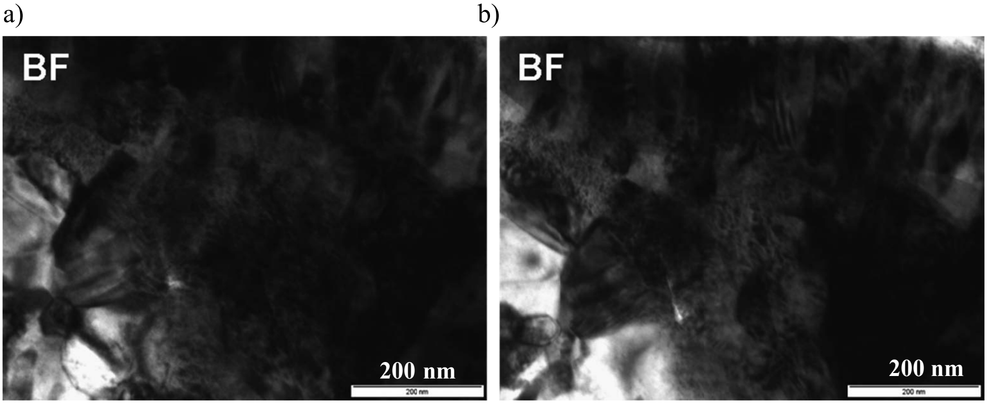

FIG. 9.22. Microstructure of supersonic sprayed Fe_3O_4 Nanox coating in bright fiels (BF): a), b) column-shaped and uniaxial nanograins.

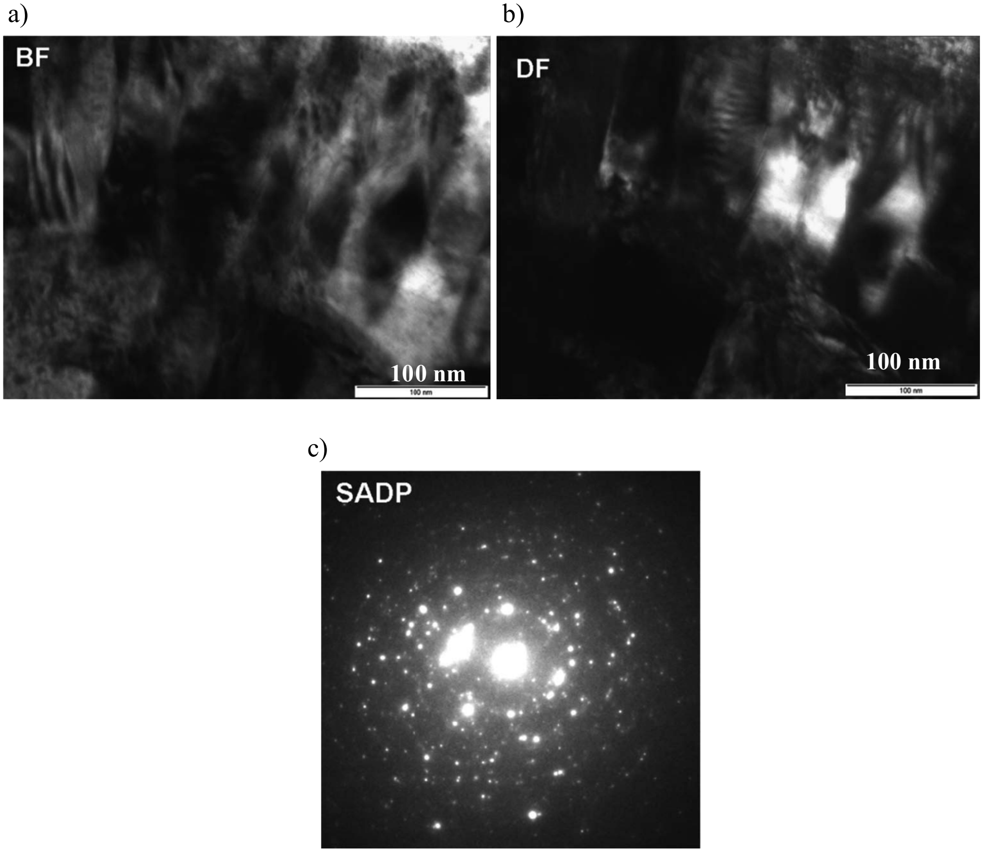

FIG. 9.23. Supersonic sprayed Fe_3O_4 Nanox coating: a) microstructure in the bright field (BF), b) microstructure in the dark field (DF), c) electron diffraction (SADP).

Figure 9.24a presents the microstructure in the bright field and the correspondent electron diffraction is shown in Figure 9.24b. Both the equiaxed grains being less than ca. 100 nm in manometric size as well as manometric columnar grains are clearly observable.

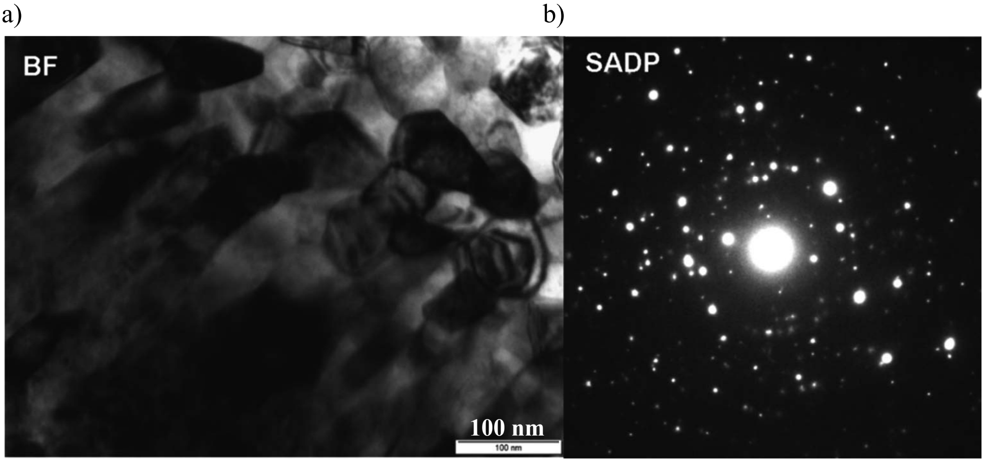

FIG. 9.24. Particles of supersonic sprayed Fe_3O_4 Nanox coating: a) microstructure in the bright field (BF), b) electron diffraction (SADP).

The microstructure of a gradient conventional coating is shown in Figures 9.25a and 9.25b. The areas of the dark phase, which is constituted with the sprayed Fe_3O_4 Inflox matrix, are distinctively visible.

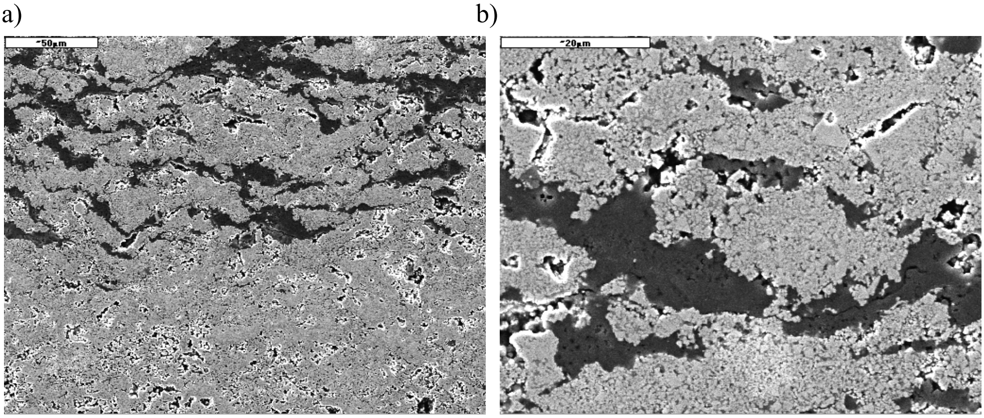

FIG. 9.25. Microstructure of supersonic sprayed WC-12Co/Fe_3O_4 conventional composite coating: a) magnified 500x, b) magnified 2000x.

The map of element distribution (Fig. 9.26) serves as a confirmation of this fact, where in the areas of iron and oxygen occurrence there is lack of tungsten. It can be noticed from the course of the linear analysis (Fig. 9.27b) that both the presence and the number of counts of iron and oxygen in the tested microstructure (Fig. 9.27a) coincide, which proves the presence of Fe_3O_4 in these areas. Simultaneously, the number of tungsten counts drops nearly to zero. The picture illustrating the microstructure of the gradient nanocomposite coating (Fig. 9.28) is very similar to the microstructure of the gradient conventional coating, granulations of the sprayed coatings in spite of the fact that their distributions are disparate. The map of element distribution (Fig. 9.29) shows that, like in the previous case, there is lack of oxygen and iron in the areas of tungsten occurrence. The linear analysis (Fig. 9.30b) of the researched microstructure (Fig. 9.30a) show the same changes in counts like in the case of the gradient conventional coating.

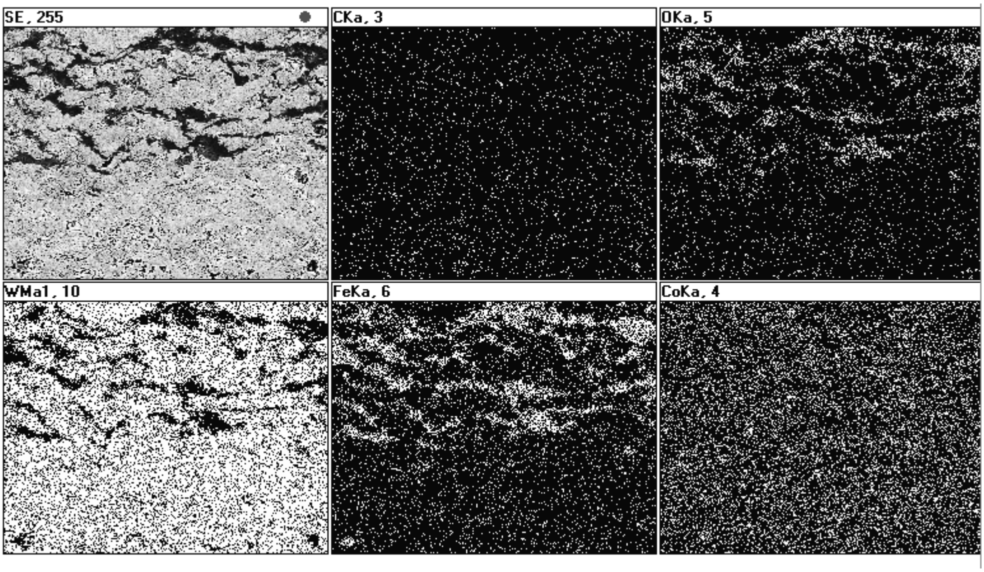

FIG. 9.26. The qualitative analysis of supersonic sprayed WC-12Co/Fe_3O_4 conventional composite coating (magnified 500x).

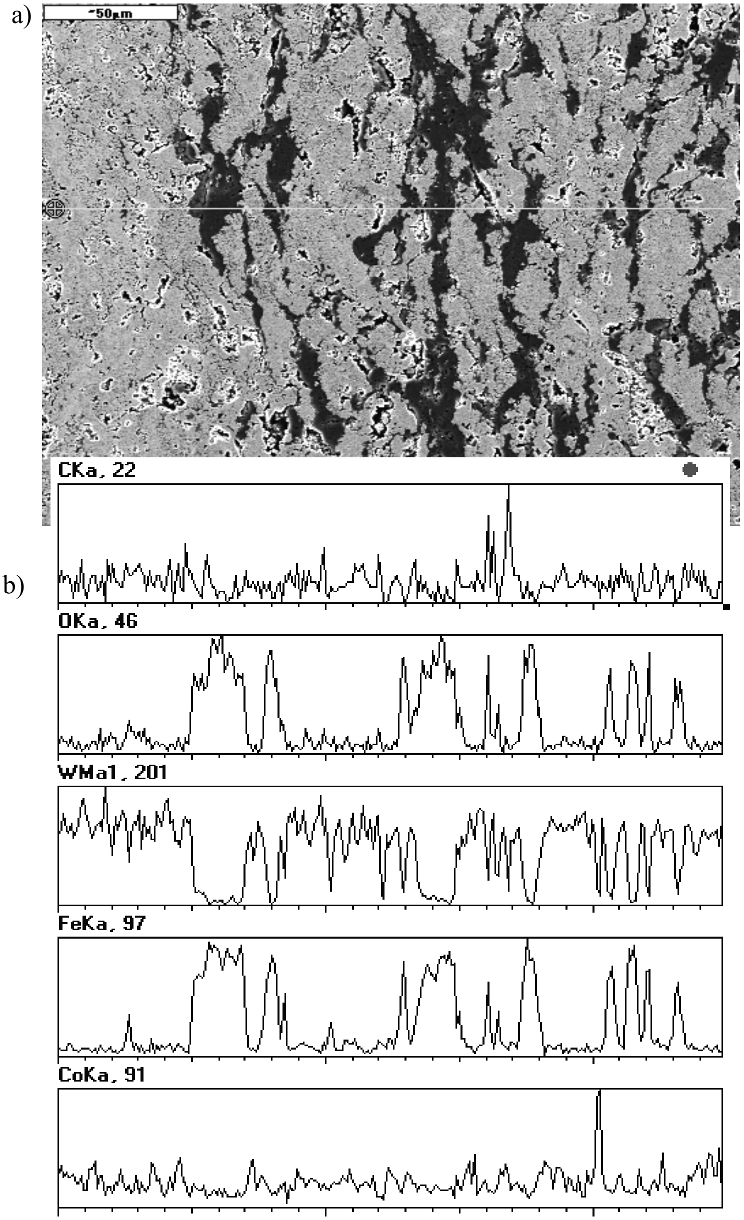

FIG. 9.27. Microstructure of supersonic sprayed WC-12Co/Fe_3O_4 conventional composite coating: a) magnified 500x, b) linear analysis.

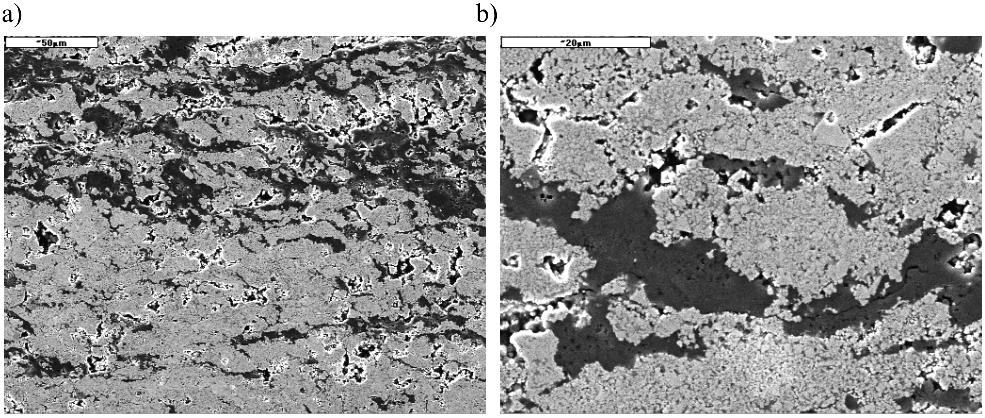

FIG. 9.28. Microstructure of supersonic sprayed WC-12Co/Fe_3O_4 nanostructured composite coating: a) magnified 500x, b) magnified 2000x.

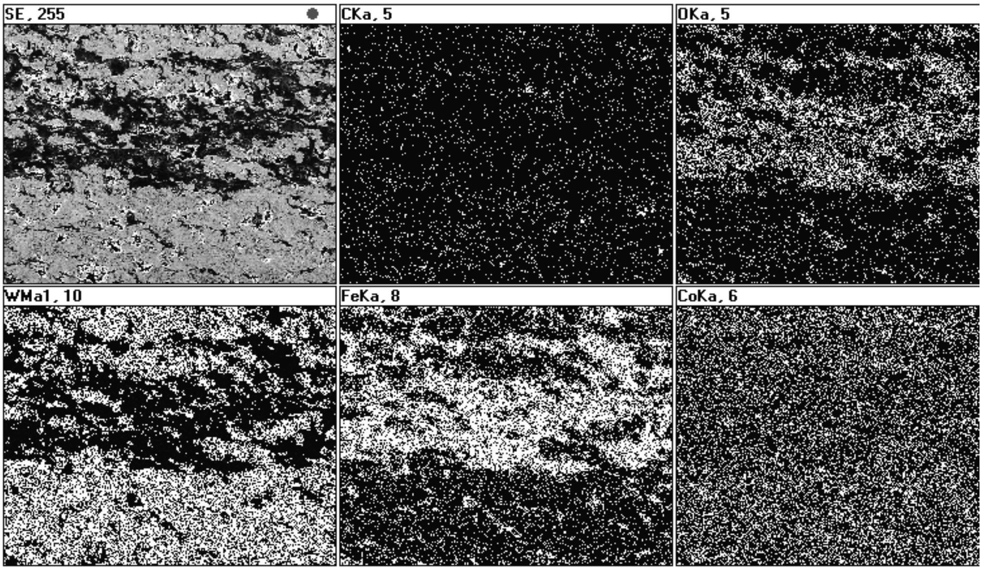

FIG. 9.29. The qualitative analysis of supersonic sprayed WC-12Co/Fe_3O_4 nanostructured composite coating (magnified 500x).

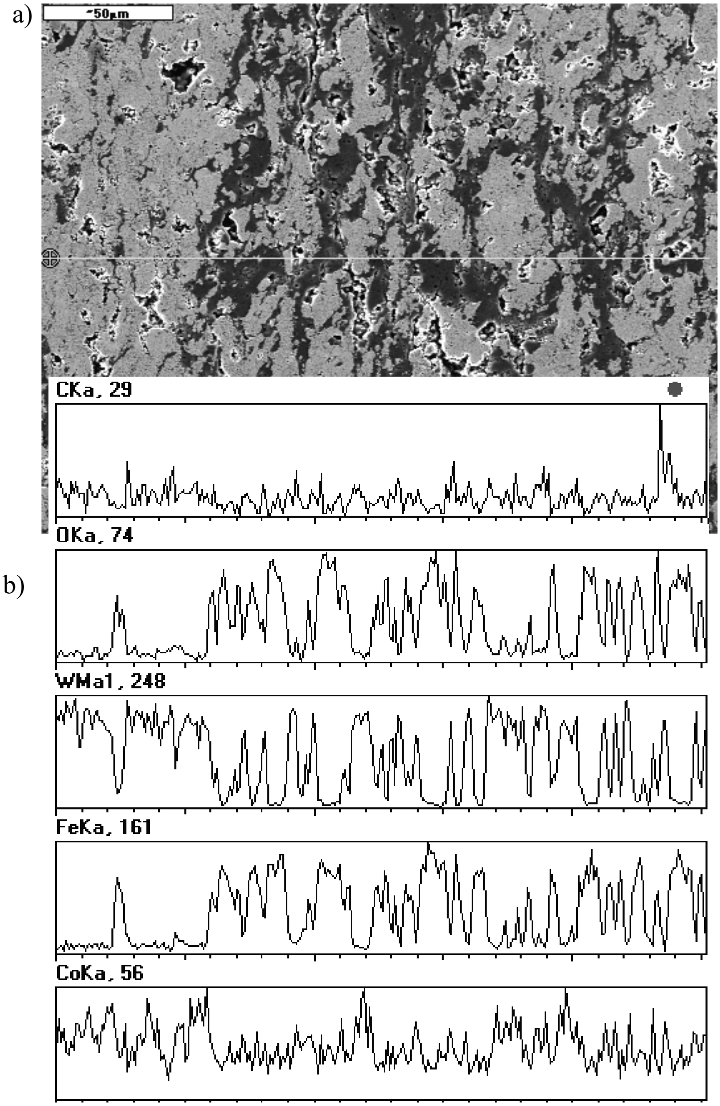

FIG. 9.30. Microstructure of supersonic sprayed WC-12Co/Fe_3O_4 nanostructured composite coating: a) magnified 500x, b) linear analysis.

Chapter 10

Phase Composition of the Coatings

Identifications of phases appearing in the obtained coatings were conducted in order to obtain a thorough analysis of the influence of supersonic spraying on the properties of coatings apart from investigating the microstructure and chemical composition. The study of chemical composition was conducted with Bruker D500 and D8 Advance diffractometers and filtered radiation of Cu and Co lamps. Measurements were done for each of the samples in one selected area on the external surface without initial preparations.

The analysis of WC-12Co Amperit (Fig. 10.1) and WC-12Co Nanox (Fig. 10.2) coatings showed only the presence of the WC phase; Co or, possibly, other phases obtained as a result of tungsten carbide decomposition do not occur. These phases are noticeable in the case of samples of coatings sprayed with the JP5000 system. Analysis of WC-12Co Amperit (Fig. 10.3) and WC-12Co Nanox (Fig. 10.4) coatings proved the presence of WC and Co, which were also present in both WC-12Co powders as well as in new phases, namely: W_2C, WC_{1-x} and W, which result from decomposing WC, which, in turn, is a consequence of the spraying stream affecting powder grains. A diffractometric analysis of Fe_3O_4 Inflox (Fig. 10.5) and Fe_3O_4 Nanox (Fig. 10.6) sprayed coatings showed that the sprayed coatings were not subject to any phase alterations, did not have any additional pollutants and are composed only of pure magnetite. Sprayed gradient coatings from mixtures of conventional and nanostructural powders were also investigated (Figs. 10.7 and 10.8). In the first case there is lack of Co or Fe_3O_4 as well as other phases. In the second phase only Fe_3O_4 is present. The diffractograms in Figure 10.9 and Figure 9.10 refer to the coatings sprayed with a mixture of conventional and nanostructural powders. In both cases, apart from WC, no other phases are present.

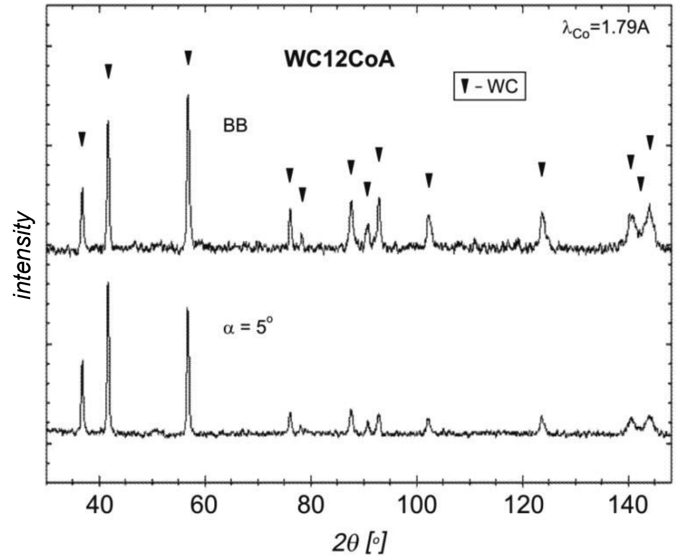

FIG. 10.1. Diffractograms of WC-12Co Amperit(WC-12CoA) coating made according to the Bragg-Brentano geometry. The picture shows marked positions of the lines of identified phases.

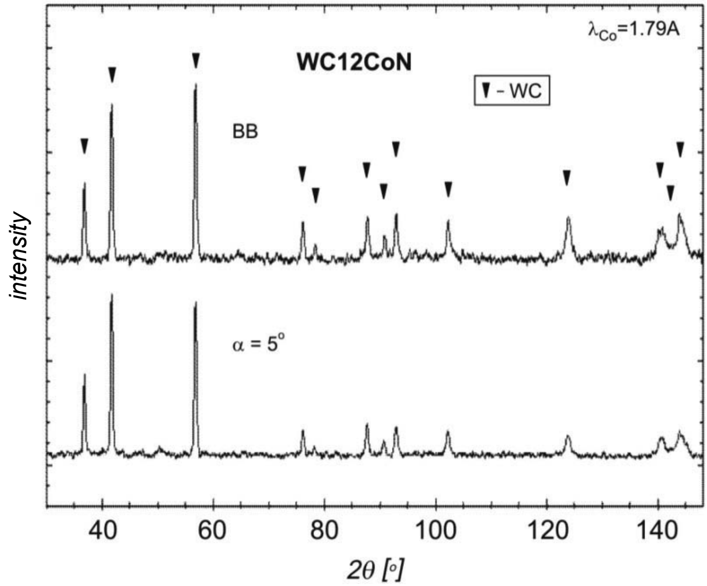

FIG. 10.2. Diffractograms of WC-12Co Nanox (WC-12CoN) coating made according to the Bragg-Brentano geometry. The picture presents marked positions of the lines of identified phases.

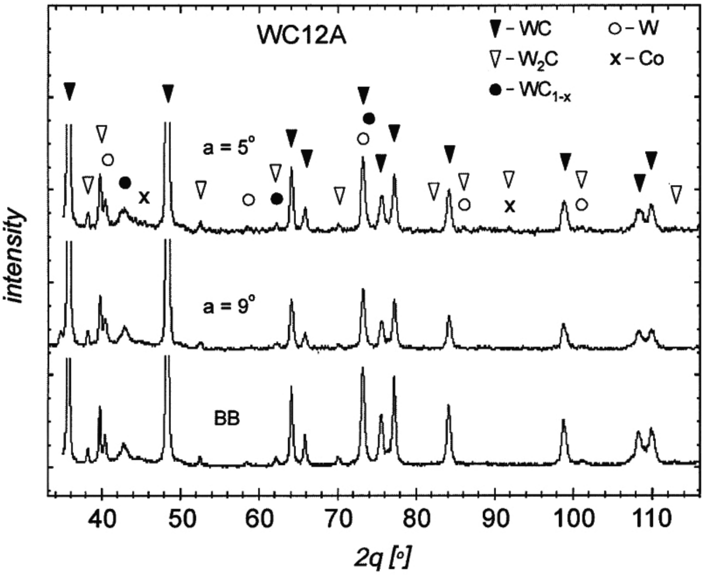

FIG. 10.3. Diffractograms of WC-12Co Amperit(WC12A) coating made according to the Bragg-Brentano geometry. The picture illustrates marked positions of the lines of identified phases.

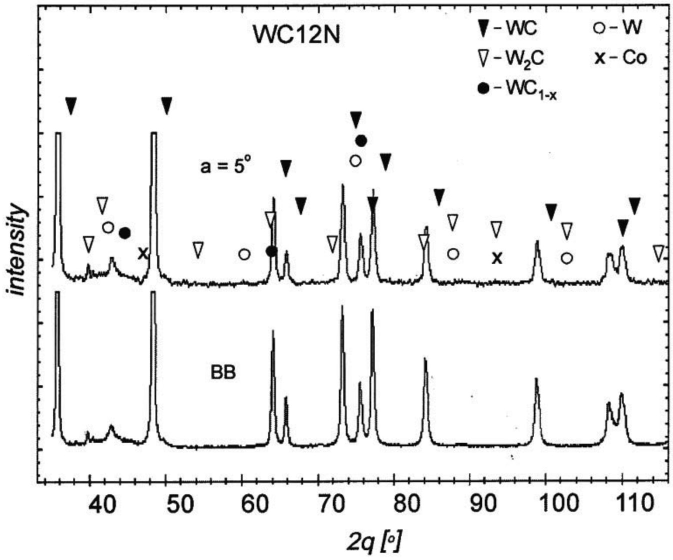

FIG. 10.4. Diffractograms of WC-12Co Nanox (WC12N) coating made according to the Bragg-Brentano geometry. The picture shows marked positions of the lines of identified phases.

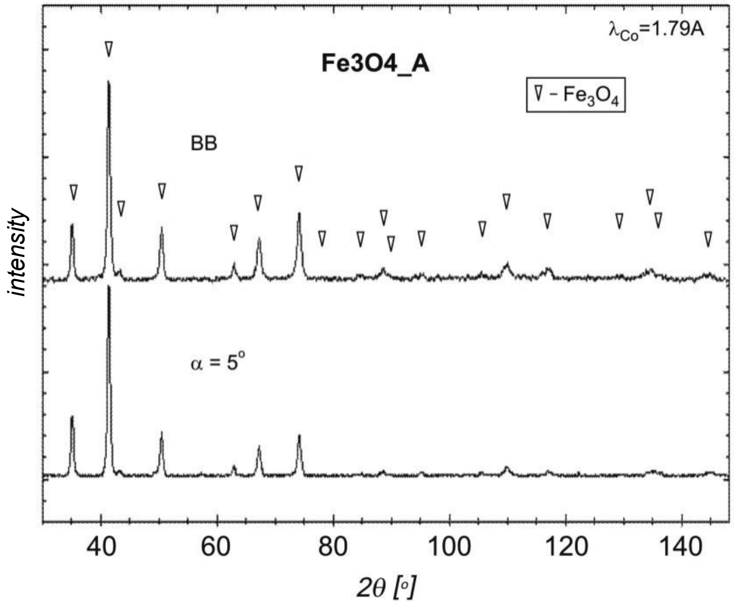

FIG. 10.5. Diffractograms of Fe_3O_4Inflox (Fe3O4_A) coating made according to the Bragg-Brentano geometry. The picture presents marked positions of the lines of identified phases.

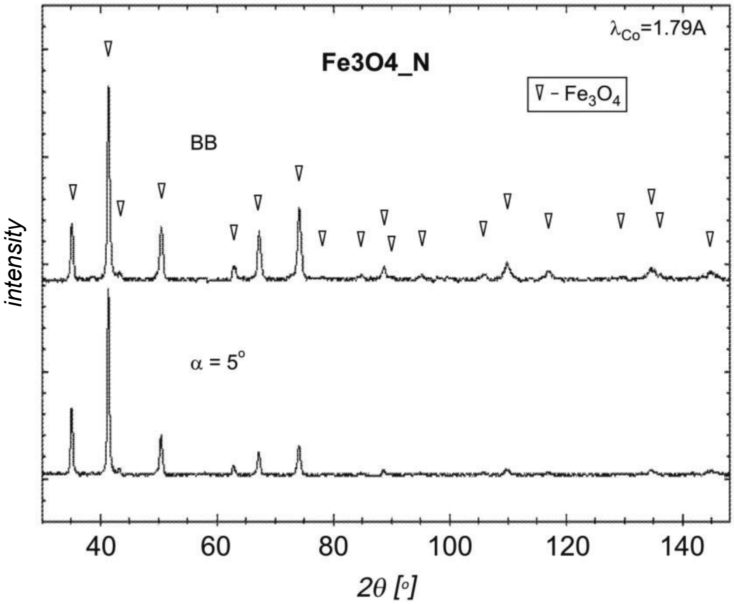

FIG. 10.6. Diffractograms of Fe_3O_4 Nanox (Fe3O4_N) coating made according to the Bragg-Brentano geometry. The picture illustrates marked positions of the lines of identified phases.

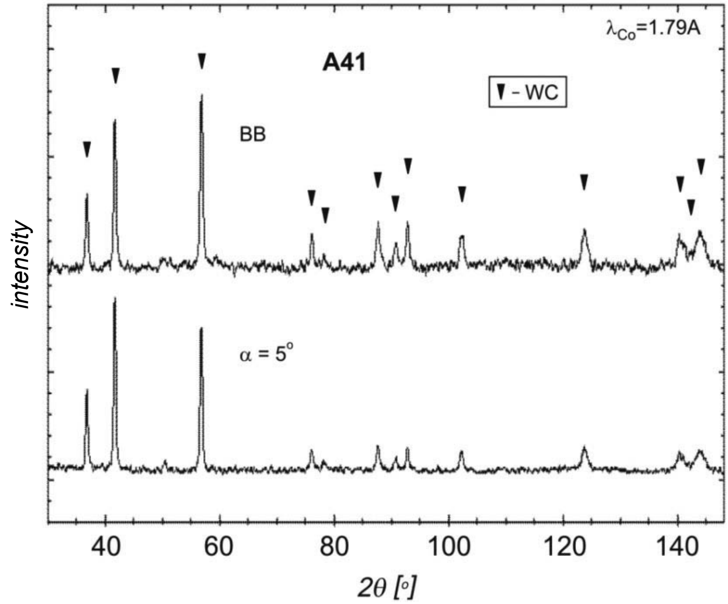

FIG. 10.7. Diffractograms of WC-12Co Amperit/Fe_3O_4Inflox (A41) gradient coating made according to the Bragg-Brentano geometry. The picture shows marked positions of the lines of identified phases.

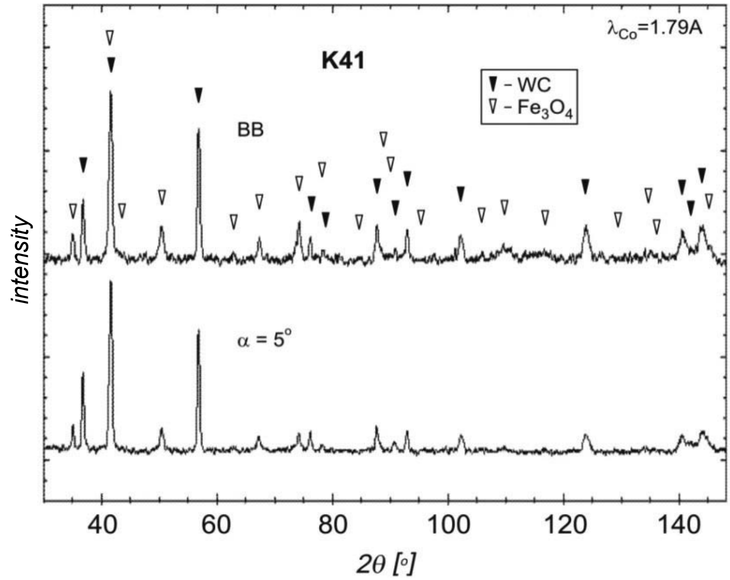

FIG. 10.8. Diffractograms of WC-12Co Nanox/Fe_3O_4 Nanox (K41) gradient coating made according to the Bragg-Brentano geometry. The picture presents marked positions of the lines of identified phases.

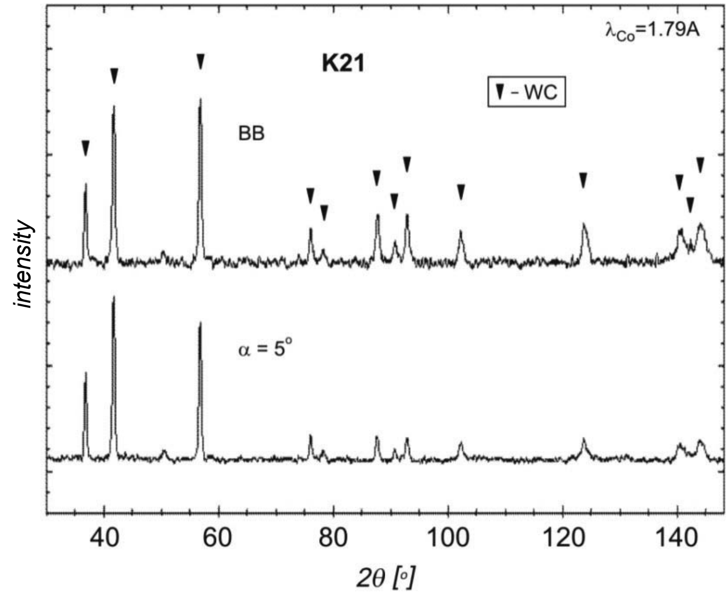

FIG. 10.9. Diffractograms of WC-12Co Amperit/Fe_3O_4Inflox (K21) coating made according to the Bragg-Brentano geometry. The picture shows marked positions of the lines of identified phases.

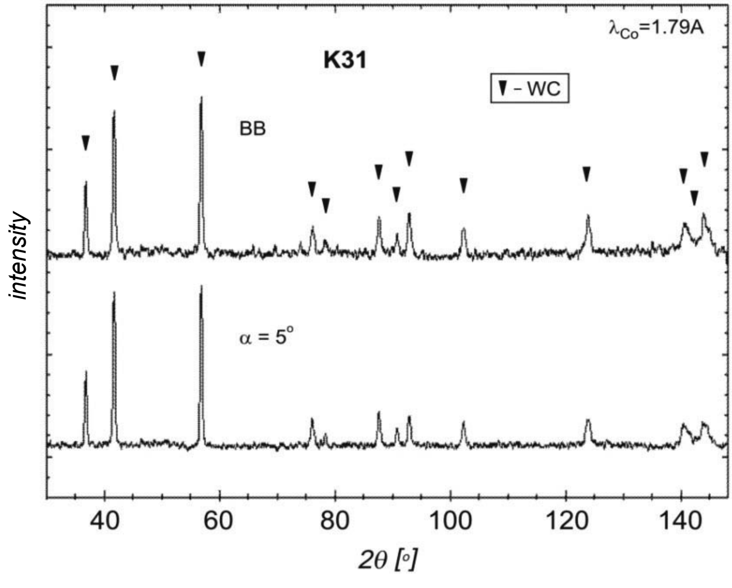

FIG. 10.10. Diffractograms of WC-12Co Nanox/Fe_3O_4 Nanox (K31) coating made according to the Bragg-Brentano geometry. The picture illustrates marked positions of the lines of identified phases.

Chapter 11

Results of the Taguchi Optimization Experiment

Results of experiment carried out according to Table 6.3 are presented in Tables 11.1÷11.12 and in Figures 11.1÷11.6.

TABLE 11.1. Results of Taguchi experiment for friction coefficient tests.

Experiment	Friction coefficient, μ	Standard deviation	**Coefficient *SN***
1	0.23	0.02646	**12.7273**
2	0.31333	0.02887	**10.05536**
3	0.17333	0.02082	**15.1808**
4	0.27333	0.02082	**11.24939**
5	0.47333	0.05686	**6.455074**
6	0.30333	0.02517	**10.34171**
7	0.15667	0.02082	**16.04965**
8	0.22333	0.01528	**13.00741**
9	0.20667	0.01528	**13.6788**

TABLE 11.2. Variance analysis of friction coefficient test results.

Parameter coefficient	S	f	$V = S/f$	ρ (%)
S_A	37.4350123	2	**18.717506**	54.52%
S_B	22.7643095	2	**11.382155**	33.16%
S_C	1.23157944	2	**0.6157897**	1.79%
S_D	7.22785402	2	**3.613927**	10.53%
Total	**68.6587553**			100.00%

TABLE 11.3. Results of Taguchi experiment for microhardness tests.

Experiment	Microhardness HV0.1	Standard deviation	**Coefficient *SN***
1	765.9	27.4568	**57.68903**
2	993.5	18.1123	**59.92799**
3	808.3	67.2476	**57.92493**
4	848.6	15.371	**58.58493**
5	794.1	14.8956	**57.94086**
6	959.5	62.4842	**59.63773**
7	830.3	11.2945	**58.31342**
8	929.4	12.0296	**59.35545**
9	887.2	59.3498	**58.36486**

TABLE 11.4. Variance analysis of microhardness test results.

Parameter coefficient	S	f	$V = S/f$	ρ (%)
S_A	0.07167103	2	**0.0358355**	1.36%
S_B	1.1589895	2	**0.5794947**	22.05%
S_C	1.50950896	2	**0.7547545**	28.72%
S_D	2.51589363	2	**1.2579468**	47.87%
Total	**5.25606312**			100.00%

TABLE 11.5. Results of Taguchi experiment for coating wear tests.

Experiment	Coating wear, g	Standard deviation	**Coefficient *SN***
1	0.00093	0.00021	**60.45757**
2	0.00143	0.00021	**56.81241**
3	0.00097	0.00015	**60.22276**
4	0.00137	5.8E-05	**57.28158**
5	0.00097	0.00012	**60.25335**
6	0.00113	0.00015	**58.86057**
7	0.00137	0.00015	**57.25073**
8	0.00093	0.00015	**60.5224**
9	0.00113	0.00015	**58.86057**

TABLE 11.6. Variance analysis of coating wear test results.

Parameter coefficient	*S*	*f*	*V* = *S*/*f*	ρ (%)
S_A	0.22207597	2	**0.111038**	1.21%
S_B	1.73374803	2	**0.866874**	9.46%
S_C	8.29544411	2	**4.1477221**	45.28%
S_D	8.06891567	2	**4.0344578**	44.04%
Total	**18.3201838**			100.00%

TABLE 11.7. Results of Taguchi experiment for countersample wear tests.

Experiment	Countersamlpewear, g	Standard deviation	**Coefficient *SN***
1	0.00087	0.00012	**61.19186**
2	0.00107	0.00015	**59.38045**
3	0.00067	0.00015	**63.37242**
4	0.00097	5.8E-05	**60.28415**
5	0.0008	0.0001	**61.8932**
6	0.00097	0.00012	**60.25335**
7	0.00113	5.8E-05	**58.90534**
8	0.0009	0.0001	**60.87955**
9	0.00093	0.00015	**60.5224**

TABLE 11.8. Variance analysis of countersample wear test results.

Parameter coefficient	S	f	*V* = *S*/*f*	ρ (%)
S_A	2.2258026	2	**1.1129013**	15.69%
S_B	2.36757927	2	**1.1837896**	16.69%
S_C	2.6500451	2	**1.3250225**	18.68%
S_D	6.94600704	2	**3.4730035**	48.95%
Total	**14.189434**			100.00%

TABLE 11.9. Results of Taguchi experiment for coating roughness tests.

Experiment	R_a, µm	Standard deviation	**Coefficient *SN***
1	0.209	0.02338	**14.12581**
2	0.2018	0.05095	**13.95421**
3	0.2538	0.01954	**11.64297**
4	0.2444	0.06027	**13.02442**
5	0.2572	0.04717	**12.48657**
6	0.2466	0.05055	**11.35794**
7	0.255	0.05211	**10.94431**
8	0.2578	0.03383	**11.96905**
9	0.2346	0.02373	**12.08745**

TABLE 11.10. Variance analysis of coating roughness test results

Parameter coefficient	S	f	$V = S/f$	ρ (%)
S_A	3.77051028	2	**1.8852551**	38.27%
S_B	2.24097963	2	**1.1204898**	22.74%
S_C	2.68889646	2	**1.3444482**	27.29%
S_D	1.15244165	2	**0.5762208**	11.70%
Total	**9.85282802**			100.00%

TABLE 11.11. Results of Taguchi experiment for coating adhesion tests

Experiment	Adhesion, MPa	Standard deviation	**Coefficient *SN***
1	34.3467	2.62407	**30.66819**
2	37.09	1.67654	**31.3669**
3	33.46	1.11862	**30.48057**
4	42.6867	3.96263	**32.53115**
5	33.0467	3.8238	**30.2556**
6	35.32	3.79237	**30.8557**
7	32.7933	2.2646	**30.27566**
8	35.6867	3.3395	**30.96836**
9	33.0467	3.8238	**30.2556**

TABLE 11.12. Variance analysis of coating adhesion test results.

Parameter coefficient	*S*	*f*	*V* = *S*/*f*	ρ (%)
S_A	0.76597033	2	**0.3829852**	17.76%
S_B	0.59175439	2	**0.2958772**	13.72%
S_C	1.64699297	2	**0.8234965**	38.18%
S_D	1.30878495	2	**0.6543925**	30.34%
Total	**4.31350264**			100.00%

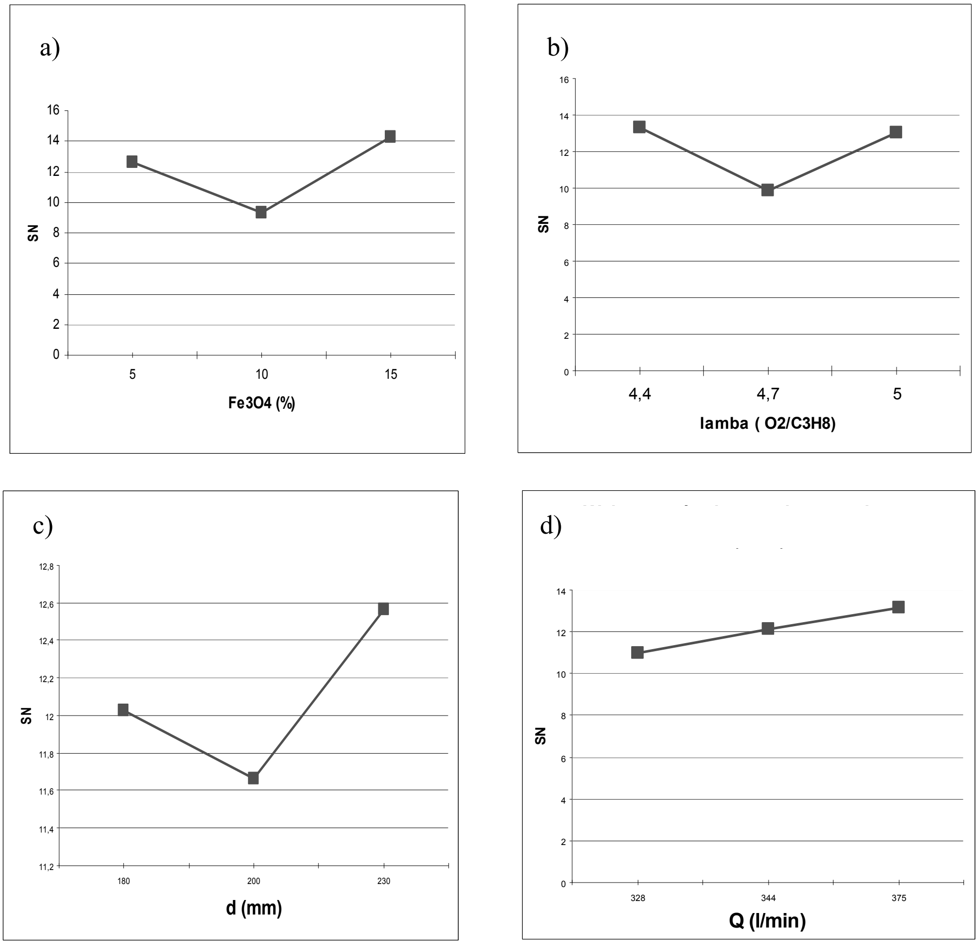

FIG. 11.1. Influence of spraying parameters on friction coefficient (tribotester “ball on disc”, chapter 6.2.3): a) Fe_3O_4 addition, b) composition of flammable gases, c) spraying distance, d) air mass flow.

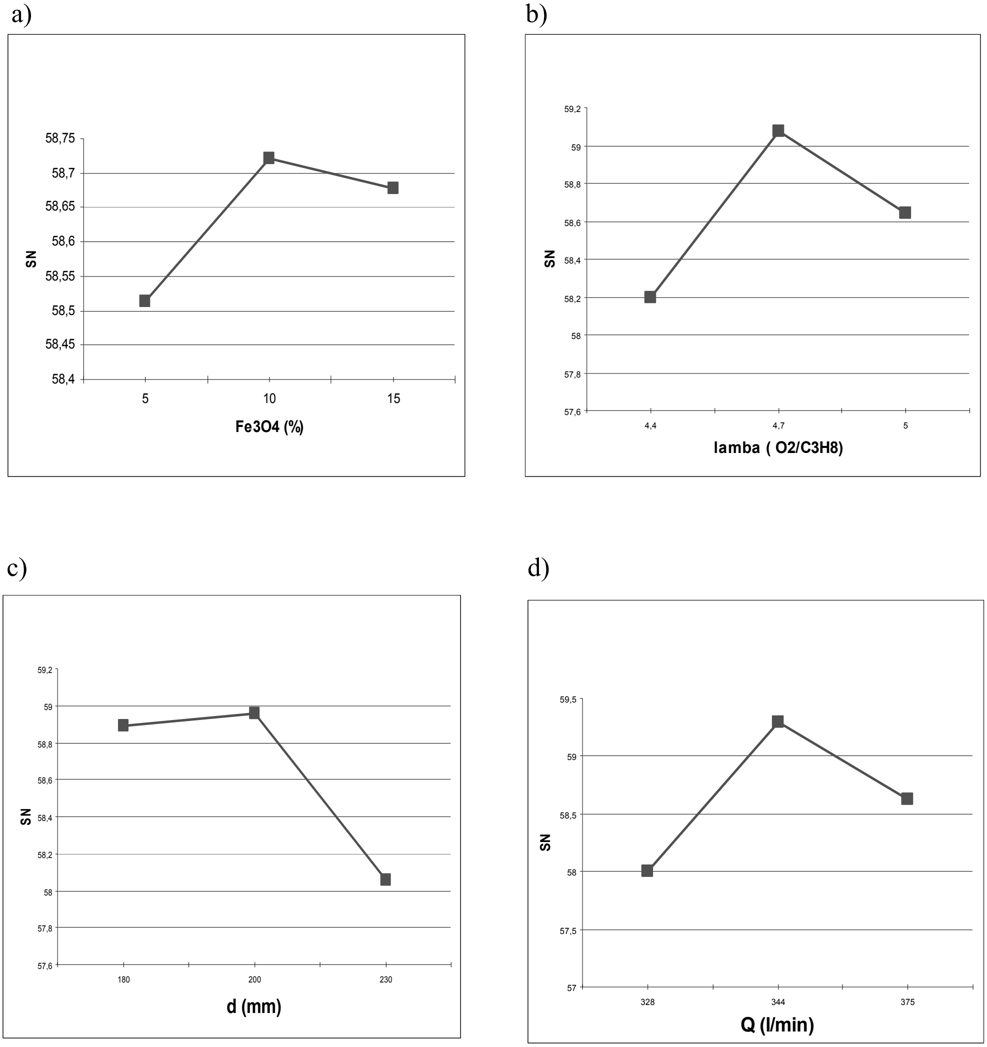

FIG. 11.2. Influence of spraying parameters on coating microhardness (hardness tester Matuzawa MMT-X3A, chapter 6.2.4): a) Fe_3O_4 addition, b) composition of flammable gases, c) spraying distance, d) air mass flow.

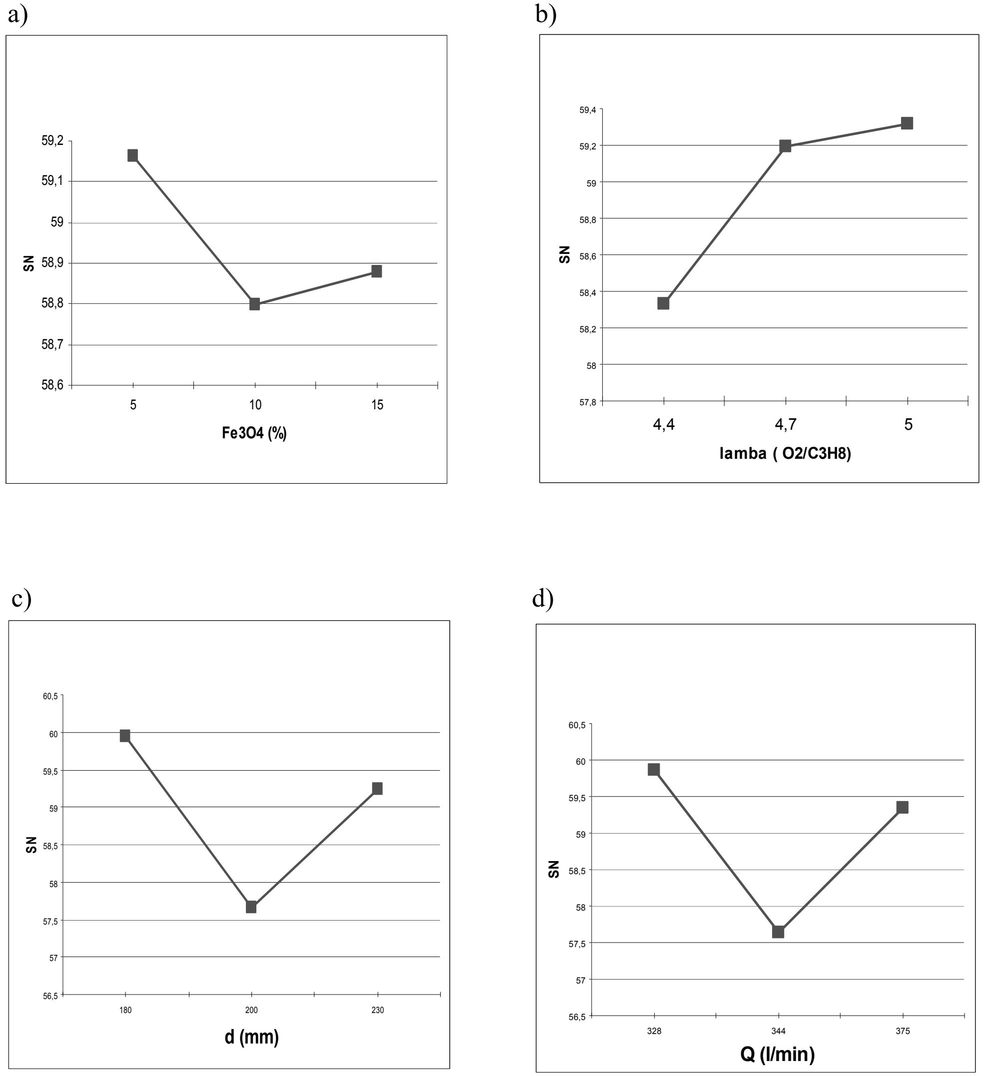

FIG. 11.3. Influence of spraying parameters on coating wear (analytical balance Denver Instrument Company, chapter 6.2.4): a) Fe_3O_4 addition, b) composition of flammable gases, c) spraying distance, d) air mass flow.

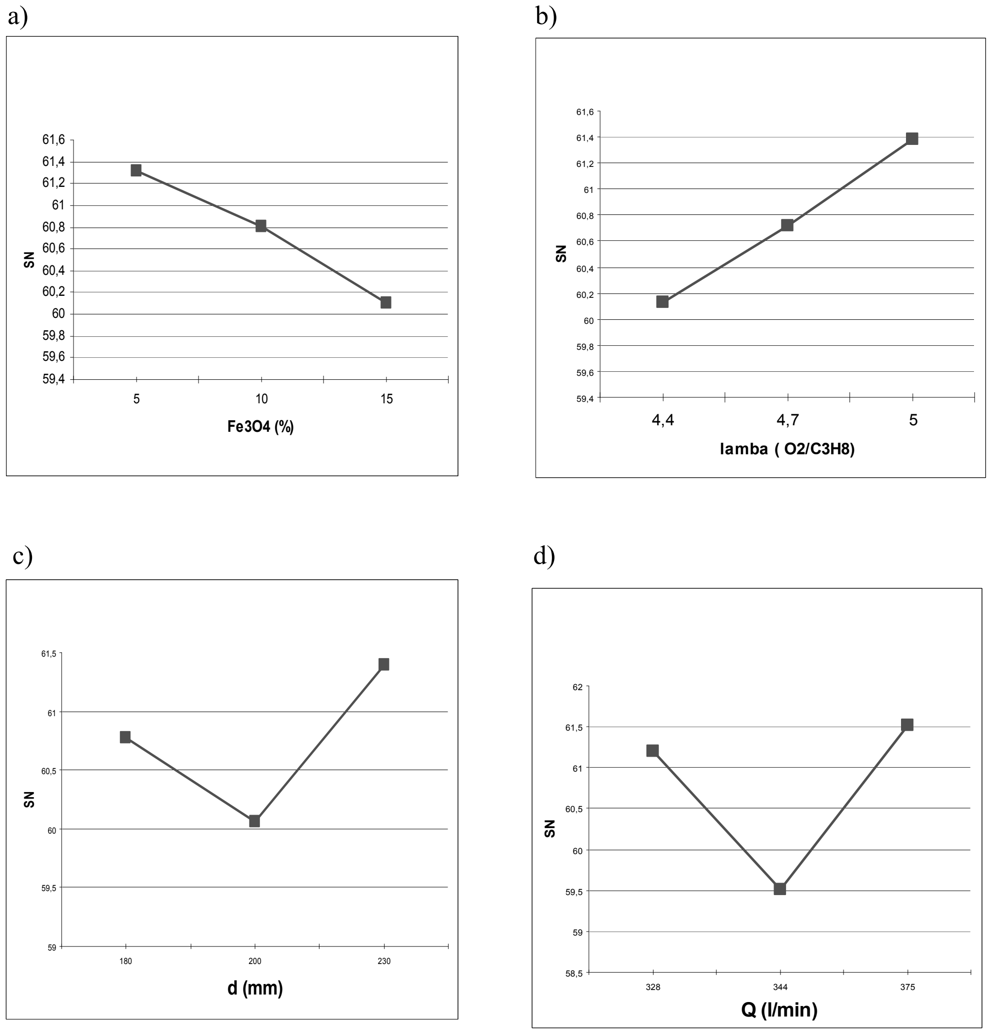

FIG. 11.4. Influence of spraying parameters on countersample wear (analytical balance Denver Instrument Company, chapter 6.2.4): a) Fe_3O_4 addition, b) composition of flammable gases, c) spraying distance, d) air mass flow.

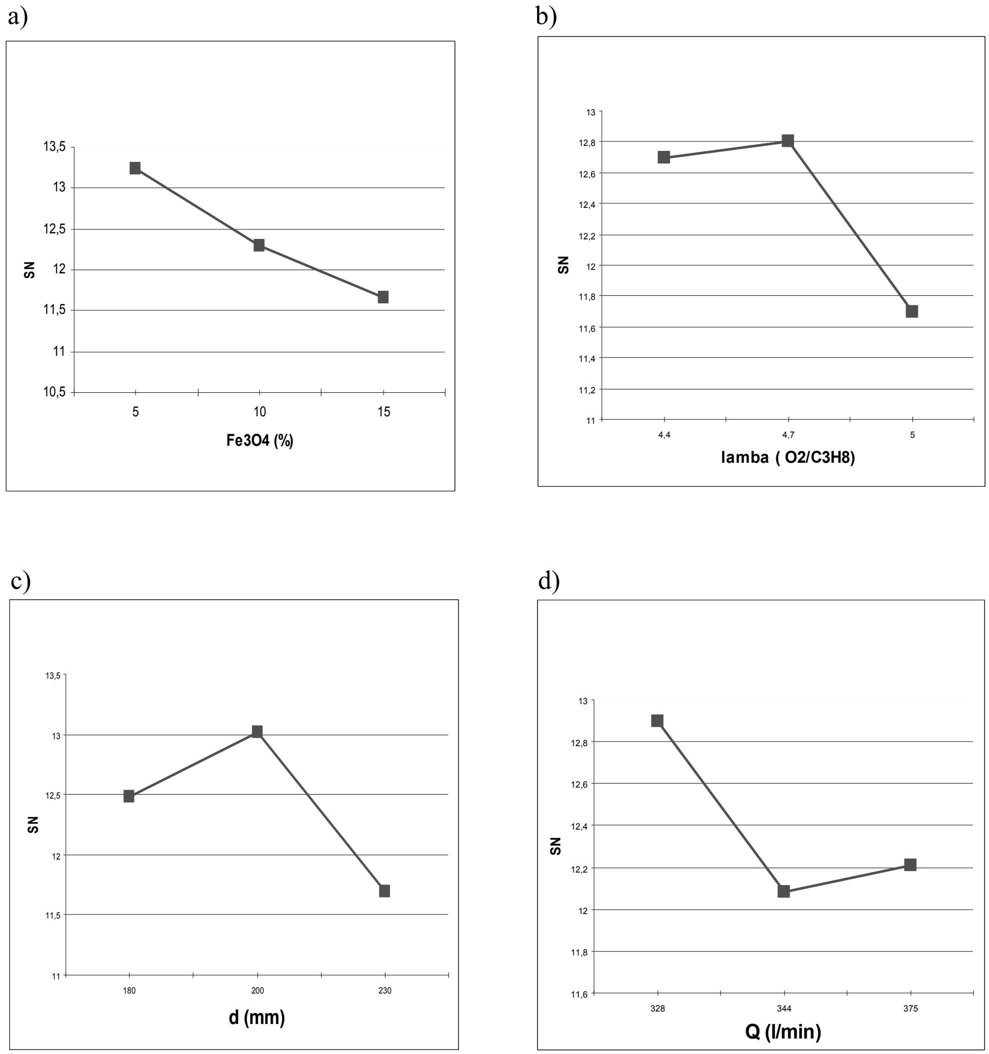

FIG. 11.5. Influence of spraying parameters on coating roughness (device Talysurf 4, chapter 6.2.4): a) Fe_3O_4 addition, b) composition of flammable gases, c) spraying distance, d) air mass flow.

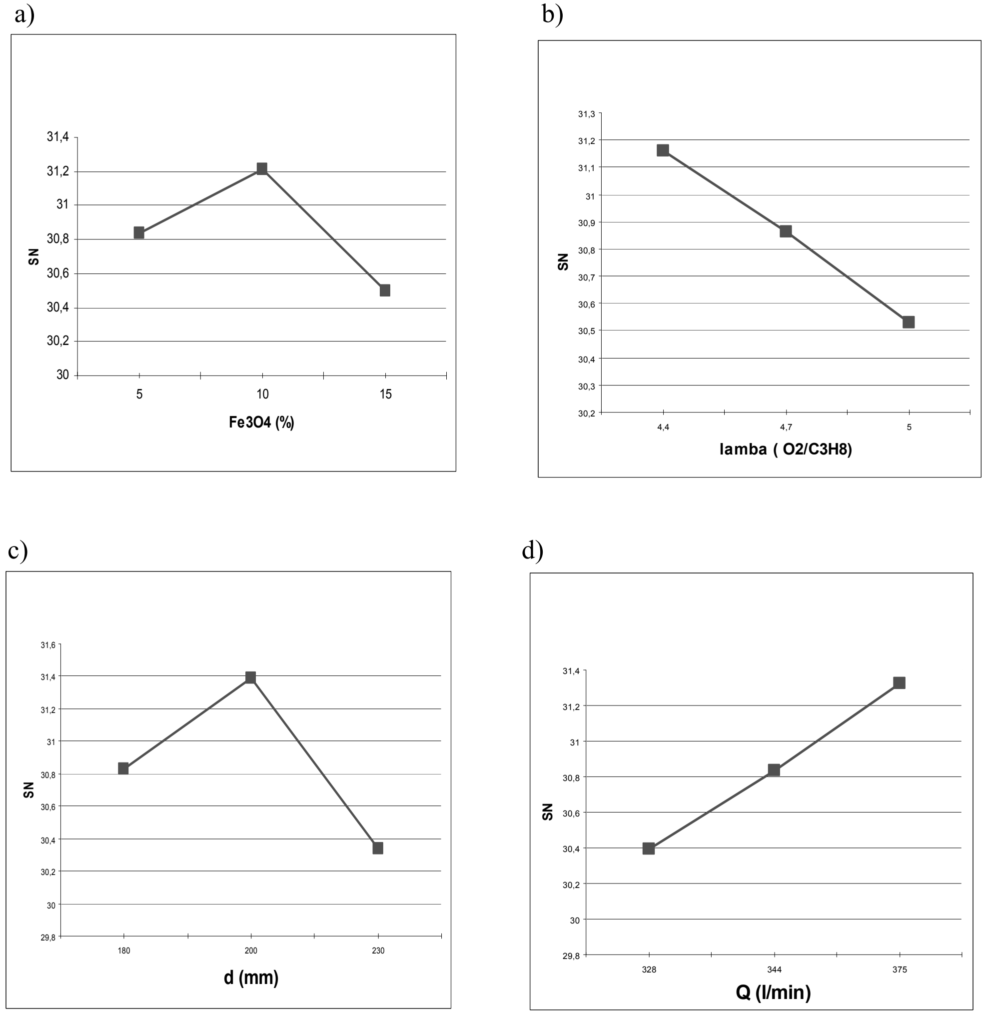

FIG. 11.6. Influence of spraying parameters on coating adhesion (testing machine Instron 8501, chapter 6.2.6): a) Fe_3O_4 addition, b) composition of flammable gases, c) spraying distance, d) air mass flow.

Chapter 12

Mechanism of Lubrication

Lubrication is a critical problem in machine operation as it is strictly related to energy losses resulting from friction and wear. Most machines use lubricants in a liquid form, but some friction pairs require solid lubricants. These are particularly useful when the operating conditions include low or high temperatures, or a vacuum. It is important that, by applying a solid lubricant, we are able to simplify the friction pair design and reduce its weight. The current research into solid lubricants is concerned with theoretical and practical problems, which are varied and complex. There is, however, no common general theory of solid lubrication. The structural, adsorption, and crystal-chemical approaches, developed in the middle of the 19th century, are true only under certain conditions; they do not explain the behaviour of solid lubricants in all environments [16, 49, 75, 118, 119]. The starting point for further analysis is the assumption that the real surface of contact F_r of two mating elements is considerably smaller than the nominal surface and can be represented as (12.1):

$$F_r = N/p_q \tag{12.1}$$

where: N – normal force, p_q – unit loads at the interface.

For the metal-metal contact, the friction force T is (12.2):

$$T = F_r \sigma_t \tag{12.2}$$

where: σ_t – unit shear stresses necessary to shear the welded areas.

Using the formula for the coefficient of friction, we obtain (12.3);

$$\mu = T/N = F_r \sigma_t \,/\, F_r p_q = \sigma_t \,/\, p_q \tag{12.3}$$

From the above relationship it is clear that the coefficient of friction is not dependent on the actual surface area of the elements in contact F_r. To reduce the coefficient of friction, we need to reduce the unit shear stresses necessary to shear the melted areas σ_t and increase the unit loads at the interface p_q. If an additional body with small σ_t, i.e. a solid lubricant, is introduced between the moving surfaces, the coefficient of friction decreases. Friction joints with solid lubricants are interesting to investigate because it is essential to explain all the processes taking place between the moving elements. Particular attention is given to the surface microstructure, its composition, phase distribution and the amount of solid lubricant, all having a considerable effect on the coefficient of friction and wear. There exists an optimal composition of the composite that ensures the minimum values of the coefficient of friction and wear (Fig. 12.1) [71].

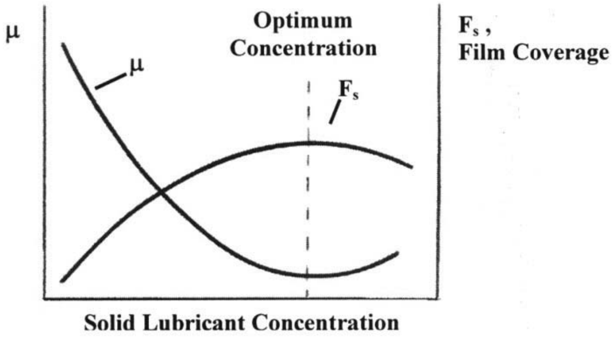

FIG. 12.1. Schematic diagram of the relationship between the solid lubricant concentration, the solid lubricant film coverage and the coefficient of friction.

Analyzing the surface of the HVOF sprayed coating, we assumed that the coating consisted mainly of WC grains in the cobalt matrix and the solid lubricant (Fe_3O_4). At the surface, we had W2C, WC1-x and tungsten phases, which resulted from the action of the HVOF spraying stream on the tungsten carbide (WC) grains (Fig. 12.2).

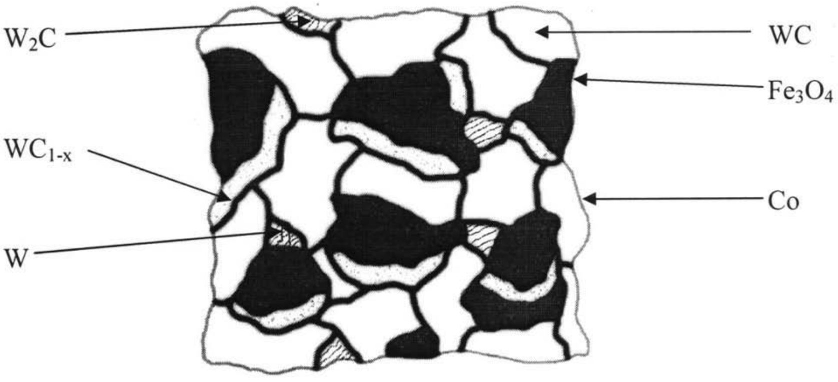

FIG. 12.2. Model of surface layer of the HVOF spray WC-12Co/Fe_3O_4 composite coating.

The processes of sliding friction and wear of the HVOF spray WC-12Co/ Fe_3O_4 composite coatings were responsible for the formation of grains containing WC, W_2C, and Fe_3O_4, WC_{1-x} and tungsten particles. The particles crushed, combined and spread in the coating-counter surface system. Their mass (and dimensions) were reduced due to the development of shear stresses. The small, very hard WC grains were the most important in the process, as they contributed to the wear of the coating and the counter surface. On the surface of the HVOF spray nanostructured and conventional coatings, there were ridges forming as a result of the action of the worn WC grains (Fig. 12.3). The other grains, i.e. Co and particularly Fe_3O_4, brought about a decrease in the static stresses, and accordingly, a decrease in the coefficient of friction and wear. The wear analysis confirmed this mechanism of lubrication and wear.

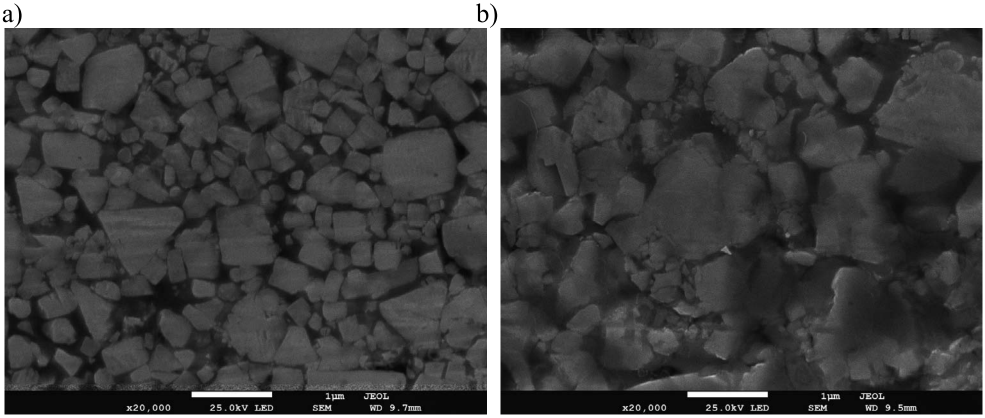

FIG. 12.3. Morphology of the worn surfaces of WC-12Co coating: a) nanostructured, b) conventional.

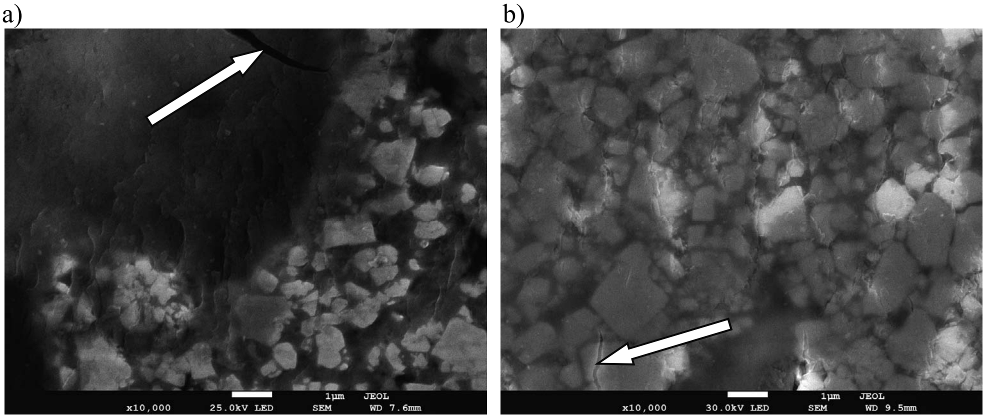

FIG. 12.4. Morphology of the worn surfaces of WC-12Co/Fe_3O_4 coating: a) nanostructured, b) conventional.

The counter body pressing against the HVOF spray composite coating caused the particles of the solid lubricant, Fe_3O_4, to fill in the coating pores. The lubricant was spread over the tungsten carbide grains and the cobalt matrix. The smooth surface was able to retain the effectiveness of the lubricating layer (Fig. 12.4). Iron oxide, Fe_3O_4, is a material with a lamellar structure in the direction (001). At the interface of the coating and the 100Cr6 steel ball (the tests conducted using a ball-on-disc tribotester), there were layers varying in thickness. The light WC grains were grey in colour varying in intensity. When the 100Cr6 steel ball was in contact with a larger amount of Fe_3O_4, the lubricant surface cracked because the yield point was exceeded (Fig. 12.4, arrows). There was no trace of spalling of the solid lubricant.

The WC and W_2C particles forming during the wear processes were transported outside the joint or absorbed by the coating micropores. The thin films of Fe_3O_4 forming during friction on the surface of tungsten carbides and the cobalt matrix indicated that both the HVOF spray nanostructured and the conventional solid lubricants were characterized by high adhesion. The nanostructured and the conventional layers were not regular in shape, which was due to their deformations at the interface (Fig. 12.5). The lubricant spalling resulted in the formation of flaky particles, which were several dozen nanometers in size (Fig. 12.6). There were no clear differences between the nanostructured and the conventional solid lubricant layers. In the direct area of contact, where the distances between the surfaces were small, the nanostructured Fe_3O_4 films behaved in the same way as the conventional ones. The solid lubricant, Fe_3O_4, well adhered to the tungsten carbide grains in the cobalt matrix. The thin, strong layer was oriented in the direction of motion. It can be concluded that this type of lubrication best coincides with the structural theory of solid lubricants, which assumes the existence of easy slide planes in the crystalline structure of the substance acting as a solid lubricant.

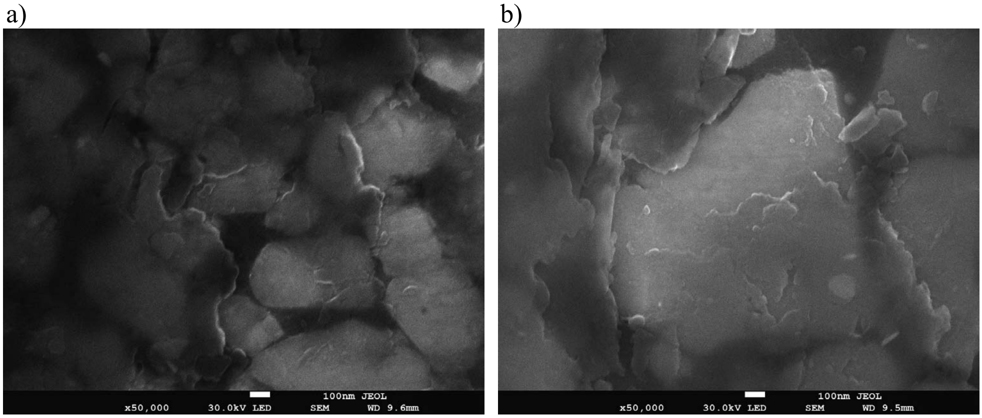

FIG. 12.5. Morphology of the Fe_3O_4 films on the WC-12Co coating in contact with the 100Cr6 steel ball: a) nanostructured, b) conventional.

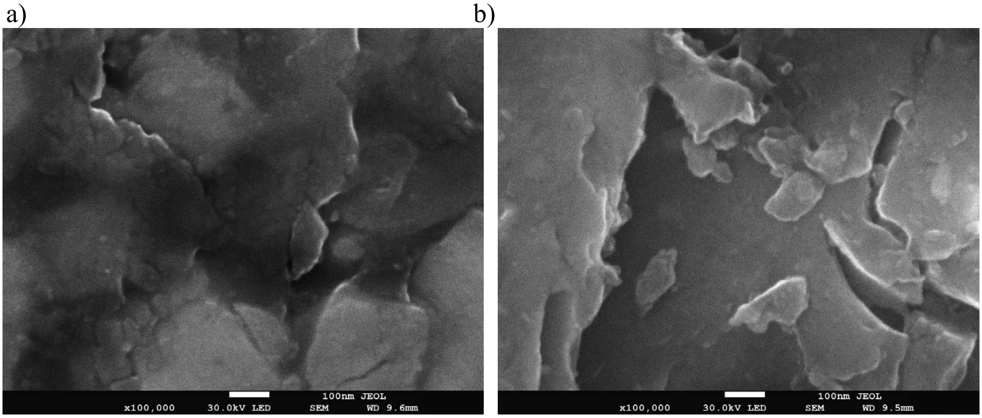

FIG. 12.6. Flaky nanometric Fe_3O_4 particles: a) nanostructured, b) conventional.

While the HVOF spray coating and the counter surface were in contact, the coefficient of friction for the area covered with the solid lubricant stabilized. If we assume that the predetermined area covered with a film of solid lubricant has no ridges, we consider only the effect of adhesion. The friction force can thus be expressed as (12.4):

$$T = F_m \sigma_t + F_s \sigma_s \tag{12.4}$$

where: F_m – surface area of the elements in contact at the metal–tungsten carbide interface; F_s – solid lubricant film coverage; σ_s – stresses shearing the solid lubricant; σ_t – unit shear stresses necessary to shear the melted areas.

If the load N is distributed proportionally over the area of contact, the coefficient of friction can be written as (12.5):

$$\boxed{\mu = \chi_m \mu_m + \chi_s \mu_s} \tag{12.5}$$

where: χ_m – percentage share of the metal-tungsten carbide contact; χ_s – percentage share of the solid lubricant film coverage; μ_m – coefficient of friction of the metal-tungsten carbide interface; μ_s – coefficient of friction of the solid lubricant at the interface.

The above relationship suggests that the coefficient of friction will decrease with an increase in the areas of surfaces covered with the lubricating film, which results from an increase in the amount of the solid lubricant in the composite. The coefficient of friction drops from the maximum value, observed when the metal-tungsten carbide system is at full contact, to a minimum value, reported at the complete solid lubricant film coverage. The self-lubrication of the WC-12Co/Fe_3O_4 coating is mainly dependent on the film spreadability, which, in turn, is attributable to its strength, adhesion and microstructure. The film may differ in thickness, depending on the contact conditions and the presence of wear products. A thick film with a high concentration of a solid lubricant is less wear resistant and more prone to deterioration due to local spalling [177]. The film microstructure can be significant and depends on the method of introduction of the solid lubricant into the friction joint. The presence of nanostructured particles of the solid lubricant in the nanostructured coating (Fig. 12.7a) improved the lubrication conditions and the wear resistance of the coating [81, 90] (Fig. 12.7b).

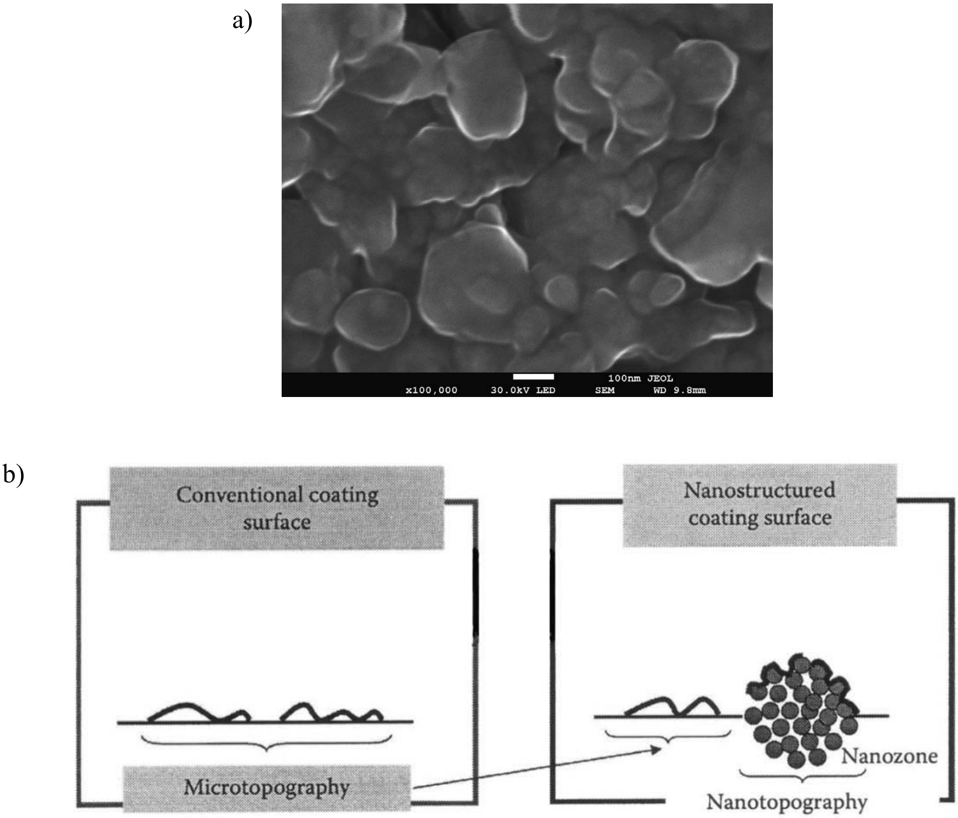

FIG. 12.7. Fe_3O_4 nanograins in the HVOF spray WC-12Co/Fe_3O_4 coating (a), model of the thermal spray conventional and nanostructured coatings (b).

Another important factor contributing to the correct performance of surfaces in contact is the capacity of load bearing through the substrate of the solid lubricant, as it conditions effective lubrication. A further increase in the content of the solid lubricant after an optimal amount is achieved to ensure complete film coverage leads to a decrease in the mechanical properties of the composite. If the substrate covered by the lubricating film has no sufficient mechanical properties, the coefficient of friction rises and the film deteriorates.

If the lubricating film covers the entire surfaces in contact F, the friction force T is (12.6):

$$T = F\sigma_s \tag{12.6}$$

and the coefficient of friction μ is expressed as (12.7):

$$\mu = F\sigma_s / N \tag{12.7}$$

If the normal load is small, then the film surface is only plastically deformed and the surface area of the elements in contact F with a metal ball can be expressed as (12.8):

$$F = \pi\ (3Nr/2E^{'})^{2/3} \tag{12.8}$$

where: r – ball radius, $E^{'}$ – equivalent modulus of elasticity for the lubricating film and the steel ball.

After substituting the relationship (12.8) into formula (12.7), we get (12.9):

$$\mu = \sigma_s\ (3r/2E^{'})^{2/3} / N^{1/3} \tag{12.9}$$

If the plastic deformation occurs under a large load, the contact surface can be expressed as (12.10) [130]:

$$F = N / H \tag{12.10}$$

where: H – composite hardness.

Substituting the relationship (12.10) into Eq. (12.7) yields (12.11):

$$\mu = \sigma_s/H \tag{12.11}$$

The relationships (12.8) and (12.10) show that the modulus of elasticity of the lubricating film and the hardness of the composite had a considerable effect on the film behaviour when under friction conditions. The higher the concentration of the solid lubricant, the lower the modulus of elasticity of the lubricating film and the lower the hardness of the composite. These properties were responsible for the gradual increase in the coefficient of friction, and consequently in the friction force, which caused spalling of the lubricating film and an increase in the coating wear. Higher mechanical properties of the composite slowed down the wear process. Analyzing the images of the WC-12Co composite coating containing a solid lubricant, Fe_3O_4, we can differentiate between stages of changes in the coating surface morphology. Before the interaction with the counter body, the solid lubricant covered the coating surface, as the lubricant was a component of the microstructure formed by HVOF spraying (Fig. 12.8a).

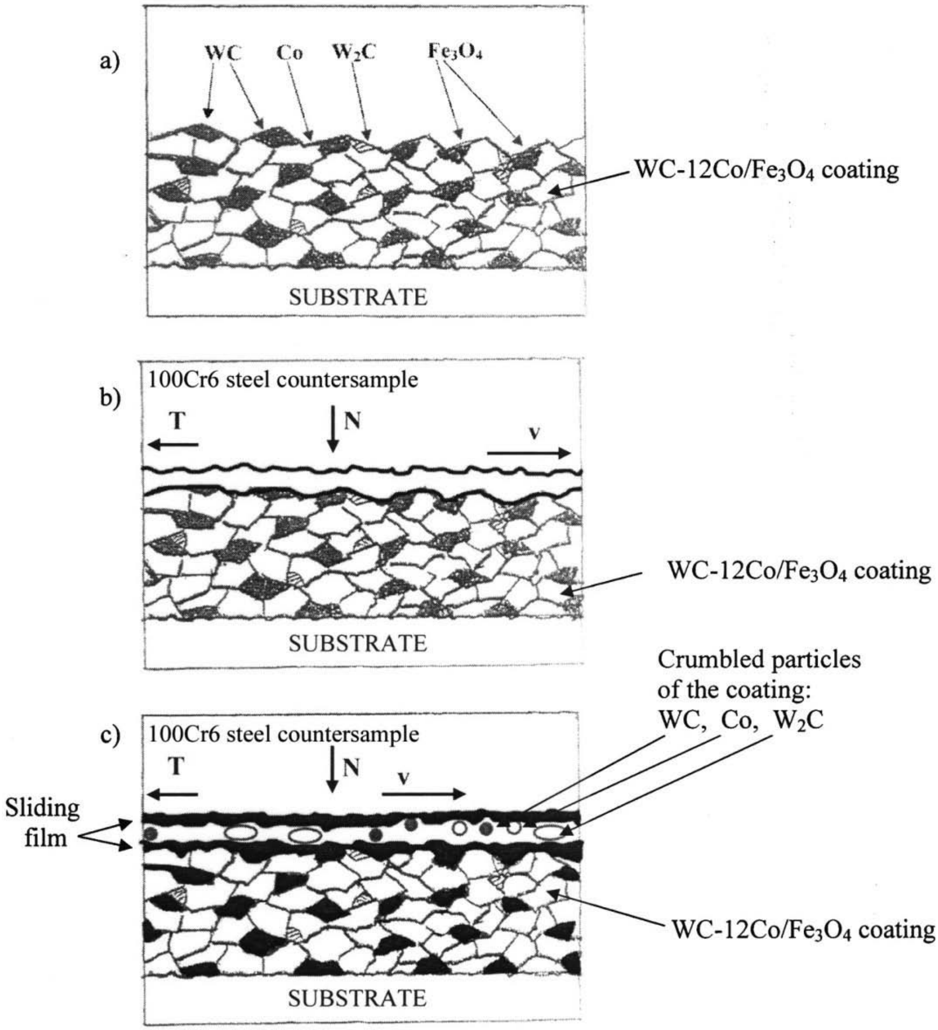

FIG. 12.8. Model of formation of the sliding film with Fe_3O_4 on the HVOF spray WC-12Co/Fe_3O_4 coating: a) model of the microstructure of HVOF spray WC-12Co/Fe_3O_4 coating, b) surface area of contact between the HVOF spray WC-12Co/Fe_3O_4 coating and the counter surface (100Cr6 steel), c) sliding film with Fe_3O_4 formed on the surfaces of the WC-12Co/Fe_3O_4 coating and the counter body.

During the first stage of the interaction, the solid lubricant was pressed against by the counter body. That caused the lubricant film coverage to increase due to the shear and sliding of the subsequent layers; consequently, the lubricant spread further over the coating surface (Fig. 12.8b). Once the interaction stabilized, the whole surface area of the coating was covered with a thin layer of the solid lubricant, Fe_3O_4, (Fig. 12.8c). That thin layer of Fe_3O_4 had very good adhesion both to the coating containing tungsten carbide grains in the cobalt matrix and to the counter surface. As a result, the layer did not wear out quickly and the interaction of the moving surfaces improved. Friction took place mainly between the two layers of Fe_3O_4, where, as mentioned above, there existed planes of easy slides. When admissible loads were exceeded, the lubricating film deteriorated locally, which led to a direct contact of the hard particles (WC or W_2C) with the irregularities of the mating surface (Fig. 12.9). Consequently, the hard grains were pulled out of the cobalt matrix and transported off the contact area. Simultaneously, some more areas containing a solid lubricant were detected; they were used up to produce a lubricant layer. According to the concept of boundary lubrication [118], the deposition of the very thin layer of a solid lubricant with low σ_s reduces the coefficient of friction μ (12.11).

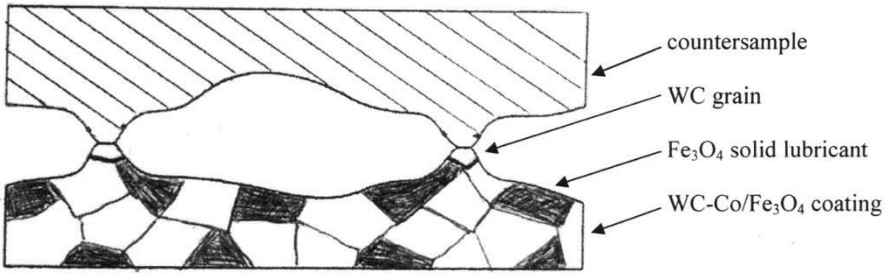

FIG. 12.9. A model of interaction of a composite coating WC-Co/Fe_3O_4 with a countersample.

The wear resistance of the composite coatings was dependent not only on the amount, dimensions and distribution of the solid lubricant but also on the development of the wear process. The process, on the other hand, was affected by a number of factors such as hardness, microstructure, bonding between the lubricant and the matrix, as well as the phase composition, continuity and thickness of the lubricating film.

Chapter 13

Spray Parameters vs. Properties of the Composite Coatings

Table 13.1 shows the relationship between the percentage share of the spray parameters ρ (%) and the coating properties, which was determined using the Taguchi optimization approach. In Table 13.2, on the other hand, we can find the optimal spray parameters for producing composite coatings.

TABLE 13.1. Percentage share of the spray parameters vs. the properties of the composite coatings.

ρ, % / Coating properties	η, % wt. Fe_3O_4	λ, O_2/C_3H_8	d, mm	Q, l/min
Coefficient of friction	54.52%	33.16%	1.79%	10.53%
Microhardness, HV0.1	1.36%	22.05%	28.72%	47.87%
Wear of coating, g	1.21%	9.46%	45.28%	44.04%
Wear of countersample, g	15.69%	16.69%	18.68%	48.95%
R_a, µm	38.27%	22.74%	27.29%	11.70%
Adhesion, MPa	17.76%	13.72%	38.18%	30.34%

TABLE 13.2. Optimal spray parameters to achieve the desired property of the coating.

Spray parameter / Coating properties	η, % wt. Fe_3O_4	λ, O_2/C_3H_8	d, mm	Q, l/min
Coefficient of friction	10%	4.7	200	336
Microhardness, HV0.1	10%	4.7	200	375
Wear of coating, g	10%	4.4	200	375
Wear of countersample, g	15%	4.4	200	375
R_a, µm	15%	5.0	230	375
Adhesion, MPa	10%	4.4	200	414

As shown in Table 13.1, the coefficient of friction was most affected by the content of Fe_3O_4 (54.52%); microhardness resulted mainly from the air flow rate (47.87%); wear was most influenced by the spray distance and the air flow rate (45.28% and 44.04%, respectively); the wear of the counter surface was mostly dependent on the air flow rate (48.95%); roughness was primarily due to the content of Fe_3O_4 (38.27%); and adhesion was largely a result of the spray distance (38.18%).

TABLE 13.3. Spray parameters used to produce the composite coatings.

Spray parameters	η, % wag. Fe_3O_4	λ, O_2/C_3H_8	d, mm	Q, l/min
	10%	4.4	200	375

TABLE 13.4. Properties of the sprayed coatings and electroplated chromium coating.

Coating properties	Coating				
	Nanostructural composite	Conventional composite	WC-12Co Nanox	WC-12Co Amperit	Galvanic chrome
Friction coefficient	0.15±0.02	0.48±0.04	0.26±0.01	0.88±0.02	0.78±0.03
Microhardness, HV0.1	863±62	892±48	966±36	1229±19	968±16
Wear of coating, g	0.0011	0.0018	0.0012	0.0019	0.0027
Wear of countersample, g	0.0009	0.0014	0.0011	0.0011	0.0019
R_a, µm	0.241±0.21	0.193±0.18	0.060±0.05	0.010±0.04	0.11±0.04
Adhesion, MPa	34.26±2.67	39.45±3.48	46±4.2	41±3.6	–
Scuffing resistance, N	1845±145	1793±182	1980±173	1853±207	268±34
Residua stress, MPa, substrate PA6	-166±8	80±7	166±13	-153±13	–
Residua stress, MPa, substrate C45	145±10	260±12	261±25	482±55	–

The spray parameters were corrected taking into consideration the coefficient of friction as well as the minimum wear of the coating and of the counter surface. The corrections made to the standard parameters included applying a 10% content of Fe_3O_4 in the mixture and decreasing the oxygen-to-acetylene ratio and the spray distance. The air flow rate remained unchanged. The corrected parameters are shown in Table 13.3.

The corrected spray parameters were used to deposit the nanostructured composite coatings. The conventional coatings were produced under the same conditions. Both types of coatings were tested to determine their coefficient of friction, microhardness, wear, wear of the counter surface, roughness, adhesion, seizure resistance and residual stresses. The results are given in Table 13.4.

Chapter 14

Discussion of Results

The morphology analysis conducted with a JOEL JSM 5400 SEM, an FEI Nova™NanoSEM 200 and a Philips CM20 TEM equipped with an EDAX EDX system to study the conventional powders (WC-12Co 519.074 and Fe_3O_4 Inflox™26FE23) and the nanostructured powders (WC-12Co Nanox™S7412 and Fe_3O_4 Nanox™26FE23) to be deposited by HVOF spraying showed that agglomeration and sintering of fine grains were responsible for the formation of the materials. The particle morphology analysis and the metallographic analysis confirmed these findings. The particle size analysis carried out by means of a Sympatec HELOS laser diffraction analyzer indicated that the powders had diverse particle size distributions. The WC-12Co Nanox™S7412 powder grains contained WC particles ranging in size from several dozen nanometers to one micrometer. The Fe_3O_4 Nanox™26FE23 powder particles contained Fe_3O_4 nanocrystals 13 nm ±3 nm in size. The diffraction analysis performed with a Bruker D-8 Advance X-ray diffractometer confirmed the phase composition of the coating materials. The metallographic analysis of the WC-12Co coatings showed that there was a clear difference in the size of tungsten carbide grains between the conventional and the nanostructured coatings. The coatings produced from the nanostructured powder had a fine-grained nanocrystalline structure. Their porosity was lower in spite of the higher amount of larger grains in the nanostructured powder. The higher porosity of the conventional coatings was probably due to the higher porosity of the powder particles, as shown in the metallographic analysis. The microstructure analysis conducted for the WC-12Co Nanox coating indicated that the same nanocrystalline grains of tungsten carbide were present both in the powder and in the coating. This suggests that the HVOF spray process with a relatively low temperature of the stream and a short dwell time did not cause the grains to decompose, despite their small size. The effect of the hot high-velocity gas stream on the WC-12Co Nanox powder was visible in the case of cobalt, which formed many amorphous structures around the nanocrystalline tungsten carbide grains. The microstructure analysis of the coatings produced from the Fe_3O_4 Inflox and Fe_3O_4 Nanox powders showed that, in spite of the differences in the particle size distribution, the morphologies of the two coatings were fairly similar. In both cases, there were clear boundaries between the slightly deformed powder particles and visible pores in the coatings. The TEM analysis of the microstructure of the Fe_3O_4 Nanox coating indicated that there were columnar and axially symmetric extended grains, the size of which ranged from several dozen to several hundred nanometers. In Figures 9.25 and 9.28, showing the microstructures of the conventional and nanostructured coatings, respectively, we can see clear areas of the dark phase, which is the matrix with the spray deposited Fe_3O_4. The element distribution maps obtained for both coatings confirmed that tungsten was absent from areas where iron and oxygen were present. The linear analysis showed that the number of iron counts coincided with that of oxygen counts, which suggested the presence of Fe_3O_4. Moreover, the total number of tungsten counts in those areas dropped nearly to zero. The images of both microstructures were similar, which was due to almost the same size of particles. The distributions of particles, however, differed.

The spray parameters were optimized using the Taguchi method. It was essential to determine what effect the content of Fe_3O_4 in the spray mixture, the oxygen-to-propane ratio, the spray distance and the air pressure had on the properties of the nanostructured composite coating, with the properties including the coefficient of friction, microhardness, wear, roughness and adhesion as well as the wear of the counter surface. The experimental data were used to correct the spray parameters for the nanostructured composite coating. The properties of the nanostructured coating were then compared with those of the conventional coating. The coefficient of friction reported for the nanostructured coating ($\mu = 0.15$) was three times lower than that obtained for the conventional coating ($\mu = 0.48$). The wear of the specimens was 0.0011 g and 0.0018 g for the nanostructured and the conventional coatings, respectively; the wear of the counter surfaces, on the other hand, was 0.0009 g and 0.0014 g, respectively.

The microhardness of the nanostructured coating was 863 HV, which was less than in the case of the conventional coating (892 HV). The adhesion of the nanostructured coating to the PA6 alloy was lower; it was 34.26 MPa, while that of the conventional coating was 39.45 MPa. The tribological tests conducted with a Falex T-09 tester proved that the seizure resistance was

higher for the nanostructured coating (1845N) than for the conventional coating (1793 N). Residual stresses in the nanostructured and the conventional coatings were measured using an original “$g - \sin2\psi$” method developed at the AGH University of Science and Technology. The macroscopic residual stresses were 166 MPa and +145 MPa for the nanostructured composite coatings, and +80 MPa and +260 MPa for the conventional composite coatings, when deposited on aluminum and steel substrates, respectively. The results suggest that the level of residual stresses was lower in the nanostructured coatings than in the conventional coatings. The HVOF spray composite coatings had lower coefficients of friction than WC-12Co coatings without Fe_3O_4. The roughness of the nanostructured coatings was four times higher than that of the coatings produced from the WC-12Co Nanox powder; the addition of Fe_3O_4 Nanox powder had a significant impact on the surface topography. Similar results were obtained for the conventional materials; the difference, however, was smaller. The wear of the nanostructured coatings was reported to be lower than that of the conventional coatings. The nanostructure plays a vital role in the wear processes; it makes the nanostructured coatings more resistant to wear. The adhesion of the nanostructured coatings to the PA6 alloy was lower than that of the conventional coatings, but its degree was sufficiently high to ensure the desired behaviour. Both types of coatings had resistance to seizure at approximately the same level; large standard deviations indicated how complex the seizure process was.

The test results showed that, despite their higher microhardness, HVOF spray nanostructured composite coatings had better properties than chrome plated coatings. **It can be concluded that HVOF spray composite coatings may be an alternative to chrome plated coatings, the production process of which is carcinogenic and should therefore be eliminated.**

Chapter 15

Conclusions

The following conclusions have been drawn on the basis of conducted analyses and experiments:

1. The process of supersonic spraying enables constituting coatings containing a solid lubricant.
2. Having compared the properties of coatings sprayed with conventional and nanostructured powders, it can be inferred that nanocrystal structures have been retained in the coating, which, with reference to a coating of conventional structure, allow to achieve more favourable tribological properties.
3. Taking the presented model of friction into consideration, the application of nanostructured powders is a favourable set of applying a solid lubricant for the coating material. It guarantee the smallest disadvantageous changes of coatings properties and at the same time the greatest uniform distribution of solid lubricant onto mating surfaces of elements.
4. A solid lubricant in the form of Fe_3O_4 has a high level of adhesion to the surface of grains of tungsten carbide present in the cobalt groundmass. According to the absorption theory, this is a fundamental factor required for the interaction of the sliding surfaces.
5. Very thin layers of Fe_3O_4 constituting during the friction process are correspondent to the theory of solid lubricants assuming the existence of facilitated slide surfaces in the crystal structure of a substance being a solid lubricant.
6. Given the diverse and unlimited possibilities of constituting composite coatings with the methods of thermal spraying, a research should be conducted in order to work out composite coatings containing a solid lubricant destined for friction units where they interact with elements containing sprayed coatings.
7. The field of the conducted research should regard particularly friction units interacting in the biological environment with the purpose of implants and also interacting at high and low temperatures as well as in vacuum.
8. The research conducted in the monograph justify further research on composite coatings containing a solid lubricant using nanostructured materials. Reports on this subject are scarce and nanomaterials are a potentially huge challenge due to uncovered possibilities in this aspect.

9. Thermally-sprayed nanostructured coatings, unlike conventional coatings characterized by a microtopography, possess a fully-formed nanotopography on the surface of machine elements. One can assume a hypothesis that such surfaces of machine elements have diverse properties (including tribological ones), which requires conducting further research on nanotribology.
10. Thermally-sprayed composite coating can be constituted even from a few materials forming a groundmass and a solid lubricant. Researching the synergism of components constituting such a coating could enable obtaining a coating with higher tribological properties.
11. Further research concerning corrosion resistance and costs of supersonic sprayed nanocomposite coatings should be included in subsequent studies.

References

1. Ait-Messaoudene N., Abdellah El-Hadj A.: Effect of the substrate and of thermophoresis on the acceleration and heating of particles during HVOF spraying. Surface and Coatings Technology 106 (1998), pp. 140–144.
2. Alidokht S.A., Abdollah-zadeh A., Soleymani S., Assadi H.: Microstructure and tribological performance of an aluminium alloy based hybrid composite produced by friction stir processing. Materials and Design 32 (2011), pp. 2727–2733.
3. Ang S.M., Berndt C.C., Cheang P., Wang J.: Effects of WC particle size on deposition of cold spray WC-Co coatings. Proc. of International Thermal Spray Conference, Singapore 2010, pp. 783–788.
4. Ashby M.F., Ferreira P.J., Schodek DL.: Nanomaterials, nanotechnologies and design. Elsevier Ltd. 2009.
5. Ban Z.-G., Shaw L.L.: Characterization of thermal sprayed nanostructured WC-Co coatings derived from nanocrystalline WC-18wt.%Co powders. Journal of Thermal Spray Technology Volume: 12, Issue: 1, March 2003, pp. 112–119.
6. Barbezat G.: Application of thermal spraying in the automobile industry. Surface and Coatings Technology 201 (2006), pp. 2028–2031.
7. Barbezat G.: Importance of surface preparation technology prior to coating deposition on cylinder bores for high performance engines. Proc. of International Thermal Spray Conference, Beijing 2007, pp. 276–280.
8. Bartuli C., Valente T., Cipri F., Bemporad E., Tului M.: Parametric study of an HVOF process for the deposition of nanostructured WC-Co coatings. Journal of Thermal Spray Technology, Volume: 14, Issue: 2, June 2005, pp. 187–195.
9. Bendell A., Disney J., Pridmore W.: Taguchi Methods; Applications in Word Industry. Springer –Verlag, New York 1989.
10. Bobzin K., Lugscheider E., Zwick J., Ernst F., Sporer D., Hopkins N., Hertter M., Matejicek J.: Microstructure and properties of new abradable seal coatings for compressor applications. Proc. of International Thermal Spray Conference, Seattle 2006.
11. Bobzin K., Lugsheider E., Ernst F., Hidalgo G., Zwick J.: Properties of HVOF sprayed ferrous coatings for corrosion protection. Proc. of International Thermal Spray Conference, Pekin 2007, pp. 555–569.
12. Bobzin K., Bagcivan N., Goebbels N., Yilmaz K., Hoehn B.-R., Michaelis K., Hochmann M: Lubricated PVD CrAlN and WC/C coatings for automotive applications. Surface & Coatings Technology Volume: 204, Issue: 6-7, December 25, 2009, pp. 1097–1101.
13. Bobzin K., Bagcivan N., Theiss S., Yilmaz K.: Plasma coatings CrAlN and a-C:H for high efficient power train in automobile. Surface & Coatings Technology Volume: 205, Issue: 5, November 25, 2010, pp. 1502–1507.
14. Bolelli G., Cannillo V., Gadow R., Killinger A., Lusvarghi L., Rauch J., Romagnoli M.: Effect of the suspension composition on the microstructural properties of high

velocity suspension flame sprayed (HVSFS) Al_2O_3 coatings. Surface & Coatings Technology Volume: 204, Issue: 8, January 15, 2010, pp. 1163–1179.

15. Borisov Y.S., Harłamow A., Sidoenko S.Ł., Adatowska E.N.: Gazotemiczeskije pokrytija iż poroszkowych mateiałow, Kijów, Naukowaja Dumka 1987.
16. Braithwaite E.R.: Solid lubricants and surfaces. Pergamon Press, Oxford 1964.
17. Branagan D.J., Marshall M.C., Meacham B.E., Aprigliano L.F., Bayles R., Lemieux E.J., Newbauer T., Martin F.J., Farmer J.C., Haslam J.J., Day S.D.: Wear and corrosion resistant amorphous/nanostructured steel coatings for replacement of electrolytic hard chromium. Proc. of International Thermal Spray Conference, Seattle 2006.
18. Burakowski T., Żórawski W.: Mikrostruktura i właściwości mechaniczne nanostrukturalnych powłok WC-12Co natryskanych naddźwiękowo. Inżynieria Materiałowa 4/2010, pp. 905–908.
19. Cao Shun-Hua, Zhi-Yong Cai, Jian-Hua Zhou, Jiong-Yi Li and Xin-Ping Lin: Phase transformation of nano-grained W(Co, C) composite powder and its phase constitute. Journal of Central South University of Technology, 2006, Volume 13, Number 6, pp. 603–607.
20. Chen Huang, Lee Soowohn, Zheng Xuebing, Ding Chuanxian: Evaluation of unlubricated wear properties of plasma-sprayed nanostructured and conventional zirconia coatings by SRV tester. Wear Volume: 260, Issue: 9-10, May 31, 2006, pp. 1053–1060.
21. Chen Hui, Gou Guoqing, Tu Mingjing, Liu Yan: Characteristics of nano particles and their effect on the formation of nanostructures in air plasma spraying WC-17Co coating. Surface & Coatings Technology Volume: 203, Issue: 13, March 25, 2009, pp. 1785–1789.
22. Chen Jianmin, Hou Guoliang, Chen Jie, An Yulong, Zhou Huidi, Zhao Xiaoqin, Yang Jie: Composition versus friction and wear behavior of plasma sprayed WC-$(W,Cr)_2$ C-Ni/Ag/BaF_2-CaF_2 self-lubricating composite coatings for use up to 600°C. Applied Surface Science Volume: 261, Complete, November 15, 2012, pp. 584–592.
23. Cherigui M., Fenineche N.E., Coddet C., Gang J., Grosdidier T.: Magnetic properties of HVOF thermally sprayed coatings obtained from nanostructured powders. International Thermal Spray Conference, Basel 2005, pp. 558–562.
24. Chivavibul Pornthep, Watanabe Makoto, Kuroda Seiji, Shinoda Kentaro: Effects of carbide size and Co content on the microstructure and mechanical properties of HVOF-sprayed WC–Co coatings. Surface & Coatings Technology Volume: 202, Issue: 3, December 5, 2007, pp. 509–521.
25. Cho J.H., Xiong Y.M., Kumar S., Ji Y.G., Lee C., Hwang S.Y.: Comparison of the Microstructures and Tribological Behavior of Blended and Nanostructured Composite Coatings by APS. Proc. of International Thermal Spray Conference, Pekin 2007, pp. 764–769.
26. Cho Jinhwan, Xiong Yuming, Kim Juneseob, Lee Changhee, Hwang SoonYoung: Tribological behavior of NiCr-base blended and nanostructured composite APS coatings by rig test. Wear Volume: 265, Issue: 11-12, November 26, 2008, pp. 1565–1571.

27. Cho Tong Yul, Yoon Jae Hong, Cho Jae Young, Joo Yun Kon, Kang Jin Ho, Zhang Shihong, Chun Hui Gon, et. al.: Surface properties and tensile bond strength of HVOF thermal spray coatings of WC-Co powder onto the surface of 420J2 steel and the bond coats of Ni, NiCr, and Ni/NiCr. Surface & Coatings Technology Volume: 203, Issue: 20-21, July 15, 2009, pp. 3250–3253.
28. Czyżniewski A., Gulbiński W., Radnóczi G., Szerencsi M., Pancielejko M.: Microstructure and mechanical properties of WC: H coatings deposited by pulsed reactive magnetron sputtering. Surface and Coatings Technology 2011, 205 (19), pp. 4471–4479.
29. Dahorte N.B., Nayak S.: Nanocoatings for engine application. Surface and Coatings Technology 194 (2005), pp. 58–67.
30. Darut G., Ageorges H., Denoirjean A., Fauchais P.: Tribological performances of YSZ composite coatings manufactured by suspension plasma spraying. Surface & Coatings Technology. doi: 10.1016/j.surfcoat.2012.12.008.
31. Darut G., Ben-Ettouil F., Denoirjean A., Montavon G., Ageorges H., Fauchais P.: Dry Sliding Behavior of Sub-Micrometer-Sized Suspension Plasma Sprayed Ceramic Oxide Coatings. Proc. of International Thermal Spray Conference, Las Vegas 2009, pp. 213–218.
32. Dellacorte C., Edmonds B.J., NASA PS400: a new high temperature solid lubricant coating for high temperature wear applications, NASA TM-2009-215678, August, 2009.
33. DellaCorte C., Bruckner R.J.: Remaining Technical Challenges and Future Plans for Oil-Free Turbomachinery. NASA/TM-2010-216762, June, 2010.
34. Dobrzański L.A.: Metalowe materiały inżynierskie, Wydawnictwo Naukowo-Techniczne, Warszawa 2004.
35. Donnet C., Erdemir A.: Historical developments and new trends in tribological and solid lubricant coatings. Surface and Coatings Technology Volume: 180-181, Complete, March 1, 2004, pp. 76–84.
36. Du H. C. Sun, Hua W.G., Zhang Y.S., Han Z., et al.: Fabrication and evaluation of D-gun sprayed WC–Co coating with self-lubricating property. WC–Co coating with self-lubricating property was deposited by detonation gun. Tribology Letters, 2006, Volume 23, Number 3, pp. 261–266.
37. Du Lingzhong, Chuanbing Huang, Weigang Zhang, Tiegang Li, Wei Liu: Preparation and wear performance of NiCr/Cr_3C_2–NiCr/hBN plasma sprayed composite coating. Surface & Coatings Technology 205 (2011), pp. 3722–3728.
38. El-Hadj A.A., Zirari M., Bacha N.: Numerical analysis of the effect of the gas temperature on splat formation during thermal spray process. Applied Surface Science 257 (2010), pp. 1643–1648.
39. Eriksson J., Olsson M.: Tribological testing of commercial CrN, (Ti,Al)N and CrC/C PVD coatings – Evaluation of galling and wear characteristics against different high strength steels. Surface & Coatings Technology 205 (2011), pp. 4045–4051.
40. Erne M., Kolar D., Hubsch C., Mohwald M., Bach Fr.-W.: Synthesis of Tribologically Favorable Coatings for Hot Extrusion Tools by Suspension Plasma Spraying. Journal of Thermal Spray Technology Volume 21(3-4) June 2012, pp. 668–675.

41. Ernst P., Barbezat G.: Thermal spray application in powertrain contribute in saving of energy and material resources. Surface and Coatings Technology 202 (2008), pp. 4428–4431.
42. Fang W., Cho T.Y., Yoon J.H., Song K.O., Hur S.K., Youn S.J., Chun H.G.: Processing optimization, surface properties and wear behavior of HVOF spraying WC–CrC–Ni coating. Journal of Materials Processing Tech. Volume: 209, Issue: 7, April 1, 2009, pp. 3561–3567.
43. Fanning Christopher E., Blanchet Thierry A.: High-temperature evaluation of solid lubricant coatings in a foil thrust bearing. Wear Volume: 265, Issue: 7-8, September 20, 2008, pp. 1076–1086.
44. Fauchais P., Montavon G., Bertrand G.: From Powders to Thermally Sprayed Coatings. Journal of Thermal Spray Technology Volume: 19, Issue: 1-2, January 2010, pp. 56–80.
45. Flitney B.: Alternatives to chrome for hydraulic actuators. Sealing Technology 10/2007, pp. 8–12.
46. Ford M., Fisher M.: Method for coating combustion engine cylinders by Plasma Transfered Wire Arc Thermal Spray. MSE 121 Spring 2010.
47. Gaona M., Lima R.S., Marple B.R.: Nanostructured titania/hydroxyapatite composite coatings deposited by high velocity oxy-fuel (HVOF) spraying. Materials Science & Engineering A, Volume: 458, Issue: 1-2, June 15, 2007, pp. 141–149.
48. Gaona M., Lima R.S., Marple B.R.: Influence of particle temperature and velocity on the microstructure and mechanical behaviour of high velocity oxy-fuel (HVOF)-sprayed nanostructured titania coatings. Journal of Materials Processing Tech. Volume: 198, Issue: 1-3, March 3, 2008, pp. 426–435.
49. Gardos M.N.: The problem-solving role of basic science in solid lubrication. The First World Tribology Congress, London 1997.
50. Grosdidier Thierry, Ji Gang, Bozzolo N.: Hardness, thermal stability and yttrium distribution in nanostructured deposits obtained by thermal spraying from milled – Y_2O_3 reinforced – or atomized FeAl powders. Intermetallics, Volume: 14, Issue: 7, July, 2006, pp. 715–721.
51. Hamrol A.: Zarządzanie jakością z przykładami. PWN, Warszawa 2007.
52. Handbook of Thermal Spray Technology; J.R. Davis, Davis & Associates, ASM International 2004.
53. Hebda M.: Procesy tarcia, smarowania i zużywania maszyn. ITeE-PIB, Warszawa-Radom 2007.
54. Heimann R.B.: Plasma Spray Coating. WILEY-VCH Verlag GmbH & Co. KGaA, Weinheim 2008.
55. Heshmat H., Hryniewicz P., Walton J.F. II, Willis J.P., Jahanmir S., Dellacorte C.: Low-friction wear-resistant coatings for high temperature foil bearings, Trib. Int. 38 (2005), pp. 1059–1075.
56. Hou Guo-Liang, Zhou Hui-Di, An Yu-Long, Liu Guang, Chen Jian-Min, Chen Jie: Microstructure and high-temperature friction and wear behavior of WC-(W,Cr)2C-Ni coating prepared by high velocity oxy-fuel spraying. Surface & Coatings Technology Volume: 206, Issue: 1, October 15, 2011, pp. 82–94.

57. Hsiao W.T., Su C.Y., Huang T.S., Liao W.H., Leu M.S.: Addition of hBN to NiAl coatings deposited using APS and HVOF thermal spraying, Proc. of International Thermal Spray Conference, Singapore 2010, pp. 885–890.
58. Hu Tianchang, Hu Litian, Ding Qi: Effective solution for the tribological problems of Ti-6Al-4V: Combination of laser surface texturing and solid lubricant film. Surface & Coatings Technology 206 (2012), pp. 5060–5066.
59. Huang Chuanbing, Du Lingzhong, Zhang Weigang: Preparation and characterization of atmospheric plasma-sprayed NiCr/Cr_3C_2–$BaF_2 \cdot CaF_2$ composite coating. Surface & Coatings Technology Volume: 203, Issue: 20-21, July 15, 2009, pp. 3058–3065.
60. Hwang Jong-Hyun, Myoung-Seoup Han, Dae-Young Kim and Joong-Geun Youn: Tribological behavior of plasma spray coatings for marine diesel engine piston ring and cylinder liner. Journal of Materials Engineering and Performance, 2006, Volume 15, Number 3, pp. 328–335.
61. Ibrahim A., Lima R.S., Berndt C.C., Marple B.R.: Fatigue and mechanical properties of nanostructured and conventional titania (TiO2) thermal spray coatings. Surface & Coatings Technology Volume: 201, Issue: 16-17, May 21, 2007, pp. 7589–7596.
62. Johnston R.E.: Mechanical characterisation of AlSi-hBN, NiCrAl-Bentonite, and NiCrAl-Bentonite-hBN freestanding abradable coatings. Surface & Coatings Technology 205 (2011), pp. 3268–3273.
63. Jurczyk M., Jakubowicz J.: Nanomateriały ceramiczne. Wydawnictwo Politechniki Poznańskiej, Poznań 2004.
64. Jurczyk M.: Mechaniczna synteza. Wydawnictwo Politechniki Poznańskiej, Poznań 2003.
65. Jurczyk M.: Nanomateriały. Wybrane zagadnienia. Wydawnictwo Politechniki Poznańskiej, Poznań 2001.
66. Kaźmierczak A., Michnowska E.: Wdrożenie technologii wytwarzania powłok z tlenkami żelaza na powierzchni roboczej pierścieni tłokowych. Inżynieria Powierzchni 4/2006, pp. 42–51.
67. Kelsall R.W., Hamley I.W, Geoghegan M.: Nanotechnologie. Wydawnictwo Naukowe PWN, Warszawa 2008.
68. Keskinen H., Mäkelä J.M.; Aromaa M., Ristimäki J., Kanerva T., Levänen E. et. al.: Effect of silver addition on the formation and deposition of titania nanoparticles produced by liquid flame spray. Journal of Nanoparticle Research Volume: 9, Issue: 4, August 2007, pp. 569–588.
69. Kim G.E., Brochu M., Moran A., Aldona T.: Enhanced TBC Performance with Nanostructured Bond Coats. Proc. of International Thermal Spray Conference, Las Vegas 2009, pp. 397–402.
70. Kim S.H., Hannula S.-P., Lee S.W.: Effects of the sliding conditions on the tribological behavior of atmospheric plasma sprayed Al_2O_3–15 wt.% ZrO_2–CaF_2 composite coating. Surface & Coatings Technology 210 (2012), pp. 127–134.
71. Kim Gilyoung, Choi Hanshin, Han Changmin, Uhm Sangho, Lee Changhee: Characterization of atmospheric plasma spray NiCr–Cr2O3–Ag–CaF2/BaF2 coatings. Surface and Coatings Technology Volume: 195, Issue: 1, May 23, 2005, pp. 107–115.

72. Kim Hyung-Jun, Lee Chang-Hee, Hwang Soon-Young: Superhard nano WC–12%Co coating by cold spray deposition. Materials Science and Engineering: A Volume: 391, Issue: 1-2, January 25, 2005, pp. 243–248.
73. Kitamura J., Sato K., Watanabe M., Chivavibul P., Komatsu M., Sakaki K., Kuroda S.: Mechanical properties of WC-Co coatings prepared by Cold and Warm Spray processes. Proc. of International Thermal Spray Conference, Hamburg 2011, pp. 161–166.
74. Korzyński M.: Metodyka eksperymentu. WNT, Warszawa 2006.
75. Krawiec S.: Kompozycje smarów plastycznych i stałych w procesie tarcia stalowych węzłów maszyn. Oficyna Wydawnicza Politechniki Wrocławskiej, Wrocław 2011.
76. Lawrowski Z.: Technika smarowania, WN PWN, Warszawa 1996.
77. Lawrowski Z.: Tribologia. WN PWN, Warszawa 1993.
78. Lee Jaekeun, Cho Sangwon, Hwang Yujin, Cho Han-Jong, Lee Changgun, Choi Youngmin, Ku Bon-Chul, Lee Hyeongkookee, Lee Byeongchul, Kim Donghan, Kim Soo H.: Application of fullerene-added nano-oil for lubrication enhancement in friction surfaces. Tribology International 42(2009), pp. 440–447.
79. Legg K.O., Graham M., Chang P., Rastegar F., Gonzales A., Sartwell B.: The replacement of electroplating, Surface and Coatings Technology 90(2000).
80. Li Chang-Jiu, Li Jing-Long: Evaporated-gas-induced splashing model for splat formation during plasma spraying. Surface and Coatings Technology 184 (2004), pp. 13–23.
81. Li Q., Li S., Yang W.: Friction and wear properties of plasma sprayed nanostructured chromium oxide coatings. Proc. of International Thermal Spray Conference Maastricht 2008, pp. 443–446.
82. Li Chang-Jiu, Yang Guan-Jun, Gao Pei-Hu, Ma Jian, Wang Yu-Yue, Li Cheng-Xin: Characterization of Nanostructured WC-Co Deposited by Cold Spraying. Journal of Thermal Spray Technology Volume: 16, Issue: 5-6, December 2007, pp. 1011–1020.
83. Li H., Khor K.A.: Characteristics of the nanostructures in thermal sprayed hydroxyapatite coatings and their influence on coating properties Surface & Coatings Technology Volume: 201, Issue: 6, December 4, 2006, pp. 2147–2154.
84. Lima R.S., Karhikeyan J., Kay C.M., Lindemann J., Berndt C.C.: Microstructural characteristics of cold sprayed nanostructured WC-Co coatings. Thin Solid Films 416(2002), pp. 129–135.
85. Lima R.S., Marple B.R., Dadouche A., Dmochowski W., Liko B.: Nanostructured abradable coatings for high temperature applications. Proc. of International Thermal Spray Conference, Seattle 2006.
86. Lima R.S., Marple B.R., Li H., Khor K.A.: Biocompability nanostructured High velocity Oxy-Fuel (HVOF) sprayed titania coatings. Proc. of International Thermal Spray Conference, Seattle 2006.
87. Lima R.S., Marple B.R.: Superior performance of high-velocity oxyfuel-sprayed nanostructured TiO_2 in comparison to air plasma-sprayed conventional Al_2O_3-13TiO_2, JTST 14(3) 2005, pp. 397–404.

88. Lima R.S., Marple B.R.: Thermal Spray Coatings Engineered from Nanostructured Ceramic Agglomerated Powders for Structural, Thermal Barrier and Biomedical Applications: A Review. Journal of Thermal Spray Technology, 2007(1), pp. 40–63.
89. Lima R.S., Marple B.R.: Process–property–performance relationships for titanium dioxide coatings engineered from nanostructured and conventional powders. Materials & Design, vol. 29 (2008), pp. 1845–1855.
90. Lin F., Yu Y., Zeng K., Ren X., Song X., Li Z., Cui Y.: Microstructure and properties of plasma sprayed ultrafine Cr_2O_3 feedstock powder and coating. Proc. of International Thermal Spray Conference, Seattle 2006.
91. Liu J., Yang Z., Wang L., Yan S., Zhang J., Lin F.: Preparation and characterization of nickel clad h-BN composite powders for abradable sealing coating. Proc. of International Thermal Spray Conference Maastricht 2008, pp. 1132–1134.
92. Liu Ru-Tie, Xiong Xiang, Chen Fu-Sheng, Lu Jin-Zhong, Hong Li-Ling, Zhang Yi-Qing: Tribological performance of graphite containing tin lead bronze–steel bimetal under reciprocal sliding test. Tribology International 44 (2011), pp. 101–105.
93. Liu X.Y., Zhao X.B., Ding C.X.: Introduction of bioactivity to plasma sprayed TiO_2 coating with nanostructured surface by post treatment. Proc. of International Thermal Spray Conference, Seattle 2006.
94. Liu Xiufang, Wang Liping, Xue Qunji: A novel carbon-based solid–liquid duplex lubricating coating with super-high tribological performance for space applications. Surface & Coatings Technology 205 (2011), pp. 2738–2746.
95. Longo F.N.: Plasma-sprayed coatings: an alternative to hard chromium, Plating and Surface Finishing, July 1985.
96. Lukaszkowicz K., Pancielejko M.: Struktura i własności tribologiczne nanokrystalicznych powłok naniesionych na podłoże ze stali X40CrMoV5-1. Inżynieria Materiałowa 2011, 32 (4), pp. 537–540.
97. Marple B.R., Lima R.S.: Processing strategies for tailoring ceramic-based nanostructured thermal spray coatings. Proc. of International Thermal Spray Conference, Seattle 2006.
98. Marple B.R., Voyer J., Bisson J.-F., Moreau C.: Thermal spraying of nanostructured cermet coatings. Journal of Materials Processing Technology Volume: 117, Issue: 3, November 23, 2001, pp. 418–423.
99. Mazurkiewicz A., Smolik J.: Badawcze i aplikacyjne uwarunkowania rozwoju hybrydowych technologii inżynierii powierzchni, Mechanik 12 (2011).
100. Michalak M., Michalczewski R., Piekoszewski W., Szczerek M.: Wpływ powłok niskotarciowych na zacieranie smarowanego styku skoncentrowanego. Inżynieria Materiałowa 5 (189)/2012, pp. 489–492.
101. Michalczewski R.: Właściwości tribologiczne smarowanych, wysokoobciążonych elementów maszyn pokrytych cienkimi powłokami niskotarciowymi. Wyd. ITeE-PIB. Radom 2012.
102. Mindivan H.: Wear behavior of plasma and HVOF sprayed WC-12Co+6% ETFE coatings on AA2024-T6 aluminum alloy. Surface & Coatings Technology Volume: 204, Issue: 12-13, March 15, 2010, pp. 1870–1874.

103. Moshkovich A., Perfilyev V., Yutujyan K., Rapoport L.: Friction and wear of solid lubricant films deposited by different types of burnishing. Wear Volume: 263, Issue: 7-12, September 10, 2007, pp. 1324–1327.
104. Moshkovith A., Perfiliev V., Gindin D., Parkansky N., Boxman R., Rapoport L.: Surface texturing using pulsed air arc treatment. Wear Volume: 263, Issue: 7-12, September 10, 2007, pp. 1467–1469.
105. Ozdemir I., Grund T., Wielage B., Tsunekawa Y.: Thermal Spraying of FeB Coatings Containing h-BN Solid Lubricant. Proc. of International Thermal Spray Conference, Pekin 2007.
106. Ozdemir I., Tekmen C., Tsunekawa Y., Grund T.: Wear Behavior of Plasma-Sprayed Al-Si/TiB2/h-BN Composite Coatings. Journal of Thermal Spray Technology Volume 19 (1-2), January 2010, pp. 384–391.
107. Ozdemir I., Ueno T., Tsunekawa Y., Okumiya M.: Cast Iron Coatings Containing Graphite Structure by Atmospheric Plasma Spraying. International Thermal Spray Conference, Osaka 2004, pp. 298–303.
108. Pancielejko M., Czyżniewski A., Zavaleyev V., Pander A., Wojtalik K.: Optimization of the deposition parameters of DLC coatings with the MCVA method. Archives of materials Science and Engineering, 54(2) 2012, pp. 60–67.
109. Papyrin A., Kosarev V., Klinkov S., Alkhimov A., Fomin V.: Cold Spray Technology, Elsevier 2007.
110. Parco M., Fagoaga I., Bobzin K., Lugscheider E., Zwick J., Hidalgo G.: Development and characterization of nanostructured iron based coatings by HFPD and HVOF. Proc. of International Thermal Spray Conference, Seattle 2006.
111. Pawlak W., Wendler B., Makówka M., Sielski J., Kozanecki M., Wysokotemperaturowe niskotarciowe powłoki na bazie MoO_3 i Ag osadzane metoda magnetronową. Inżynieria Materiałowa, 4(182) 2011, pp. 553–557.
112. Pawlowski L.: The science and engineering of thermal spray coatings. John Wiley & Sons 2008, Chichester 2008, 2nd ed.
113. Pawlowski L.: Finely grained nanometric and submicrometric coatings by thermal spraying: A review. Surface & Coatings Technology Volume: 202, Issue: 18, June 15, 2008, pp. 4318–4328.
114. Pawlowski L.: Suspension and solution thermal spray coatings. Surface & Coatings Technology, Volume: 203, Issue: 19, June 25, 2009, pp. 2807–2829.
115. Picas J.A., Forn A., Matthäus G.: HVOF coatings as an alternative to hard chrome for piston and valves. Wear 261 (2006), pp. 477–484.
116. Pimentel J.V., Polcar T., Cavaleiro A.: Structural, mechanical and tribological properties of Mo–S–C solid lubricant coating. Surface & Coatings Technology 205 (2011), pp. 3274–3279.
117. Płaza S., Margielewski L., Celichowski G.: Wstęp do tribologii i tribochemia. Wydawnictwo Uniwersytetu Łódzkiego, Łódź 2005.
118. Pytko S., Pytko P., Furmanik K.: Tribologia smarowania granicznego. Tribologia. Teoria i praktyka 5/2011, pp. 189–203.

119. Pytko S., Pytko P., Furmanik K.: What we know about the boundary lubrication. Scientific Basis of Modern Technologies, Jaremche 2011, ISBN 978-966-8776-23-6, pp. 376–378.
120. Pytko S.: Podstawy tribologii i techniki smarowania. Wyd. AGH, Kraków 1989.
121. Qiao Yunfei, Fischer Traugott E., Dent Andrew: The effects of fuel chemistry and feedstock powder structure on the mechanical and tribological properties of HVOF thermal-sprayed WC–Co coatings with very fine structures. Surface and Coatings Technology, Volume: 172, Issue: 1, July 15, 2003, pp. 24–41.
122. Qiu Y., Khonsari M.M.: Experimental investigation of tribological performance of laser textured stainless steel rings. Tribology International 44 (2011), pp. 635–644.
123. Rajkumar K., Aravindan S.: Tribological performance of microwave sintered copper–TiC–graphite hybrid composites. Tribology International 44 (2011), pp. 347–358.
124. Rampon R., Marchand O., Filiatre C., Bertrand G.: Influence of suspension characteristics on coatings microstructure obtained by suspension plasma spraying. Surface & Coatings Technology Volume: 202, Issue: 18, June 15, 2008, pp. 4337–4342.
125. Rapoport L., Nepomnyashchy O., Lapsker I., Verdyan A., Moshkovich A., Feldman Y., Tenne R.: Behavior of fullerene-like WS2 nanoparticles under severe contact conditions. Wear 259 (2005), pp. 703–707.
126. Rapoport L., Moshkovich A., Perfilyev V., Lapsker I., Halperin G., Itovich Y., Etsion I.: Friction and wear of MoS2 films on laser textured steel surfaces. Surface & Coatings Technology Volume: 202, Issue: 14, April 15, 2008, pp. 3332–3340.
127. Rauch J., Manzat A., Killinger A., Gadow R.: HVOF and HVSFS Coatings for Reduction of Wear and Friction in Cylinder Liners. Proc. of International Thermal Spray Conference, Las Vegas 2009, pp. 1100–1105.
128. Rayón E., Bonache V., Salvador M.D., Bannier E., Sánchez E., Denoirjean A., Ageorges H.: Nanoindentation study of the mechanical and damage behaviour of suspension plasma sprayed TiO_2 coatings. Surface & Coatings Technology 206 (2012), pp. 2655–2660.
129. Rempp A., Killinger A., Gadow R.: New Approach to Ceramic/Metal-Polymer multilayered Coatings for High Performance Dry Sliding Applications. Journal of Thermal Spray Technology Volume 21(3-4) June 2012, pp. 659–667.
130. Roberts E.W.: Ultra low friction films of MoS a for space applications. Thin Solid Films. 181 (1989), pp. 461–473.
131. Sahraoui T., Fenineche N-E., Montavon G., Coddet C.: Alternative to chromium: characteristics and wear behaviour of HVOF coatings for gas turbine shafts repair (heavy-duty). Journal of Materials Processing Technology 152 (2004), pp. 43–55.
132. Saravanan P., Selvarajan V., Rao D.S., Joshi S.V., Sundararajan G.: Influence of process variables on the quality of detonation gun sprayed alumina coatings. Surface and Coatings Technology Volume: 123, Issue: 1, January 10, 2000, pp. 44–54.
133. Schlaefer T., Bobzin K., Ernst F., Richardt K., Verpoort C., Schreiber F., Schwenk A., Flores G.: Plasma transferred wire arc spraying of novel wire feedstock onto cylinder bore walls of AlSi engine blocks. Proc. of International Thermal Spray Conference Maastricht 2008, pp. 17–24.

134. Schneider K.E., Belaschenko V., Dratwinski M., Siegman S., Zagorski A.: Thermal Spraying for Power Generation Components. WILEY-VCH Verlag GmbH & Co. KGaA, Weinheim 2006.
135. Schramm L., Verpoort C., Schwenk A., Bobzin K., Bagcivan N., Schläfer T., Theiß S., Yilmaz K.: Friction improvement of new generations of engines by PTWA cylinder bore coating and new piston rings. Proc. of International Thermal Spray Conference, Hamburg 2011, pp. 495–500.
136. Shin J.-H., Lim D.-S., Ahn H.-S.: Effect of annealing and Fe_2O_3 addition on the high temperature tribological behaviour of the plasma sprayed yttria-stabilized zirconia coating. Surface and Coatings Technology 133-134 (2000), pp. 403–410.
137. Shipway P., McCartney D., Sudaprasert T.: Sliding wear behaviour of conventional and nanostructured HVOF sprayed WC-Co coatings. Wear 259 (2005), pp. 820–827.
138. Shtertser A., Muders C., Veselov S., Zlobin S., Ulianitsky V., Jiang X., Bataev V.: Computer controlled detonation spraying of WC/Co coatings containing MoS_2 solid lubricant. Surface & Coatings Technology, Volume: 206, Issue: 23, July 15, 2012, pp. 4763–4770.
139. Skoneczny W.: Kształtowanie właściwości warstw wierzchnich aluminium i jego stopów metoda anodowania twardego. Wydawnictwo Politechniki Łódzkiej, Bielsko-Biała 2001, ISBN-83-87087-48-3.
140. Skopp A., Kelling N., Woydt M., Berger L.-M.: Thermally sprayed titanium suboxide coatings for piston ring/cylinder liners under mixed lubrication and dry-running conditions. Wear Volume: 262, Issue: 9-10, April 10, 2007, pp. 1061–1070.
141. Skrzypek S.J., Żórawski W., Chruściel K., Goły M.: Przegląd dyfrakcyjnych metod rentgenowskich do charakteryzowania wybranych właściwości powłok. Inżynieria Powierzchni – Wybrane Zagadnienia, Monografia, Kielce 2011, pp. 161–171.
142. Skrzypek S., Żórawski W.: Naprężenia własne w nanostrukturalnych powłokach kompozytowych natryskanych naddźwiękowo. Mechanik 8/9, pp. 786–788.
143. Skrzypek S.J., Baczmański A.: Progress in X-ray Diffraction of Residual Macro-stresses Determination Related to Surface Layer Gradients and Anisotropy. Advances in X-Ray Analysis, 44, 2001, pp. 134–145.
144. Skrzypek S.J., Karp J., Chruściel K.: Automatyczny pomiar makronaprężeń własnych. Przegląd Mechaniczny z.20, (1989), pp. 13–15.
145. Skrzypek S.J.: Makronaprężenia własne cienkich warstw – pomiar metodą g-$\sin^2\psi$ w nowej geometrii dyfrakcji przy stałym kącie padania. Inżynieria Powierzchni (2001), Nr 2, pp. 47–55.
146. Skrzypek S.J.: New methodological Approach in Surface Residual Stress Examinations, Inżynieria Materiałowa Nr 4 (1998), pp. 1035–1038.
147. Skrzypek S.J.: Nowe możliwości pomiaru makro-naprężeń własnych w materiałach przy zastosowaniu dyfrakcji promieniowania X w geometrii stałego kąta padania, Rozprawy i Monografie 108, Uczelniane Wyd. Nauk.-Dydaktyczne AGH, Kraków 2002.
148. Sliney H.E.: Wide Temperature Spectrum Self-Lubricating Coatings Prepared by Plasma Spraying, Thin Solid Films, Vol. 64, 1979, pp. 211–217.

149. Smolik J., Mazurkiewicz A., Poteralska B.: Nowoczesna inżynieria powierzchni – stan wiedzy I kierunki rozwoju, Inżynieria Materiałowa 4 (2011), pp. 562–565.
150. Taguchi G., Chowdhury S., Wu. Y.: Taguchi's Quality Engineering Handbook. Willey 2004.
151. Taguchi G., Elsayed E., Hsiang T.: Quality Engineering Systems. McGraw-Hill, Inc., 1989.
152. Taguchi G.: Taguchi on Robust Technology Development. ASME Press, New York 1993.
153. Tekmen Cagri, Ozdemir Ismail, Fritsche Gudrun, Tsunekawa Yoshiki: Structural evolution of mechanically alloyed Al–12Si/TiB2/h-BN composite powder coating by atmospheric plasma spraying. Surface & Coatings Technology Volume: 203, Issue: 14, April 15, 2009, pp. 2046–2051.
154. Terajima T., Takeuchia F., Nakata K., Adachi S., Nakashim K., Igarashi T.: Composite coating containing WC/12Co cermet and Fe-based metallic glass deposited by high-velocity oxygen fuel spraying. Journal of Alloys and Compounds 504S (2010), pp. S288–S291.
155. Tian W., Wang Y., Yang Y.: Fretting wear behavior of conventional and nanostructured Al_2O_3–13wt%TiO_2 coatings fabricated by plasma spray. Wear Volume: 265, Issue: 11-12, November 26, 2008, pp. 1700–1707.
156. Tillmann W., Vogli E., Hoffmann F.: Wear-resistant and low-friction diamond-like-carbon (DLC)-layers for industrial tribological applications under humid conditions, Surface and Coating Technology 204 (2009), pp. 1040–1045.
157. Toma F.L., Berger L.-M., Scheitz S., Langner S., Rodel C., Potthoff A., Sauchuk V., Kusnezoff M.: Comparison of the Microstructural Characteristics and Electrical Properties of Thermally Sprayed Al_2O_3 Coatings from Aqueous Suspensions and Feedstock Powders. Journal of Thermal Spray Technology 480, Volume 21(3-4) 2012.
158. Trpčevska J., Żórawski W., Jakubeczynova D., Briancin J., Zdravecka E.: Invesigation of microstructure of plasma and HVOF sprayed carbides coatings. Powder Metalurgy Progress, vol. 1, no 1, 2007, pp. 52–58.
159. Tsunekawa Y., Ozdemir I., Okumiya M.: Plasma Sprayed Cast Iron Coatings Containing Solid Lubricant Graphite and h-BN Structure. Journal of Thermal Spray Technology 15 (2006), Issue 1, pp. 239–245.
160. Tului M., Valente T., Becker D., Wagner S.: Plasma sprayed self lubricant coatings. International Thermal Spray Conference, Basel 2005, pp. 1171–1174.
161. Tung Simon C., McMillan Michael L.: Automotive tribology overview of current advances and challenges for the future. Tribology International Volume: 37, Issue: 7, July, 2004, pp. 517–536.
162. Tyagi Rajnesh, Xionga Dangsheng, Li Jianliang: Effect of load and sliding speed on friction and wear behavior of silver/h-BN containing Ni-base P/M composites. Wear 270 (2011), pp. 423–430.
163. Uozato S., Nakata K., Ushio M.: Development of Ferrous Powder Thermal Spray Coatings on Cylinder Bore in Diesel Engine. Proc. of International Thermal Spray Conference, Osaka 2004, pp. 286–289.

164. Valette S., Denoirjean A., Lefort P.: Plasma sprayed steel: Adhesion of an alumina film via a wüstite interlayer. Surface & Coatings Technology 202 (2008), pp. 2603–2611.
165. Varis T., Knuuttila J., Suhonen T., Kanerva U., Silvonen J., Leivo J., Turunen E.: Improving the properties of HVOF- sprayed Cr_2O_3 by nanocomposite powders. Proc. of International Thermal Spray Conference Maastricht 2008, pp. 452–455.
166. Vetter J., Barbezat G., Crummenauer J., Avissar J.: Surface treatment selections for automotive applications. Surface and Coatings Technology 200 (2005) 1990.
167. Wang H.-T., Li C.-J., Yang G.-J., Li C.-X., Zhang Q., Li W.-Y.: Microstructural Characterization of Cold-Sprayed Nanostructured FeAl Intermetallic Compound Coating and its Ball-Milled Feedstock Powders. Proc. of International Thermal Spray Conference, Pekin 2007.
168. Wang Hai-Dou, Xu Bin-Shi, Liu Jia-Jun, Zhuang Da-Ming, Wei Shi-Cheng, Zhang Xian-Cheng, Jin Guo, Jiang Yi: Microstructures and friction-reduction performances of the graphite coatings. Materials Letters 59 (2005), pp. 1683–1686.
169. Wang W.: Application of high temperature self-lubricating composite coating on steam turbine components. Surface & Coatings Technology 177-178 (2004), pp. 12–17.
170. Wang Yongxin, Wang Liping, Xue Qunji: Improvement in the tribological performances of Si_3N_4, SiC and WC by graphite-like carbon films under dry and water-lubricated sliding conditions. Surface & Coatings Technology 205 (2011), pp. 2770–2777.
171. Wang Hai-Dou, Xu Bin-Shi, Liu Jia-Jun, Zhuang Da-Ming: Characterization and tribological properties of plasma sprayed FeS solid lubrication coatings. Materials Characterization Volume: 55, Issue: 1, July, 2005, pp. 43–49.
172. Wang Hai-Dou, Xu Bin-Shi, Liu Jia-Jun, Zhuang Da-Ming, Wei Shi-Cheng, Jin Guo: The iron sulfide coatings prepared by plasma spraying and their friction-reduction performance. Surface & Coatings Technology Volume: 201, Issue: 9-11, February 26, 2007, pp. 5286–5289, 5286–5289.
173. Wang Jun, Li Ke, Shu Da, He Xin, Sun Baode, Guo Qixin, Nishio Mitsuhiro, Ogawa Hiroshi: Effects of structure and processing technique on the properties of thermal spray WC–Co and NiCrAl/WC–Co coatings. Materials Science and Engineering: A Volume: 371, Issue: 1-2, April 25, 2004, pp. 187–192.
174. Wang Y.M., Jiang B.L., Lei T.Q., Guo L.X.: Microarc oxidation and spraying graphite duplex coating formed on titanium alloy for antifriction purpose. Applied Surface Science Volume: 246, Issue: 1-3, June 15, 2005, pp. 214–221.
175. Witaszek S.: Ocena właściwości tribologicznych grupy tłok-tuleja cylindrowa wykonanej z materiałów kompozytowych na osnowie stopów aluminium. Praca doktorska, Politechnika Śląska 2012.
176. Wu J.-H., Phillips B.S., Jiang Wenping, Sanders J.H., Zabinski J.S., Malshe A.P.: Bio-inspired surface engineering and tribology of MoS_2 overcoated cBN–TiN composite coating. Wear Volume: 261, Issue: 5-6, September 20, 2006, pp. 592–599.
177. Wu Yunxin, Wang Fuxing, Cheng Yinqian, Chen Nanping: A study of the optimization mechanism of solid lubricant concentration in Ni/MoS2 self-lubricating composite. Wear 205 (1997), pp. 64–70.

178. Yang K., Fukumoto M., Yasui T., Yamada M.: Role of substrate temperature on microstructure formation in plasma-sprayed splats. Surface & Coatings Technology 214 (2013), pp. 138–143.
179. Yang Hyunseok, Lee Changhee, Hwang Soon Young: The effect of nano-sized Cr_2O_3 addition on the characteristics of $NiCr–Cr_2O_3–Ag–BaF_2/CaF_2$ coating. Surface & Coatings Technology Volume: 201, Issue: 1-2, September 12, 2006, pp. 38–44.
180. Yao Yanli, Wang Xiaomin, Guo Junjie, Yang Xiaowei, Xu Bingshe: Tribological property of onion-like fullerenes as lubricant additive. Materials Letters 62 (2008), pp. 2524–2527.
181. Yuan Jianhui, Zhu Yingchun, Ji Heng, Zheng Xuebing, Ruan Qichao, Niu Yaran, Liu Ziwei, Zeng Yi: Microstructures and tribological properties of plasma sprayed WC–Co–Cu–BaF_2/CaF_2 self-lubricating wear resistant coatings. Applied Surface Science, Volume 256, Issue 16, 2010, pp. 4938–4944.
182. Yuan Jianhui, Zhu Yingchun, Zheng Xuebing, Ji Heng, Yang Tao.: Fabrication and evaluation of atmospheric plasma spraying WC–Co–Cu–MoS_2 composite coatings. Journal of Alloys and Compounds, Volume 509, Issue 5, 3 February 2011, pp. 2576–2581.
183. Yuan Jianhui, Zhu Yingchun, Zheng Xuebing, Ruan Qichao, Ji Heng: Improvement in tribological properties of atmospheric plasma-sprayed WC–Co coating followed by Cu electrochemical impregnation. Applied Surface Science Volume: 255, Issue: 18, June 30, 2009, pp. 7959–7965.
184. Zhang Q., Li C.-J., Li C.-X., Yang G.-J., Wang X.-R., Wang H.-T., Lui S.-C.: Preliminary Study of Oxidation Behavior of Cold Sprayed Nanostructured NiCrAlY Bond Coatings. Proc. of International Thermal Spray Conference, Pekin 2007.
185. Zois D., Lekatou A., Vardavoulias M., Panagiotopoulos I., Vazdirvanidis A.: A Comparative Microstructural Investigation of Nanostructured and Conventional Al_2O_3 Coatings Deposited by Plasma Spraying.Journal of Thermal Spray Technology Volume: 17, Issue: 5-6, December 2008, pp. 887–894.
186. Żórawski W.: Mikrostruktura i własności nanostrukturalnych powłok WC-12Co natryskanych naddźwiękowo. Tribologia. Teoria i Praktyka, 6/2010, pp. 307–317.
187. Żórawski W.: Nanostrukturalne powłoki kompozytowe natryskane naddźwiękowo. XVI Naukowo-Techniczna Krajowa Konferencja Spawalnicza „Postęp, innowacje i wymagania jakościowe procesów spajania”. Międzyzdroje 2010, ISBN 978-83-60637-50-0, pp. 303–314.
188. Żórawski W., Davin F.: Microstructure and properties of HVOLF sprayed nanostructured carbide coatings. Journal of Machine Manufacturing, Vol. XLIX, Issue E3-E5, 2009, pp. 23–27.
189. Żórawski W., Trpčevská J.: Własności nanostrukturalnych powłok węglikowych natryskanych naddźwiękowo. VI Konferencja Naukowo-Techniczna „TEROTECHNOLOGIA 2009”, Kielce 2009, pp. 446–450.
190. Żórawski W., Bokuvka O., Skrzypek S.: Tribological properties of plasma and HVOF sprayed composite coatings. Przegląd Spawalnictwa 8/2012, pp. 28–34.

191. Żórawski W., Burakowski T.: Badanie mikrostruktury powłok kompozytowych 85%WC-12Co +15%Fe_3O_4 konwencjonalnych i nanostrukturalnych. Mechanik 8/9 pp. 789–790.
192. Żórawski W., Chatys R., Radek N., Borowiecka-Jamrozek J.: Plasma sprayed composite coatings with reduced friction coefficient. Surface & Coatings Technology 202 (2008), pp. 4578-4582.
193. Żórawski W., Kozerski S.: Scuffing resistance of plasma and HVOF sprayed WC-12Co, $Cr_3C_2$25(Ni20Cr) coatings. Surface & Coatings Technology 202 (2008), pp. 4453–4457.
194. Żórawski W., Skrzypek S., Trpčevska J.; Tribological properties of hypersonically sprayed carbide coatings. FME Transactions, University of Belgrade, Vol. 36, No. 2, 2008, pp. 81–86.
195. Żórawski W., Skrzypek S.: Tribological properties of plasma and HVOF-sprayed NiCrBSi-Fe_2O_3 composite coatings. Surface & Coatings Technology 220(2013), pp. 276–281.
196. Żórawski W.: Influence of plasma and supersonic spraying parameters on the roughness of composite coatings. VI International Congress on Precision Machining, Sandomierz – Kielce 2007, pp. 185–190.
197. Żórawski W.: Mikrostruktura powłok miedzianych natryskanych zimnym gazem. Inżynieria Powierzchni 1/2006, pp. 29–34.
198. Żórawski W.: Nowe kierunki rozwoju natryskiwania cieplnego w produkcji nowych części maszyn. Inżynieria powierzchni 3/2011, pp. 10–17.
199. Żórawski W.: Odporność na zatarcie galwanicznych powłok chromowych i natryskanych HVOF powłok WC-12Co. Tribologia, teoria i praktyka 4/2008 (220), pp. 235–246.
200. Żórawski W.: Selected tribological properties of nanostructured HVOF sprayed composite coatings. Rozdział w monografii w jęz. ang. “Scientific basis of modern technologies: experience and prospects, Edited by J.I. Shalapko, Institute of Mechanics and Computer Science, Khmelnitsky National University, Ukraine, L.A. Dobrzanski, Institute of Engineering Materials and Biomaterials, Silesian University of Technology, Gliwice, Poland, Jaremche 2011, pp. 211–222.
201. Żórawski W.: The microstructure and tribological properties of liquid-fuel HVOF sprayed nanostructured WC-12Co coatings. Surface & Coatings Technology 220(2013), pp. 282–289.
202. Żórawski W.: Właściwości tribologiczne nanostrukturalnych powłok kompozytowych natryskanych HVOF. Tribologia. Teoria i praktyka, 4/2011, pp. 271–281.
203. Żórawski W.: Własności powłok węglikowych natryskanych HVOLF. Przegląd Spawalnictwa 8/2007, pp. 112–115.
204. Żórawski W.: Tribological properties of supersonic sprayed nanostructured WC-12Co coatings. Rozdział w monografii “Nanomaterials”, Kraków 2010, ISBN 978-83-912887-9-5, pp. 74–83.